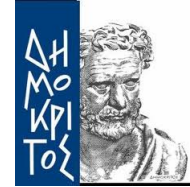Σχολη Εφαρμοσμενων
Μαθηματικων & Φυσικων
Επιστημων

Σχολη Μηχανολογων
Μηχανικων

Ινστιτουτο Πυρηνικης
Φυσικης

Ινστιτουτο Επιστημης
Υλικων

Μελέτη σε δέσμες σωματιδίων ενός ανιχνευτή micromegas $1 \times 1 \text{ m}^2$, για το αδρονικό θερμιδόμετρο του ILC

ΜΕΤΑΠΤΥΧΙΑΚΗ ΔΙΠΛΩΜΑΤΙΚΗ ΕΡΓΑΣΙΑ
Μ.Δ.Ε. Φυσικη και Τεχνολογικές Εφαρμογές

του

Τσιγαρίδα Α. Στέργιου

Επιβλέπων: Τσιπολίτης Γεώργιος
Αναπληρωτής Καθηγητής Ε.Μ.Π

Εγκρίθηκε από την τριμελή εξεταστική επιτροπή την 27/02/2013

....
Θεόδωρος Αλεξόπουλος
Καθηγητής Ε.Μ.Π

....
Γεώργιος Τσιπολίτης
Αν. Καθηγητής Ε.Μ.Π

....
Ευάγγελος Γαζής
Καθηγητής Ε.Μ.Π

ii

....
Στέργιος Α. Τσιγαρίδας
Διπλωματούχος Φυσικός Εφαρμογών, Σ.Ε.Μ.Φ.Ε., Ε.Μ.Π,
Διπλωματούχος Μ.Δ.Ε. «Φυσική & Τεχνολογικές Εφαρμογές», Σ.Ε.Μ.Φ.Ε., Ε.Μ.Π

iv

Acknowledgements

Ολοκληρώνοντας την διπλωματική μου εργασία θα ήθελα να ευχαριστήσω όλους αυτούς τους ανθρώπους που με ενέπνευσαν να ασχοληθώ με τη φυσική και με καθοδήγησαν όλα αυτά τα χρόνια ως μαθητή και μετέπειτα ως προπτυχιακό ή και μεταπτυχιακό φοιτητή.

Αρχικά θα ήθελα να ευχαριστήσω τον καθηγητή μου κύριο Γεώργιο Τσιπολίτη ο οποίος, μέσω της διδασκαλίας του μου μετέδωσε το "μικρόβιο" της Πειραματικής Φυσικής Υψηλών Ενεργειών και στη συνέχεια μου έδωσε την ευκαιρία να ασχοληθώ ενεργά και να αγαπήσω το συγκεκριμένο αντικείμενο. Τον ευχαριστώ επίσης για την ευκαιρία που μου έδωσε να εργαστώ στο CERN, όπου πήρα μια πρώτη γεύση για το πως λειτουργεί ένα σύγχρονο ερευνητικό κέντρο και μέσω της συνεργασίας με άλλους επιστήμονες, αποκόμισα σημαντικές εμπειρίες για την μετέπειτα ζωή και καριέρα μου.

Οφείλω να εκφράσω ένα μεγάλο ευχαριστώ ευχαριστώ στον φίλο, συμφοιτητή και πλέον υποψήφιο διδάκτορα Νικόλαο Καραστάθη για τις συμβουλές του σε θέματα υπολογιστικής φύσεως και όχι μόνο, οι οποίες συνέβαλαν στην ολοκλήρωση της εργασίας. Θα μείνουν βαθιά χαραγμένες στο μυαλό μου, οι μακροχρόνιες και ουσιώδεις συζητήσεις που είχαμε, για πάσης φύσεως θέματα, τόσο κατά την παραμονή μου στη Γενεύη όσο και τον υπόλοιπο καιρό. Τον ευχαριστώ και του εύχομαι τα καλύτερα.

Ευχαριστώ ιδιαίτερα τον υποψήφιο διδάκτορα Κωνσταντίνο Καρακώστα για την την φιλοξενία του τις πρώτες μέρες και τις πολύτιμες συμβουλές του για την χρησιμοποίηση του αλγόριθμου εύρεσης τροχιών που έχει κατασκευάσει, η χρήση του οποίου ήταν καταλυτική για την έκβαση της παρούσας εργασίας. Ευχαριστώ επίσης, τους Στέφανο Λεοντσίνη και Κώστα Ντέκα για την φιλοξενία τους κατά την διάρκεια των πειραμάτων.

Θα ήθελα να ευχαριστήσω επίσης, τους συναδέλφους μου Καστριώτου Μαρία και Σταματόπουλο Αθανάσιο, για τις ευχάριστες συζητήσεις μας στο εργαστήριο πειραματικής φυσικής υψηλών ενεργειών αλλά και γιατί με ανέχτηκαν όλο αυτόν τον καιρό. Ευχαριστώ επίσης όλους τους φίλους μου για την στήριξη τους κατά τη διάρκεια της εκπόνησης της εργασίας

Τέλος, το μεγαλύτερο ευχαριστώ από τα βάθη της καρδιάς μου δε θα μπορούσε να μην ανήκει στην οικογένεια μου. Τους ευχαριστώ για την ηθική και υλική υποστήριξη τους τα χρόνια των σπουδών μου και γενικότερα στη ζωή μου στις εύκολες και δύσκολες στιγμές. Χωρίς αυτούς δε θα είχα τη δυνατότητα να κυνηγήσω τα όνειρα μου και δε θα είχα φτάσει στο σημείο που βρίσκομαι σήμερα.

Abstract in Greek language

Η παρούσα εργασία εκπονήθηκε στα πλαίσια του διατμηματικού προγράμματος μεταπτυχιακών σπουδών "Φυσική & Τεχνολογικές Εφαρμογές" υπό την οργάνωση του τομέα Φυσικής του Εθνικού Μετσόβιου Πολυτεχνείου. Αντικείμενο της εργασίας είναι η ανάλυση δεδομένων από πειράματα που πραγματοποιήθηκαν στο Ευρωπαϊκό Κέντρο Πυρηνικών Ερευνών(CERN) και αφορούν την μελέτη ενός πρωτότυπου ανιχνευτή σωματιδίων, βασισμένο στην τεχνολογία Micromegas. Η συγκεκριμένη τεχνολογία είναι μια από τις υποψήφιες για χρήση στο αδρονικό θερμιδόμετρο ενός μελλοντικού γραμμικού επιταχυντή.

Η ανακοίνωση των τελευταίων αποτελεσμάτων των δύο μεγαλύτερων πειραμάτων του CERN (ATLAS,CMS) και η ανακάλυψη ενός μποζονίου το οποίο θέτει υποψηφιότητα για επιβεβαίωση των προβλέψεων του καθιερωμένου προτύπου για το μποζόνιο Higgs, εντείνει και ενθαρρύνει τις σκέψεις για την κατασκευή ενός γραμμικού επιταχυντή ηλεκτρονίων για την πραγματοποίηση μετρήσεων μεγάλης ακρίβειας που ακολουθεί συνήθως μετά τη λειτουργία ενός επιταχυντή αδρονίων όπως είναι ο LHC στο CERN.

Η κατασκευή ενός τέτοιου τύπου γραμμικού επιταχυντή προϋποθέτει την ύπαρξη θερμιδομέτρων υψηλής ενεργειακής διακριτικής ικανότητας. Την μελέτη και κατασκευή των θερμιδομέτρων έχει αναλάβει η διεθνής συνεργασία CALICE. Στα πλαίσια της συνεργασίας αυτής ένα πρωτότυπο θερμιδόμετρο βασισμένο στην τεχνολογία Micromegas, έχει κατασκευαστεί στο εργαστήριο σωματιδιακής φυσικής του Annecy(LAPP). Τον Αύγουστο του 2011 εκτέθηκε για πρώτη φορά σε δέσμες σωματιδίων(μιόνια,πιόνια) στις εγκαταστάσεις του H4/SPS στο CERN. Για την μελέτη της απόδοσης του συγκεκριμένου ανιχνευτή, χρησιμοποιήθηκε το τηλεσκόπιο του RD51 για την ανίχνευση τροχιών των σωματιδίων και ανιχνευτές σπινθηρισμού ως σύστημα σκανδαλισμού.

Στο πρώτο κεφάλαιο γίνεται μια εκτεταμένη περιγραφή της εργασίας στην ελληνική γλώσσα. Η υπόλοιπη εργασία είναι γραμμένη στην αγγλική γλώσσα και περιλαμβάνει στο δεύτερο κεφάλαιο τις βασικές αρχές που διέπουν την αλληλεπίδραση βαρέων φορτισμένων σωματιδίων με την ύλη. Στο τρίτο κεφάλαιο γίνεται αναφορά στους ανιχνευτές αερίου τύπου Micromegas και στις βασικές τους ιδιότητες. Τέλος το τέταρτο και πέμπτο κεφάλαιο αφορούν την ανάλυση των δεδομένων και την παρουσίαση των αποτελεσμάτων από τα πειράματα για το τηλεσκόπιο και το θερμιδόμετρο αντίστοιχα.

Abstract

This thesis is a part of "Physics & Technological Application" M.Sc. program hosted by department of Physics at National Technological University of Athens. Scope of the thesis is the data analysis of a test-beam that took place at SPS/CERN in order to study a prototype Micromegas detector, which is one of the candidate technologies for the hadronic calorimeter of a future linear collider.

After the presentation of the latest results of CERN's large experiments(ATLAS,CMS) the discovery of a new particle, candidate for the Standard Model Higgs boson, encourages the thoughts about the construction of a linear electron collider, in order to take precise measurements, that usually follows the operation of an hadron collider like CERN's Large Hadron Collider(LHC).

The construction of a linear electron collider requires calorimeters with high granularity and jet energy resolution. The research and development of calorimeters for a future linear collider has undertaken from the international collaboration CALICE. On the behalf of CALICE collaboration a prototype calorimeter based on Micromegas technology developed at Laboratoire d'Annecy-le-Vieux de Physique des Particules - CNRS/IN2P3. The prototype tested at particle beams(muons, pions) for first time at CERN's H4/SPS facilities during August 2011. For the efficiency studies of the prototype, installed a set-up consisted of a micromegas telescope(RD51) for tracking, the prototype and three scintillators plus PMT for triggering.

In the first chapter, presented a detailed description of the thesis in Greek language. The rest of the thesis written in English language and presents the basic principles of heavy charged particle interaction with matter in chapter 2. In chapter 3, presented the Micromegas detector and its properties, while in chapters 4 and 5 presented the results from the data analysis for the telescope and the prototype respectively.

x

Contents

Preface to Greek Language

Η παρούσα εργασία πραγματεύεται την μελέτη συμπεριφοράς και απόδοσης σε δέσμες σωματιδίων, ενός πρωτότυπου ανιχνευτή Micromegas διαστάσεων 1×1 m^2. Η τεχνολογία είναι μια από τις υποψήφιες για χρησιμοποίηση στο αδρονικό θερμιδόμετρο ενός μελλοντικού γραμμικού επιταχυντή $e^- - e^+$. Μετά από ένα εκτεταμένο πρόλογο στην ελληνική γλώσσα όπου θα παρουσιάζεται συνοπτικά το περιεχόμενο της εργασίας θα ακολουθήσει το κυρίως μέρος της στην αγγλική γλώσσα.

1.1 Μελλοντικός γραμμικός επιταχυντής

Κατά τη διάρκεια των προηγούμενων αλλά και των αμέσως επόμενων χρόνων τα πειράματα που διεξάγονται στο Ευρωπαϊκό Κέντρο Πυρηνικών Ερευνών (CERN) θα αποτελέσουν μια πρώτη ματιά στην υψηλότερη κλίμακα ενέργειας που έχει επιτευχθεί μέχρι σήμερα. Αυτό θα γίνει με χρήση του μεγάλου αδρονικού επιταχυντή όπου επιταχύνονται και συγκρούονται δέσμες πρωτονίων-αντιπρωτονίων.

Το γεγονός ότι, τα πρωτόνια δεν είναι στοιχειώδη σωματίδια αλλά έχουν συστατικά, συνεπάγεται ότι ένα μόνο μέρος της αρχικής ενέργειας του πρωτονίου συμμετέχει στις συγκρούσεις, ενώ η ακριβής ενέργεια κάθε σύγκρουσης είναι άγνωστη. Ως αποτέλεσμα, έχουμε συγκρούσεις που καλύπτουν ένα μεγάλο εύρος ενεργειών χωρίς αλλαγή των συνθηκών λειτουργίας και έτσι οι αδρονικοί επιταχυντές χαρακτηρίζονται ως *επιταχυντές ανακαλύψεων*.

Ωστόσο, παρόλο που ένας αδρονικός επιταχυντής είναι ιδανικός για ανακαλύψεις νέας φυσικής, υστερεί στις μετρήσεις ακριβείας. Για να γίνουν μετρήσεις ακριβείας πρέπει να χρησιμοποιηθεί ένας επιταχυντής $e^- - e^+$ ή γενικά ένας επιταχυντής στοιχειωδών σωματιδίων. Τα ηλεκτρόνια επειδή είναι στοιχειώδη, μας επιτρέπουν να γνωρίζουμε την αρχική ενέργεια της σύγκρουσης με ακρίβεια και συνήθως τη λειτουργία ενός επιταχυντή ανακαλύψεων ακολουθεί αυτή ενός επιταχυντή για μετρήσεις ακριβείας.

Για επιταχυντές ηλεκτρονίων, η υψηλότερη ενέργεια έχει επιτευχθεί στον κυκλικό επιταχυντή LEP (στη σημερινή σήραγγα του LHC) και είναι περίπου 200 GeV. Για υψηλότερες ενέργειες, οι απώλειες λόγω ακτινοβολίας synchrotron αυξάνονται δραματικά με αποτέλεσμα να μη εξετάζεται μια παρόμοια λύση για το μέλλον. Ο μόνος τρόπος για να επιτευχθούν τέτοιες ενέργειες είναι να κατασκευαστεί ένας γραμμικός επιταχυντής, όπου τα ηλεκτρόνια θα επιταχύνονται στις υψηλές ενέργειες μόνο με ένα πέρασμα.

Οι δύο βασικές τεχνολογίες που ακόμη βρίσκονται στο στάδιο της έρευνας, είναι ο International Linear Collider (ILC) και ο Compact Linear Collider (CLIC). Βασίζονται σε διαφορετική λειτουργία όσον αφορά την επιταχυντική διάταξη και θα φτάσουν σε διαφορετικές ενέργειες κάτι που οδηγεί σε διαφορετικό περιβάλλον συγκρούσεων.

Ο ILC σχεδιάζεται για να φτάσει σε ενέργειες στο κέντρο μάζας τάξης των $\sqrt{s} = 500\ GeV$ με μια πιθανή αναβάθμιση στα $1\ TeV$, ενώ ο Compact LInear Collider (CLIC) για $\sqrt{s} = 3\ TeV$, το οποίο θα θα προσεγγιστεί σε διάφορα στάδια, ξεκινώντας απο τα $\sqrt{s} = 500\ GeV$. Οι δύο διατάξεις για ενέργειες των $\sqrt{s} = 500\ GeV$ είναι ικανές να αποτυπώσουν τις ίδιες φυσικές συνθήκες. Ωστόσο, αν αποφασιστεί ότι τα ερωτήματα που ταλανίζουν την φυσική στοιχειωδών σωματιδίων τον τελευταίο καιρό, μπορούν να απαντηθούν σε ενέργειες $\sqrt{s} < 1\ TeV$, είναι πολύ πιθανό να κατασκευαστεί ο ILC, γιατί βασίζεται γνωστές και σταθερές συνθήκες επιτάχυνσης. Ο βασικός λόγος που μελετάται ο CLIC είναι για περίπτωση υψηλότερων ενεργειών, όπου θα είναι δυνατή η μελέτη σωματιδίων υψηλότερη ακόμα και απο αυτή που επιτυγχάνεται στον LHC.

1.2   International Linear Collider

Ο International Linear Collider (ILC) είναι ένας επιταχυντής e^+e^- νέας γενιάς. Οι ανιχνευτικές και επιταχυντικές του διατάξεις Θα είναι το μεταίχμιο της επιστήμης και θα επιχειρήσει μια πρωτοπόρα και εις βάθος ματιά στα θεμελιώδα ζητήματα της φύσης, με την τελειοποίηση και επέκταση των δυνατοτήτων του μεγάλου αδρονικού επιταχυντή στο CERN.

Σχεδιάζεται για να λειτουργήσει σε ενέργειες στο κέντρο μάζας που ξεκινούν απο τα $\sqrt{s} = 91$ και φτάνουν μέχρι τα $500\ GeV$, ή μέχρι τα $1\ TeV$ σε δεύτερο στάδιο. Το ενεργειακό εύρος σε συνδυασμό με την ξεκάθαρη εικόνα για την αρχική κατάσταση των συγκρούσεων, κάνει πιθανή την περαιτέρω μελέτη του *Καθιερωμένου Προτύπου* (Standard Model) όπως επίσης και των πιθανών επεκτάσεων του όπως η *Υπερσυμμετρία* (SUSY) ή οι περισσότερες διαστάσεις, σε ένα πρόγραμμα συμπληρωματικό του LHC. Ο LHC, λόγω της υψηλής ενέργειας στο κέντρο μάζας ($14\ TeV$), είναι μια πανίσχυρη μηχανή ανακαλύψεων στη φυσική αυτής της κλίμακας ενεργειών. Εν συνεχεία ο ILC θα χρησιμοποιηθεί για την διεξαγωγή λεπτομερών μετρήσεων, όπως ο προσδιορισμός των ιδιοτήτων ενός πιθανού σωματιδίου Higgs που θα αποκαλυφθεί. Η βασική δομή του ILC φαίνεται στο σχημα [2.3].
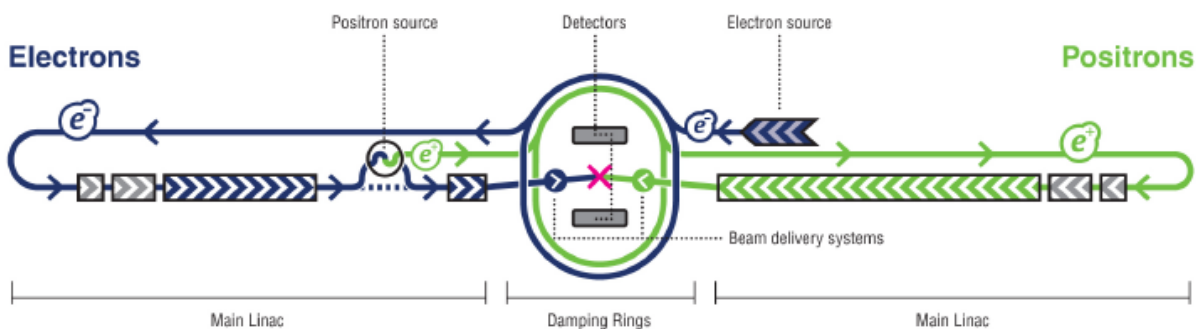

Figure 1.1: Αναπαράσταση της βασικής δομής του ILC.

1.3 Θερμιδομετρία σε έναν μελλοντικό γραμμικό επιταχυντή

Ανάλογα με τα αποτελέσματα του LHC, θα αποφασιστεί ποια απο τις δύο προαναφερθείσες τεχνολογίες θα πάρει την έγκριση για κατασκευή. Σε κάθε περίπτωση όμως, η μέτρηση της ενέργειας (ή αλλιώς θερμιδομετρία) των παραγόμενων σωματιδίων είναι μείζονος σημασίας. Αυτό προϋποθέτει την κατασκευή θερμιδόμετρων για μετρήσεις υψηλής ακρίβειας.

Διάφορες τεχνολογίες ανιχνευτών είναι υπό μελέτη για την χρησιμοποίηση στα θερμιδόμετρα του μελλοντικού γραμμικού επιταχυντή. Για το ρόλο αυτό έχει συσταθεί μια διεθνής συνεργασία με το όνομα CALICE. Οι υπο μελέτη τεχνολογίες βασίζονται σε ανιχνευτές στερεάς κατάστασης κυρίως για το πλεκτρομαγνητικό θερμιδόμετρο, ενώ για το αδρονικό εξετάζονται κυρίως ανιχνευτές αερίου. Η τελική επιλογή ωστόσο, θα γίνει με διάφορα κριτήρια που ποικίλουν ανάλογα με την διάταξη που θα πάρει την έγκριση για κατασκευή, το μέγεθος της, τον τρόπο λήψης δεδομένων και φυσικά το κόστος.
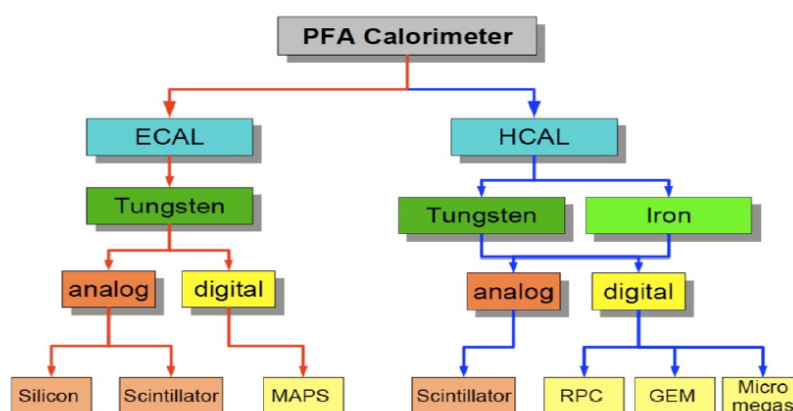
Figure 1.2: Επισκόπηση των διαφόρων τεχνολογιών που είναι υποψήφιες για χρήση σε ένα μελλοντικό γραμμικό επιταχυντή.

1.4 Ανιχνευτής MicroMeGaS

Η Micromegas ανιχνευτής εφευρέθηκε από τους Γ.Γιοματάρη και G. Charpak, το 1995. Ο ανιχνευτής Micromegas είναι ένας ανιχνευτής αερίου που στην ουσία λειτουργεί όπως ένας αναλογικός απαριθμητής και μπορεί να ανιχνεύσει φορτισμένα σωματίδια (πλεκτρόνια, μιόνια, άλφα) και ουδέτερα (φωτόνια, νετρόνια) με κατάλληλη επιλογή αερίου και συνθηκών λειτουργίας. Είναι κατασκευασμένος από υλικά χαμηλού κόστους και λόγω του απλού μηχανικού σχεδιασμού του μπορεί να παραχθεί μαζικά. Χαρακτηρίζεται από καλή ενεργειακή διακριτική ικανότητα και εξαιρετική χωρική και μπορεί να ανιχνεύσει φωτόνια πολύ χαμηλής ενέργειας (250eV) εξαιτίας του μεγάλου πολλαπλασιαστικού παράγοντα (high gain) ενώ η πολύ γρήγορη συλλογή φορτίου επιτρέπει την μέτρηση μεγάλου ρυθμού σωματιδίων. Τα πολύ γρήγορα σήματα αυτά (1ns για πλεκτρόνια, 100ns για θετικά ιόντα) δεν περιορίζουν την ικανότητα ανίχνευσης υψηλού ρυθμού σωματιδίων, σε αντίθεση μετους παραδοσιακούς ανιχνευτές αερίου (χρόνος συλλογής ιόντων 50μs). Λόγω των ιδιοτήτων του ο Micromegas μπορεί να χρησιμοποιηθεί για διάφορα πειράματα φυσικής ενεργειών αλλά και για ιατρικούς σκοπούς. Μερικά ενδεικτικά πειράματα που έχει χρησιμοποιηθεί είναι τα: COMPASS, TESLA, n-TOF, CAST ενώ έχει πάρει έγκριση και για τη χρησιμοποίηση στο πείραμα ATLAS.

Figure 1.3: Σχηματική αναπαράσταση του ανιχνευτή Micromegas

1.4.1 Δομή του ανιχνευτή **Micromegas**

Ένα από τα κύρια χαρακτηριστικά του ανιχνευτή, είναι η ασύμμετρη δομή του. Αποτελείται από δύο περιοχές οι οποίες διαχωρίζονται από ένα πλέγμα το οποίο είναι γνωστό με την ονομασία micromesh. Το πρώτο τμήμα του ανιχνευτή, που θα πρέπει να δια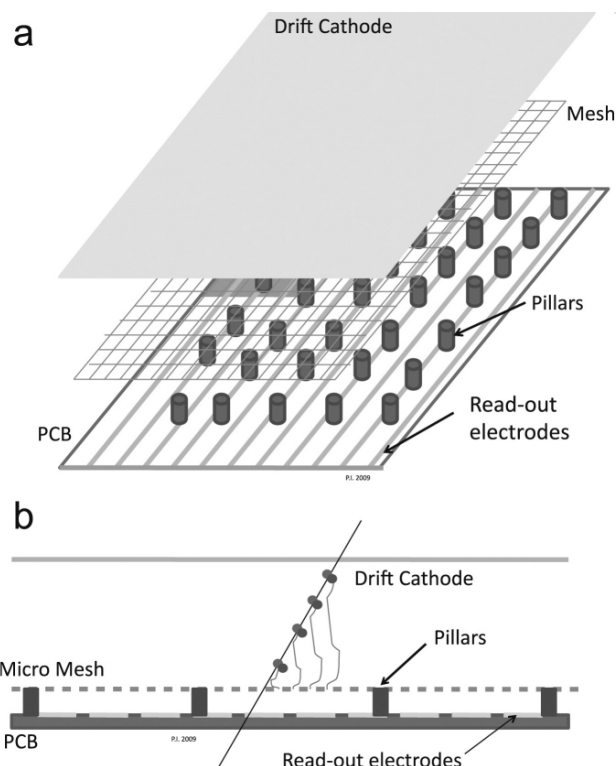σχίσει ένα σωματίδιο είναι η περιοχή μετατροπής(Conversion gap). Η περιοχή εκτείνεται απο το ηλεκτρόδιο ολίσθησης (drift electrode) μέχρι το micromesh. Το δεύτερο τμήμα του ανιχνευτή ονομάζεται περιοχή ενίσχυσης (amplification gap) και εκτείνεται απο το micromesh μέχρι τα ηλεκτρόδια ανάγνωσης(strips), απο όπου λαμβάνεται το σήμα μέσω κατάλληλων ηλεκτρονικών. Οι τυπικές διαστάσεις για την περιοχή ενίσχυσης είναι γύρω στα $3 - 5mm$ ενώ για την περιοχή ενίσχυσης είναι της τάξης των $100\mu m$. Για να διατηρηθεί παράλληλο το πλέγμα με την άνοδο εγκαθιστώνται pillars κάθε $2mm$ με διάμετρο $50 - 150\mu m$.Αυτά τυπώνονται από ένα φιλμ (photoresistive polyamide film) με τη μέθοδο της συμβατικής λιθογραφίας πάνω σε εποξικό υπόστρωμα. Το πάχος του φιλμ καθορίζει και το βάθος της περιοχής ενίσχυσης.

Τα ηλεκτρόδιο ολίσθησης και το micromesh τροφοδοτούνται με διαφορετική τάση στο καθένα, ενώ τα strips είναι γειωμένα. Συνεπώς στα conversion και amplification gap να έχουμε τη δημιουργία ηλεκτρικού πεδίου. Το ηλεκτρικό πεδίο του conversion gap είναι της τάξης του $1 - 3kV/cm$ ενώ αυτό του amplification gap, λόγω των μικρών διαστάσεων του είναι πολύ πιο ισχυρό και κυμαίνεται μεταξύ $30 - 50kv/cm$ ανάλογα με την τάση με την οποία τροφοσοτούμε το mesh. Μια σχηματική ανααράσταση του ηλεκτρικού πεδίου φαίνεται στο παρακάτω σχήμα:

Ο ρόλος του πλέγματος (micromesh) είναι πολλαπλός και είναι κάτι περισσότερο από το να οριοθετεί την περιοχή μετατροπής (conversion gap) και την περιοχή ενίσχυσης (amplification gap). Κατασκευάζεται από ένα λεπτό φύλλο χαλκό πάχους $3 - 5m$ με μία διαδικασία η οποία βασίζεται στην τεχνική της φωτολιθογραφίας και επιτρέπει την χάραξη σε αυτόν ανοιγμάτων 25 μm με βήμα 50 μm. Η τάση που εφαρμόζεται είναι της τάξης των $500 - 600V$ και είναι τόση ώστε
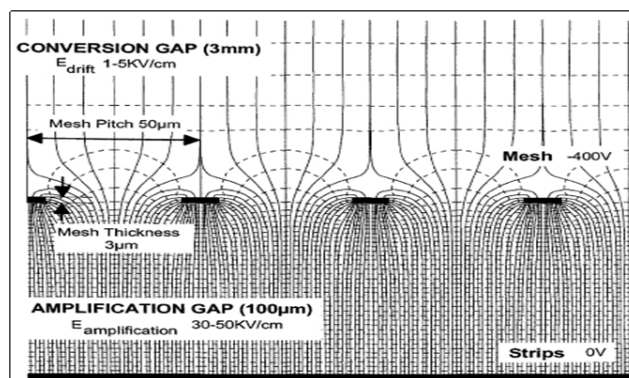
Figure 1.4: Αναπαράσταση των γραμμών του ηλεκτρικού πεδίου ενός ανιχνευτή micromegas

ο λόγος του ηλεκτρικού πεδίου της περιοχής ενίσχυσης προς αυτό της περιοχής μετατροπής, να είναι μεγάλος. Όσο μεγαλύτερος είναι αυτός ο λόγος τόσο πιο μακριά γίνεται η μετάβαση του ηλεκτρονίου στην περιοχή ενίσχυσης. Πρέπει να είναι μεγαλύτερος του 5 για να έχουμε μεταφορά όλων των ηλεκτρονίων από την μία περιοχή την άλλη. Επιπλέον, όταν ο λόγος παίρνει αυτή τη τιμή απορροφώνται από το mesh όλα τα ιόντα που έχουν παραχθεί από τους ιονισμούς και δεν διαφεύγουν στην περιοχή μετατροπής. Την ίδια στιγμή, καθώς παρέχεται ένας ομαλός δρόμος για τα ηλεκτρόνια στην περιοχή ενίσχυσης, το πλέγμα αποτρέπει τα ιόντα που παράγονται από τη χιονοστιβάδα να εισέλθουν στην περιοχή απογύμνωσης.

(a)   (b)
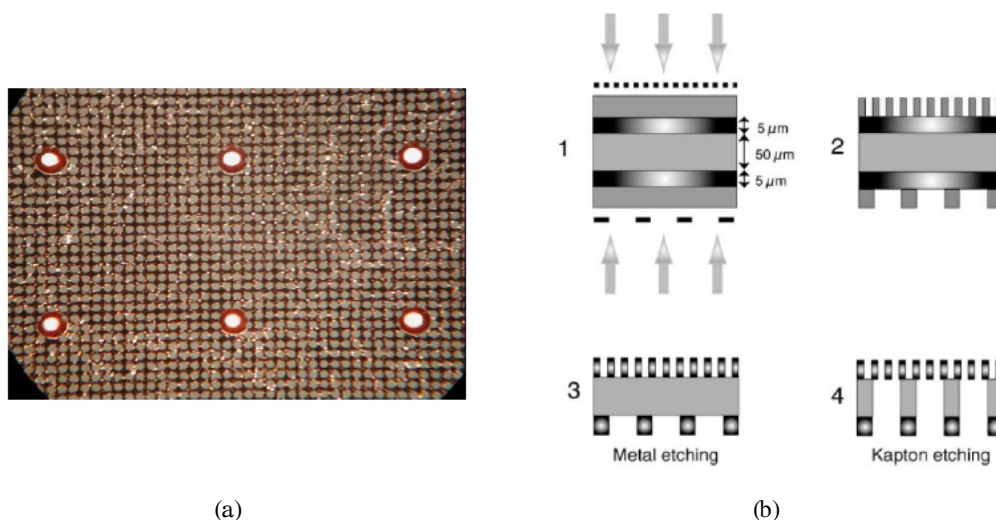
Figure 1.5: (a) Φωτογραφία του micromesh που λήφθηκε μέσω τηλεσκοπίου. (b) Η διαδικασία της φωτολιθογραφίας που ακολουθείται κατά την κατασκευή ενός ανιχνευτή micromegas.

Καθώς τα ιόντα συγκεντρώνονται από το πλέγμα με μεγάλη αποδοτικότητα και ταχύτητα, τα ηλεκτρόνια συνεχίζουν στην περιοχή ενίσχυσης και ολοκληρώνουν το ταξίδι τους στο ηλεκτρόδιο ανόδου(strips). Τα strips είναι λωρίδες χαλκού, πλάτους $150 - 350\mu m$ τοποθετημένα σε απόσταση $200\mu m$ (από το μέσο του πλάτους τους) μεταξύ τους. Όλα τα strips μαζί μας δίνουν το ηλεκτρόδιο της ανόδου το οποίο μας δίνει και χωρικές πληροφορίες. Τα strips μπορούν να έχουν οποιοδήποτε σχήμα. Μπορούν να έχουν μορφή λωρίδων ώστε να παίρνουμε χωρικές πληροφορίες μόνο για τον ένα άξονα, ή να έχουν μορφή pixels και να παίρνουμε πληροφορίες και για τους δύο άξονες X-Y. Έχουν κατασκευαστεί strips σε διάφορες μορφές

ανάλογα με τις ανάγκες του εκάστοτε πειράματος και τη χρήση του ανιχνευτή.

1.4.2   Αρχή λειτουργίας του ανιχνευτή Micromegas

Ο θάλαμος του ανιχνευτή περιέχει αέριο μείγμα που αποτελείται άπω αργό και ένα δεύτερο αέριο(συνήθως ισοβουτάνιο ή διοξείδιο του άνθρακα) η αναλογία των οποίων ποικίλει ανάλογα με την εφαρμογή. Όταν ένα φορτισμένο σωματίδιο ή ένα φωτόνιο εισέλθει στον θάλαμο στο conversion gap αλληλεπιδρά με τα άτομα του αργού μέσω ενός απο τους γνωστούς μηχανισμούς και ιονίζει τα άτομα του αερίου. Έτσι έχουμε τη δημιουργία ζευγών ελευθέρων ηλεκτρονίων και ιόντων. Τα ελεύθερα ηλεκτρόνια αυτά που ονομάζονται αρχικά ηλεκτρόνια ιοντισμού (primary ionization electrons) λόγω της διαμόρφωσης του ηλεκτρικού πεδίου του conversion gap υπό κατάλληλες συνθήκες περνούν σχεδόν στο δεύτερο μέρος του θαλάμου (amplification gap). Εκεί εξ' αιτίας της μικρής απόστασης μεταξύ του mesh και των strips, το ηλεκτρικό πεδίο στην περιοχή αυτή είναι πολύ πιο ισχυρό και έτσι έχουμε τον περαιτέρω ιονισμό του αερίου. Έχουμε πολλαπλασιασμό των ζευγών ηλεκτρονίων-ιόντων και εμφάνιση του φαινομένου της χιονοστιβάδας και λόγω του ηλεκτρικού πεδίου τα ηλεκτρόνια κινούνται προς την άνοδο(strips) και τα θετικά ιόντα να κινούνται προς το mesh. Έτσι έχουμε τη δημιουργία περίσσειας φορτίου το οποίο συλλέγεται από τα strips. Η ποσότητα του φορτίου που συλλέγεται είναι ανάλογη της αρχικής ενέργειας του σωματιδίου ή φωτονίου που ήταν υπεύθυνο για τον πρώτο ιονισμό μορίου του αργού. Λαμβάνοντας υπόψη όλες τις παραμέτρους (γεωμετρία, ηλεκτρικό πεδίο, είδος αερίου) υπολογίζουμε την ενέργεια του αρχικού σωματιδίου.

1.5   Πειραματική διάταξη

σ Το πειραματικό μέρος της παρούσας εργασίας διεξήχθη στο Ευρωπαϊκό Κέντρο Πυρηνικών Ερευνών (CERN) και συγκεκριμένα στις εγκαταστάσεις SPS/H4[1]. Η πειραματική διάταξη που εγκαταστάθηκε αποτελείται από τον πρωτότυπο ανιχνευτή micromegas που κατασκευάστηκε από την ομάδα του LAPP[2], ένα τηλεσκόπιο micromegas για τον προσδιορισμό των τροχιών των σωματιδίων, ενώ ως σύστημα σκανδαλισμού χρησιμοποιήθηκαν σπινθηριστές σε συνδυασμό με φωτοπολλαπλασιαστές. Τα πειράματα διήρκεσαν 18 ημέρες, όπου χρησιμοποιήθηκαν δέσμες μιονίων και πιονίων. Η πειραματική διάταξη φαίνεται στις παρακάτω εικόνες.

1.5.1   Το τηλεσκόπιο micromegas

Το τηλεσκόπιο micromegas κατασκευάστηκε στα πλαίσια της διεθνούς συνεργασίας με το όνομα RD51, απο τις ομάδες του Εθνικού Μετσοβίου Πολυτεχνείου και του ΕΚΕΦΕ Δημόκριτος. Αποτελείται από τρεις σταθμούς, κάθε ένας από τους οποίους απαρτίζεται από ένα διπλό ανιχνευτή micromegas. Ο όρος διπλός, χρησιμοποιείται για να περιγράψει τη χαρακτηριστική δομή του κάθε σταθμού, όπου ένα κοινό επίπεδο οριοθετείται απο το ηλεκτρόδιο του drift, αριστερά και δεξιά του οποίου τοποθετούνται τα ηλεκτρόδια του mesh και οι πλακέτες PCB που περιέχουν τα strips, συγκροτώντας έτσι το διπλό ανιχνευτή.

Με αυτή τη δομή, μπορούμε να έχουμε πληροφορία την θέση σε δύο διατάσεις χρησιμοποιώντας κατάλληλα την πληροφορία από τα strips για X και Y επίπεδο ενώ είναι δυνατή η χρήση μόνο τριών γραμμών υψηλής τάσης (μια για κάθε ηλεκτρόδιο). Κάθε PCB περιέχει 96 strips που

---

[1] Super Proton Synchrotron
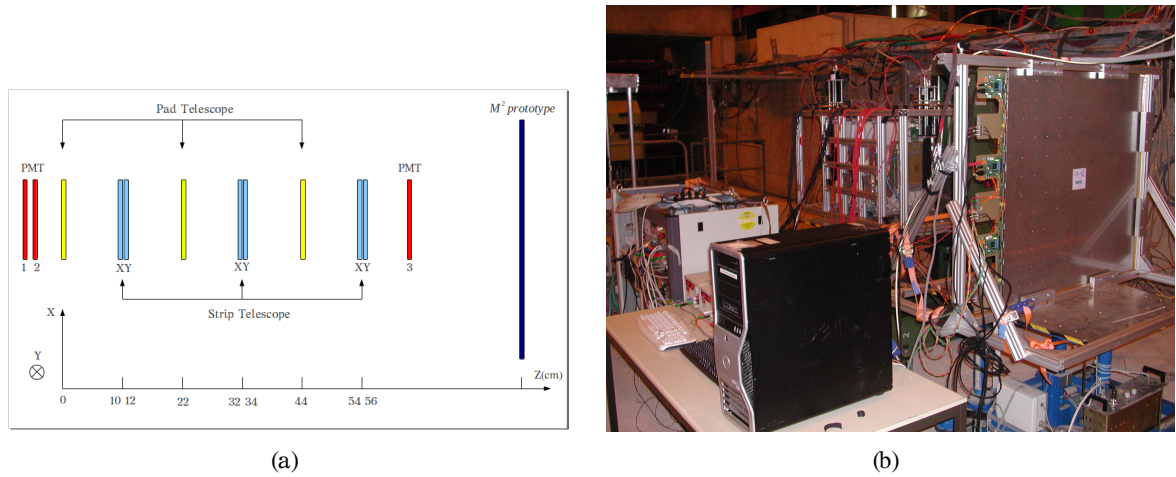[2] Laboratoire d'Annecy-le-Vieux de Physique des Particules - CNRS/IN2P3

(a)

(b)

Figure 1.6: (a) Αναπαράσταση της πειραματικής διάταξης που χρησιμοποιήθηκε. (b) Φωτογραφία απο τον χώρο που διεξήχθησαν τα πειράματα.

τοποθετούνται σε απόσταση $250 \mu m$ το ένα από το άλλο, δημιουργώντας μια ενεργή περιοχή 2.4×10 *cm*, ενώ ο συνδυασμός δύο PCB δημιουργεί μια συνολική ενεργή περιοχή στις δύο διστάσεις, της τάξης των 2.4×2.4 cm ($96 \times 250 \mu m = 2.4$ cm). Μια σχηματική αναπαράσταση για ένα σταθμό του τηλεσκοπίου φαίνεται στο σχήμα (5.3)

(a) The station

(b) The strips
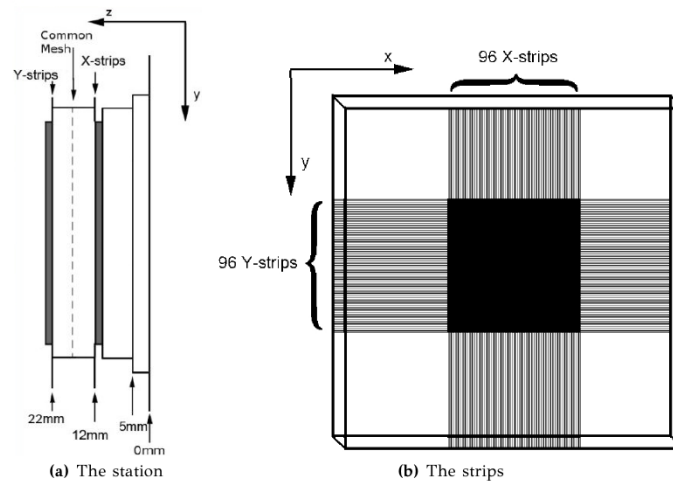
Figure 1.7: (a) Σχηματική αναπαράσταση ενός διπλού σταθμού micromegas (b) Σχηματική αναπαράσταση του ενεργού χώρου που δημιουργείται από τις δύο PCB κάθε σταθμού. Η συνολική ενεργή περιοχή (2.4×2.4 *cm*) είναι το τετράγωνο με το μαύρο χρώμα στο κέντρο του σταθμού.

1.6 Ο πρωτότυπος ανιχνευτής **micromegas** διαστάσεων 1×1 m^2.

1.6.1 Η δομή του ανιχνευτή

Ο συγκεκριμένος ανιχνευτής έχει διαστάσεις 1×1 m^2 και διαθέτει 9216 κανάλια ανάγνωσης (or 96×96 pads). Αποτελείται από έξι ASU (Active Sensor Units), οι οποίες συνδυάζονται ανά δύο και τοποθετούνται σε ένα ατσάλινο πλαίσιο. Στη συνέχεια τοποθετείται μια πλαστική μάσκα

Figure 1.8: Φωτογραφίες του πρωτότυπου ανιχνευτή κατα τη διάρκεια της συναρμολογησης.

και άλλο ένα πλαίσιο που περιλαμβάνει το ηλεκτρόδιο του drift. Μεταξύ δύο ASU βρίσκεται ένα κομμάτι πλαστικού 5*mm*, για λόγους στήριξης. Η περιοχή μετατροπής οριοθετείται από το πλαίσιο που περιέχει το drift, για τη στήριξη του οποίου στα 3*mm* πάνω από το mesh χρησιμοποιούνται μικροσκοπικά στηρίγματα σε όλη την έκ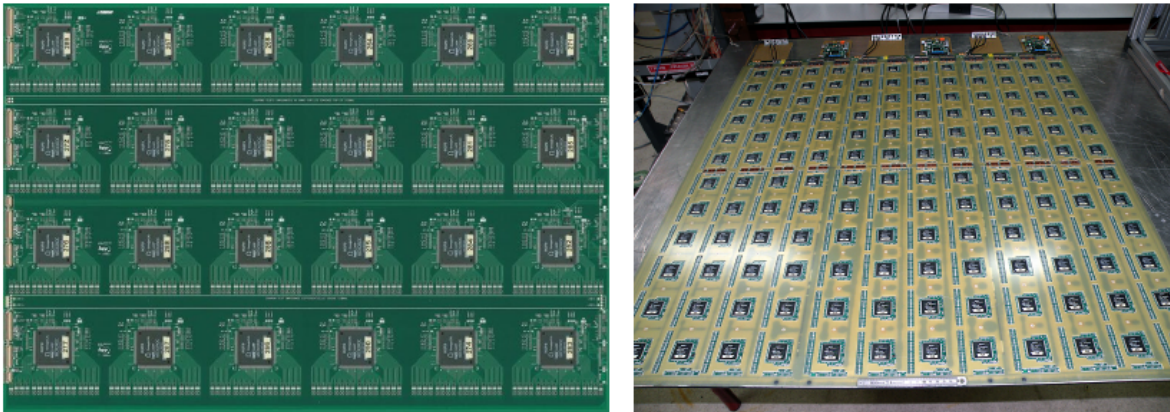ταση του ανιχνευτή. Κάθε ASU αποτελείται από το mesh και μια PCB με 48×32 μπλόκ ανάγνωσης διαστάσεων 1×1 cm^2, ενώ περιλαμβάνει συνολικά 24 MICROROC chips, όπως φαίνεται στο σχήμα 5.5.
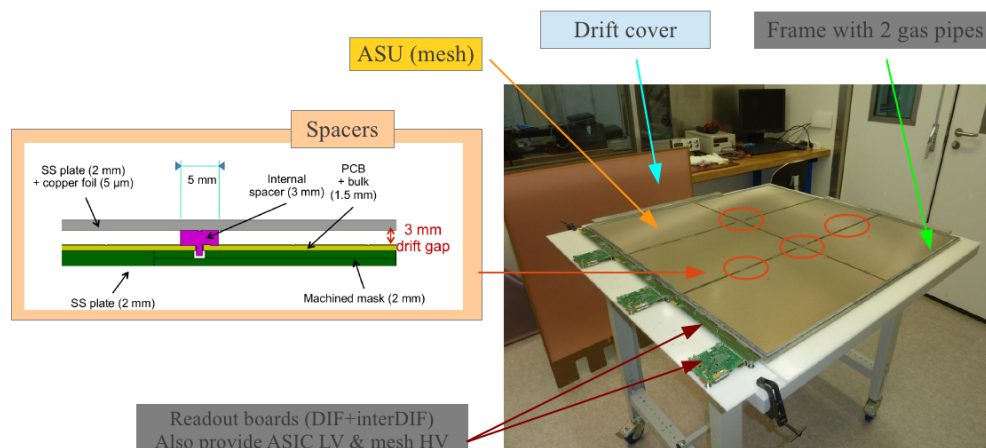
Figure 1.9: Νεκρές περιοχές του ανιχνευτή λόγω των υλικών που χρησιμοποιούνται για την στήριξη των επιμέρους κομματιών.

1.6.2 MICROROC chip.

Το MICROROC είναι ένα ολοκληρωμένο κύκλωμα που περιλαμβάνει 64 κανάλια και κατασκευά-ζεται με τεχνολογία SiGe 0.35*μm*. Τα συγκεκριμένα chip σχεδιάζονται για χρήση ως ηλεκτρονικά ανάγνωσης στον ILC όπου ο μεγάλος αριθμός των καναλιών σε συνδυασμό με τις μειωμένες διαστάσεις που απαιτούνται, οδηγεί σε χρήση ηλεκτρονικών ενσωματωμένων πάνω στους ανιχνευτές. Το ολοκληρωμένο καλύπτει μια περιοχή 20 mm^2 και κάθε κανάλι (Fig 5.7), αποτελείται από:

- Ένα σύστημα προστασίας από εκφορτίσεις.

- Ένα προενισχυτή.

- Δύο διαμορφωτές παλμού (για λειτουργία χαμηλής και υψηλής ενίσχυσης).

- Τρείς διευκρινιστές με κωδικοποίηση δύο ψηφίων.

- Ένα σύστημα μνήμης.

- Ένα μετρητή διέλευσης 24 ψηφίων που λειτουργεί στα 5MHz(BCID).

Figure 1.10: Σχηματική απεικόνιση του ολοκληρωμένου κυκλώματος του MICROROC.

1.7   Ανάλυση δεδομένων του πειράματος

Η πειραματική διάταξη εγκαταστάθηκε για 18 μέρες στην γραμμή SPS/H4 Αύγουστο του 2011. Με ένα μέσο όρο σκανδαλισμών $100\,\mathrm{Hz}$ per spill, πάνω απο 6 εκατομμύρια γεγονότα καταγράφη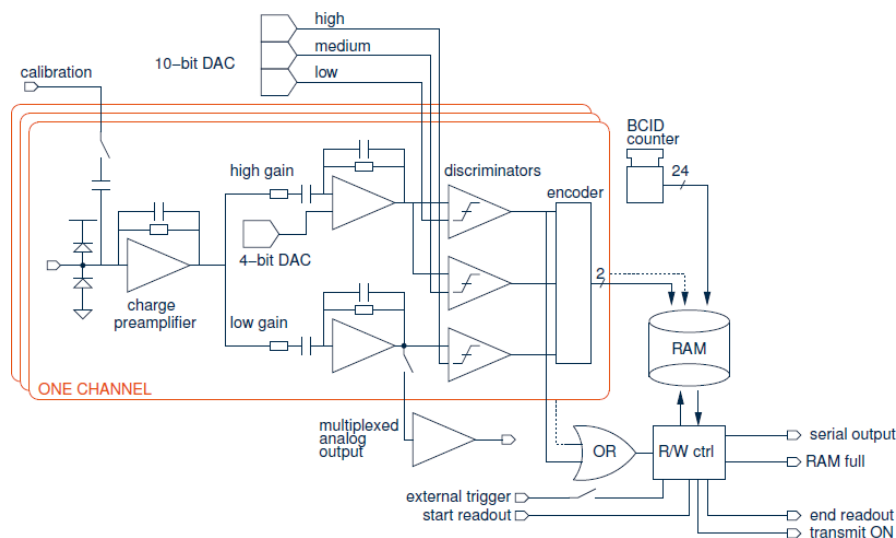καν, χρησιμοποιώντας δέσμες μιονίων και πιονίων σε αναλογία 85/15. Τα μιονια χρησιμοποιήθηκαν για τη μελέτη της αποδοτικότητας του ανιχνευτή κάτω απο διάφορες συνθήκες, ενώ τα πιόνια χρησιμοποιήθηκαν για τη δημιουργία αδρονικών καταιγισμών έτσι ώστε να μελετηθεί η απόκριση του ανιχνευτή. Οι καταιγισμοί αυτοί παράχθηκαν με τη βοήθεια ενός τούβλου απο σίδηρο που τοποθετήθηκε ανάμεσα στο τηλεσκόπιο και το πρωτότυπο.

Για όλους τους ανιχνευτές χρησιμοποιήθηκε ένα μη έφλεκτο αέριο μίγμα $Ar/CF_4/iC_4H_{10}$ 95/3/2, με συνολική ροή $4\,\mathrm{l/h}$. Οι ανιχνευτές του τηλεσκοπίου ήταν σταθερά ρυθμισμένοι σε τάση $420V$ για το mesh και $530V$ για το drift ενώ οι φωτοπολλαπλασιαστές 1,2 and 3 ήταν ρυθμισμένοι στα $1700V$, $1750V$ και $1750V$ αντίστοιχα.

1.7.1   Αλγόριθμος εύρεσης των cluster.

Όταν ένα σωματίδιο εισέλθει στην ενεργή περιοχή του ανιχνευτή, ιονίζει τα άτομα του αερίου και στη συνέχεια έχουμε τη γνωστή διαδικασία της χιονοστιβάδας έτσι ώστε να έχουμε ένα παλμό στην άνοδο. Στον ανιχνευτή micromegas ο ιονισμός γίνεται στο conversion gap, ενώ με την παρουσία ηλεκτρικού πεδίου τα ηλεκτρόνια εισέρχονται στο amplification gap, όπου και τελικά έχουμε την ενίσχυση του φορτίου το οποίο καταλήγει στα strips.

Στην πλειοψηφία των περιπτώσεων το μέγεθος της χιονοστιβάδας είναι μεγαλύτερο από το μέγεθος ενός strip, με αποτέλεσμα το φορτίο να εναποτίθεται σε περισσότερα από ένα strip. Αυτό οδηγεί στη δημιουργία συμπαγών ομάδων ενεργοποιημένων strips, που είναι γνωστές και ως cluster. Τα cluster, περιέχουν όλη την πληροφορία για το σωματίδιο που πέρασε από τον ανιχνευτή. Συνεπώς, ένας αλγόριθμος για την εύρεση των cluster και τον υπολογισμό των ιδιοτήτων τους είναι απαραίτητος.

Στα πλαίσια της εργασίας αυτής, κατασκευάστηκε ένας αλγόριθμος, ικανός να υπολογίζει των αριθμό των cluster για κάθε γεγονός αλλά και την ακριβή θέση τους, το μέγεθος τους και το συνολικό τους φορτίο. Η μέθοδος πάνω στην οποία βασίζεται ο αλγόριθμος περιγράφεται παρακάτω:
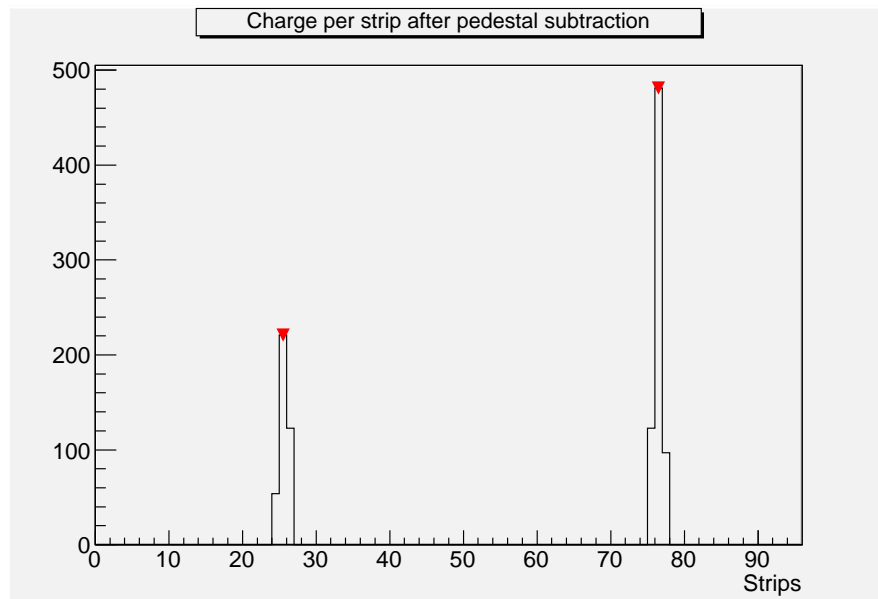

Figure **1.11**: Ένα γεγονός με δύο clusters. Ο αλγόριθμος ξεκινά απο την κορυφή του από το cluster με την υψηλότερη κορυφή (δεξιά) και συνεχίζει με το δεύτερο cluster.

- Κατασκευάζει το ιστόγραμμα που απεικονίζει το φορτίο για κάθε strip. Έτσι επιτυγχάνεται η κατάταξη των strip με τη σωστή σειρά και υπάρχει η παρέχεται η δυνατότητα για μια πρώτη ματιά στο γεγονός.

- Στη συνέχεια αναζητητά κορυφές στο ιστόγραμμα, οι οποίες υποδεικνύουν την ύπαρξη cluster.

- Ξεκινώντας από την υψηλότερη κορυφή βρίσκει την αρχή και το τέλος του cluster.

- Τέλος, αφού έχει υπολογίσει την αρχή και το τέλος, υπολογίζει το μέγεθος, το φορτίο και την ακριβή θέση του κάθε cluster με βάση τα strip που έχουν ενεργοποιηθεί. Η θέση x του cluster μεγέθους N δίνεται από το βαρύκεντρο τη κατανομής του φορτίου για κάθε cluster, όπου x_i είναι η θέση του κάθε strip και Q_i το φορτίο:

$$x = \frac{\sum_{i=1}^{N} x_i \cdot Q_i}{\sum_{i=1}^{N} Q_i}$$

- Αν στο συγκεκριμένο γεγονός υπάρχουν περισσότερα από ένα cluster, τότε ο αλγόριθμος συνεχίζει με την δεύτερη υψηλότερη κορυφή κ.ο.κ. αλλιώς συνεχίζει με το επόμενο γεγονός.

1.7.2 Ευθυγράμμιση του τηλεσκοπίου.

Μετά τον υπολογισμό του αριθμού των cluster και των ιδιοτήτων τους, είμαστε σε θέση να ανακατασκευάσουμε τις τροχιές των σωματιδίων που πέρασαν μέσα απο τον ενεργό όγκο του τηλεσκοπίου. Ωστόσο, για να γίνει αυτό θα πρέπει το τηλεσκόπιο να είναι ευθυγραμισμένο, γιατί όπως είναι λογικό οι σταθμοί δε βρίσκονται ακριβώς στην ίδια θέση και αυτό οφείλεται είτε στον ανθρώπινο παράγοντα είτε σε αποκλίσεις που δημιουργήθηκαν κατά τη μεταφορά και εγκατάσταση της διάταξης στο CERN. Η ευθυγράμμιση γίνεται με την ακόλουθη μέθοδο:

- Κρατάμε τον πρώτο σταθμό ως επίπεδο αναφοράς.

- Κατασκευάζουμε ένα δείγμα από γεγονότα με ένα cluster για τους σταθμούς που μετρούν τη θέση στο X επίπεδο και αντίστοιχα για το Y επίπεδο.

- Υπολογίζουμε τη διαφορά της θέσης του cluster:

  ▶ $2^{ος}$ σταθμός - $1^{ος}$ σταθμός.

  ▶ $3^{ος}$ σταθμός - $1^{ος}$ σταθμός.

- Κατασκευάζουμε το ιστόγραμμα των διαφορών και προσαρμόζουμε μια Γκαουσιανή.

- Η μέση τιμή που προκύπτει από την προσαρμογή είναι η ζητούμενη απόκλιση που πρέπει να διορθώσουμε.

Η εφαρμογή αυτής της μεθόδου για τους ανιχνευτές του τηλεσκοπίου έδωσε τα ακόλουθα αποτελέσματα:

Table 1.1: Απόκλιση του $2^{ου}$ και $3^{ου}$ σταθμού όταν ο $1^{ος}$ λαμβάνεται ως επίπεδο αναφοράς.

Σταθμός	Απόκλιση [strips]	Απόκλιση [mm]
$2^{ος}$ X-επίπεδο	-1.996	-0.499
$2^{ος}$ Y-επίπεδο	-12.34	-3.085
$3^{ος}$ X-επίπεδο	+2.857	+0.714
$3^{ος}$ Y-επίπεδο	-1.307	-0.326

1.7.3 Ανακατασκευή των τροχιών

Για την ανακατασκευή των τροχιών, χρησιμοποιήθηκε ο αλγόριθμος εύρεσης τροχιών του RD51[3]. Ο αλγόριθμος αυτός είναι κατάλληλος για χρήση σε τηλεσκόπια Micromegas και GEM και βασίζεται στον μετασχηματισμό Hough για την εύρεση των τροχιών. Ο χρήστης παρέχει σαν είσοδο των αριθμό και την θέση των, όπου στην έξοδο θα λάβει ένα αρχείο με όλη την απαραίτητη πληροφορία για τις τροχιές των σωματιδίων.

Για γεγονότα με ένα cluster σε X και Y επίπεδο, δημιουργούνται τρία σημεία στο χώρο από τα οποία προκύπτει η τροχιά. Ωστόσο για λόγους απλότητας, παίρνουμε την προβολή κάθε σημείου στις δυο διαστάσεις, έχοντας πλέον να αντιμετωπίσουμε ένα πιο εύκολο πρόβλημα.

1.7.4 Χωρική διακριτική ικανότητα των θαλάμων του τηλεσκοπίου

Εφόσον γνωρίζουμε τις παραμέτρους των τροχιών, μπορούμε να μετρήσουμε τη χωρική διακριτική ικανότητα για κάθε σταθμό του τηλεσκοπίου. Για να μετρήσουμε την ενδογενή χωρική
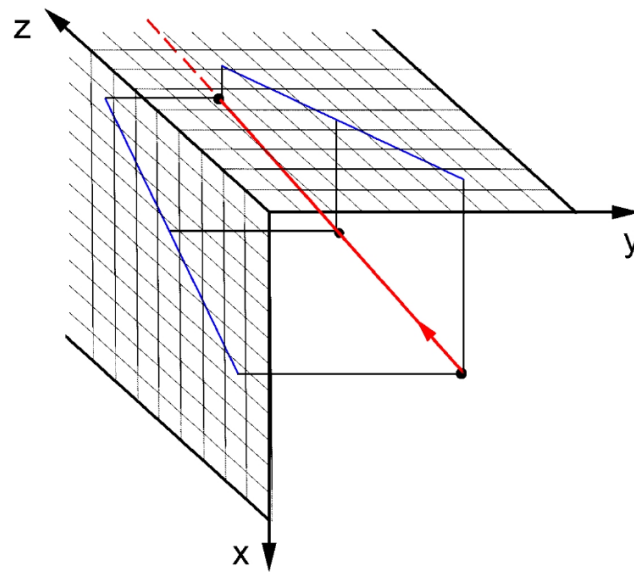
---

[3]Developed by K.Karakostas.

Figure 1.12: Προβολη των σημείων και κατα συνέπεια της τροχιάς απο τις τρεις (XYZ) στις δύο (X-Z and Y-Z) διαστάσεις.
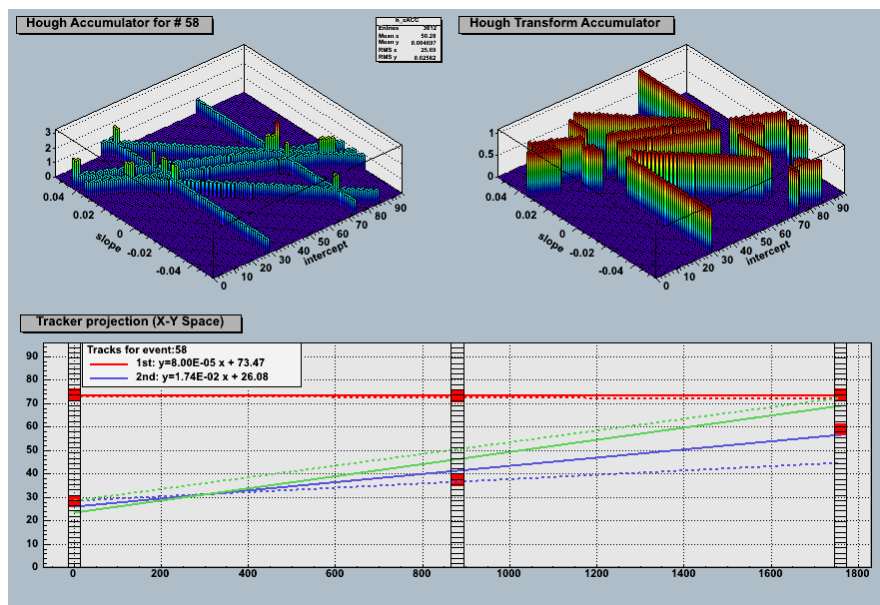

Figure 1.13: Ένα γεγονός με δύο τροχιές όπως απεικονίζεται στο κύριο παράθυρο του γραφικού περιβάλλοντος του αλγόριθμου εύρεσης τροχιών.

διακριτική ικανότητα, χρησιμοποιήσαμε την εξής μέθοδο:

- Φτιάχνουμε ένα δείγμα γεγονότων που περιέχουν μια τροχιά και στο Χ και στο Υ επίπεδο.

- Υπολογίζουμε την κατανομή των υπολοίπων για κάθε σταθμό, τα οποία είναι η διαφορά της θέσης του cluster από τη θέση την οποία προβλέπει η τροχιά (fig. 6.23(a)). Η κατανομή αυτή δίνει το $\sigma_{included}$

- Επαναλαμβάνουμε την διαδικασία αυτή, μόνο που τώρα δε περιλαμβάνουμε τον υπο μελέτη σταθμό και προσαρμόζουμε μια ευθεία γραμμή χρησιμοποιώντας τους υπόλοιπους σταθμούς. Τα υπόλοιπα σε αυτή την περίπτωση είναι η διαφορά της θέσης του cluster από την ευθεία που προσαρμόσαμε (fig. 6.23(b)). Η κατανομή αυτή δίνει το $\sigma_{excluded}$
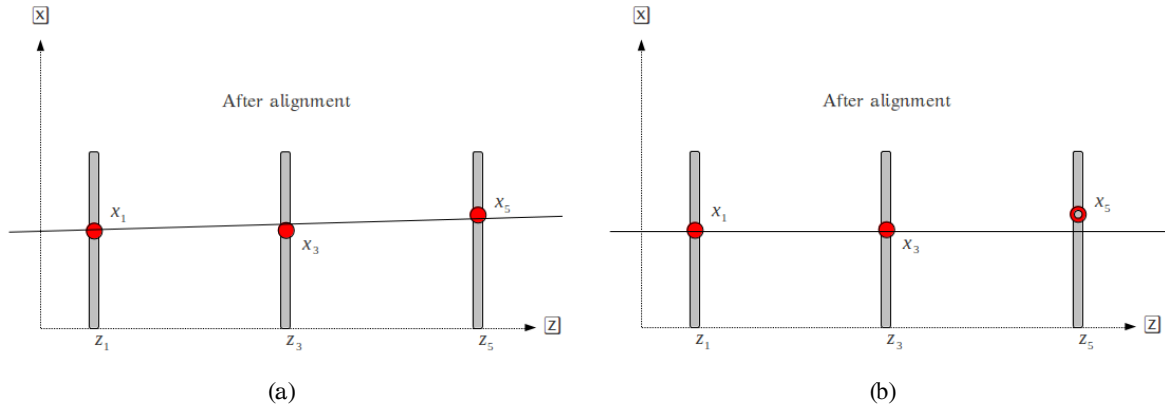

(a)   (b)

Figure 1.14: Αναπαράσταση της μεθόδου για τον υπολογισμό της χωρικής διακριτικής ικανότητας κάθε ανιχνευτή. Κατασκευάζουμε την κατανομή των υπολοίπων, λαμβάνοντας υπ'όψη όλους τους σταθμούς (a) και εξαιρώντας τον υπό μελέτη σταθμό (b).

Η ενδογενής διακριτική ικανότητα κάθε ανιχνευτή δίδεται από τον γεωμετρικό μέσο των διασπορών των δύο κατανομών, όπως φαίνεται στην εξίσωση 6.1. Εφαρμόζοντας την συγκεκριμένη μέθοδο, υπολογίστηκε η ενδογενής χωρική διακριτική ικανότητα για κάθε ανιχνευτή. Τα αποτελέσματα φαίνονται στον πίνακα 1.2

$$\sigma_{total} = \sqrt{\sigma_{included} \cdot \sigma_{excluded}}$$ (1.1)

Table 1.2: Ενδογενής χωρική διακριτική ικανότητα των θαλάμων του τηλεσκοπίου.

chamber	$\sigma_{included}[strip]$	$\sigma_{excluded}[strip]$	$\sigma_{total}[strip]$	$\sigma_{total}[\mu m]$
1	0.116955	0.655224	0.278928	69.73
2	0.106858	0.59539	0.252234	63.06
3	0.225735	0.336798	0.275730	68.93
4	0.205426	0.588961	0.347833	86.95
5	0.116955	0.665224	0.278928	69.73
6	0.106858	0.59539	0.252234	63.06

1.7.5 Μελέτη της αποδοτικότητας του πρωτοτύπου.

Για να μετρήσουμε την αποδοτικότητα του μεγάλου ανιχνευτή, χρησιμοποιήσαμε τις τροχιές που προέκυψαν από το τηλεσκόπιο. Ένα δείγμα καθαρών γεγονότων (αυστηρά ένα cluster

σε κάθε ανιχνευτή του τηλεσκοπίου και για X και για Y επίπεδο) δημιουργήθηκε. Επίσης εφαρμόστηκαν περιορισμοί στον χρονισμό των γεγονότων αλλά και στη θέση, για να απορρίψουμε όσο το δυνατόν ακριβέστερα γεγονότα που οφείλονται στο θόρυβο.

Για κάθε γεγονός του δείγματος, επεκτείνουμε την τροχιά στο επίπεδο του μεγάλου ανιχνευτή και ψάχνουμε για ενεργοποιημένα pad σε μια περιοχή ±3 pad απο τη θέση όπου στοχεύει η τροχιά. Αν υπάρχει ενεργοποιημένο pad τότε σημαίνει οτι μεγάλος ανιχνευτής είναι αποδοτικός (εικόνα 7.4(a)) για το συγκεκριμένο γεγονός, αντίθετα αν δεν υπάρχει, τότε δεν είναι αποδοτικός (εικόνα 7.4(b)). Ο λόγος των γεγονότων του δείγματος στα οποία είναι αποδοτικός ο ανιχνευτής προς το συνολικό αριθμό των γεγονότων του δείγματος είναι η αποδοτικότητα του ανιχνευτή
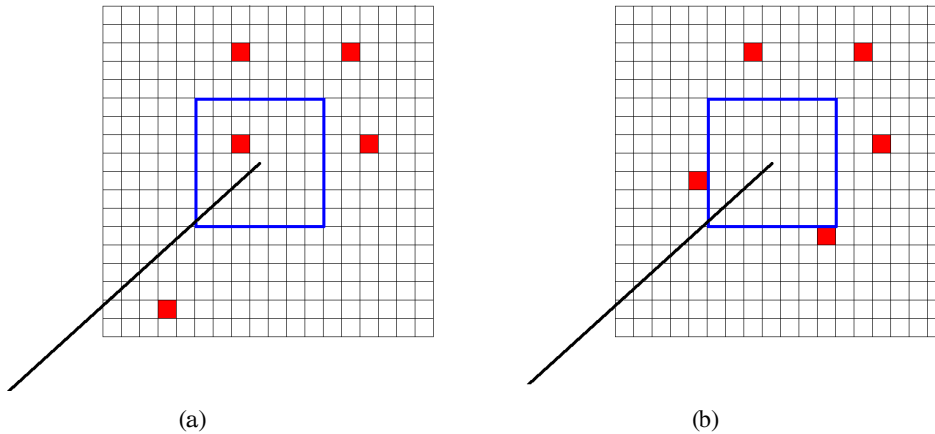

(a)   (b)

Figure 1.15: Αναπαράσταση ενός γεγονότος στο οποίο ο μεγάλος ανιχνευτής είναι αποδοτικός (a) και ενός γεγονότος στο οποίο δεν είναι αποδοτικός (b).

Το σφάλμα $\delta\epsilon$ στην αποδοτικότητα υπολογίζεται σύμφωνα με τον παρακάτω τύπο ο οποίος προκύπτει από την διωνυμική κατανομή:

$$\delta\epsilon = \sqrt{\frac{\epsilon \cdot (1-\epsilon)}{N_{total}}}$$

όπου ϵ είναι η αποδοτικότητα και N_{total} ο συνολικός αριθμός των γεγονότος του υπό μελέτη δείγματος. Η αποδοτικότητα μετρήθηκε για διάφορες συνθήκες. Τα αποτελέσματα που προέκυψαν παρουσιάζονται στα γραφήματα 1.16, 1.17 και 1.18.

1.7.6   Μέτρηση της πολλαπλότητας

Για να μετρηθεί η πολλαπλότητα, χρησιμοποιήθηκε το ίδιο δείγμα καθαρών γεγονότων με τη μελέτη της αποδοτικότητας. Για κάθε γεγονός, μετριέται ο αριθμός των ενεργοποιημένων pad μέσα στη περιοχή των ±3 pad γύρω από το σημείο που στοχεύει η τροχιά. Η μέση τιμή του αριθμού των ενεργοποιημένων pad για όλα τα γεγονότα του δείγματος είναι η πολλαπλότητα. Τα αποτελέσματα που προέκυψαν φαίνονται στα γραφήματα 1.19, 1.20, 1.21 και 1.22

1.7.7   Επίδραση των νεκρών περιοχών στην απόδοση του ανιχνευτή.

Ένα από τα πιο σημαντικά πράγματα για τον μεγάλο ανιχνευτή είναι να κατανοήσουμε την επίδραση των νεκρών περιοχών, λόγω των υλικών που τοποθετούνται για τη στήριξη των
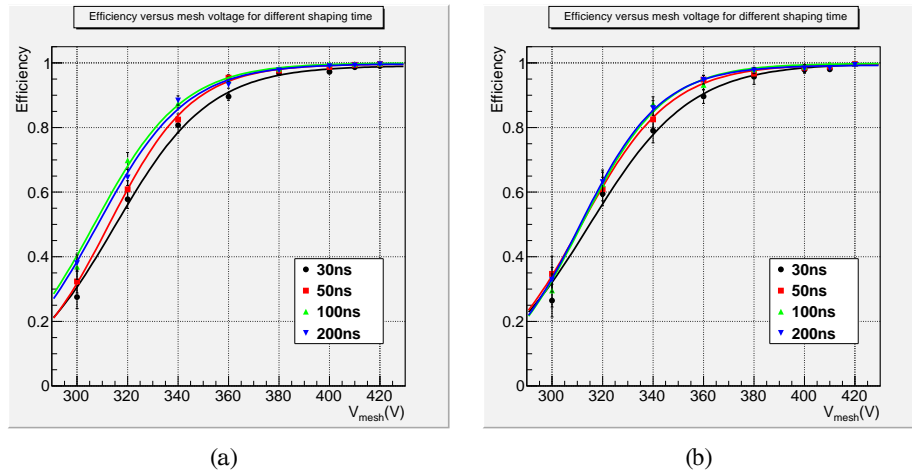
Figure 1.16: Αποδοτικότητα συναρτήσει της τάσης στο mesh για διάφορα shaping time για X (a) και Y (b) επίπεδο.
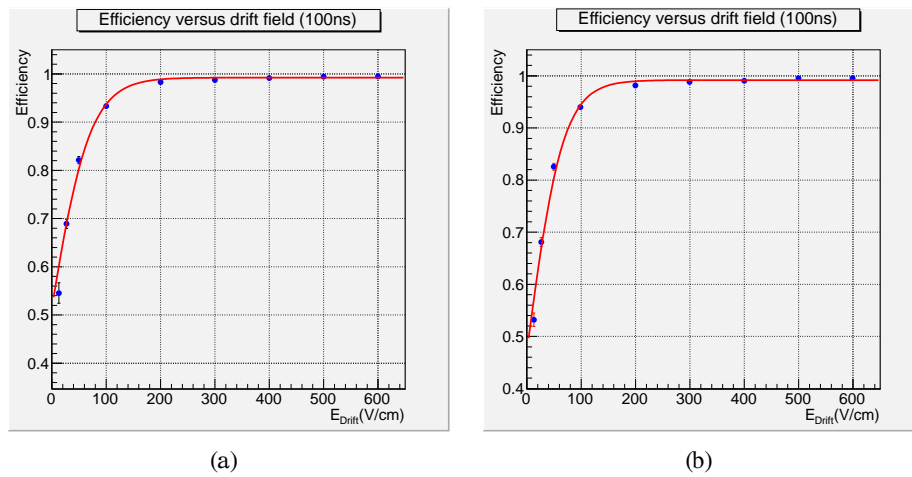

Figure 1.17: Αποδοτικότητα συναρτήσει του ηλεκτρικού πεδίου στην περιχή μετροπής για X (a) και Y (b) επίπεδο.

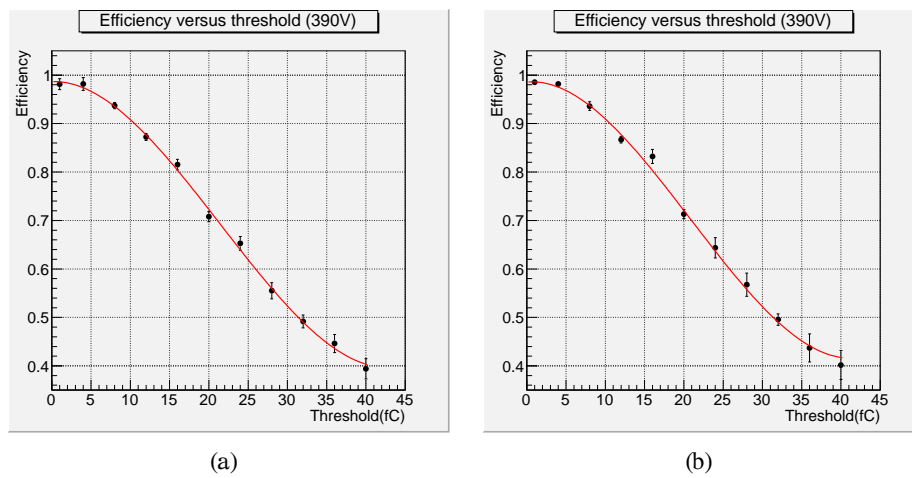**Figure 1.18**: Αποδοτικότητα συναρτήσει του κατωφλίου πάνω από το οποίο ένα σήμα θεωρείται πραγματικό για X (a) και Y (b) επίπεδο.

(a)   (b)

Figure 1.19: Πολλαπλότητα συναρτήσει της τάσης στο mesh για διάφορα shaping time για Χ (a)
και Υ (b) επίπεδο.

(a)   (b)

Figure 1.20: Πολλαπλότητα συναρτήσει του ηλεκτρικού πεδίου στην περιοχή μετατροπής για Χ
(a) και Υ (b) επίπεδο.

(a)   (b)

Figure 1.21: Πολλαπλότητα συναρτήσει του κατωφλίου πάνω από το οποίο ένα σήμα θεωρείται
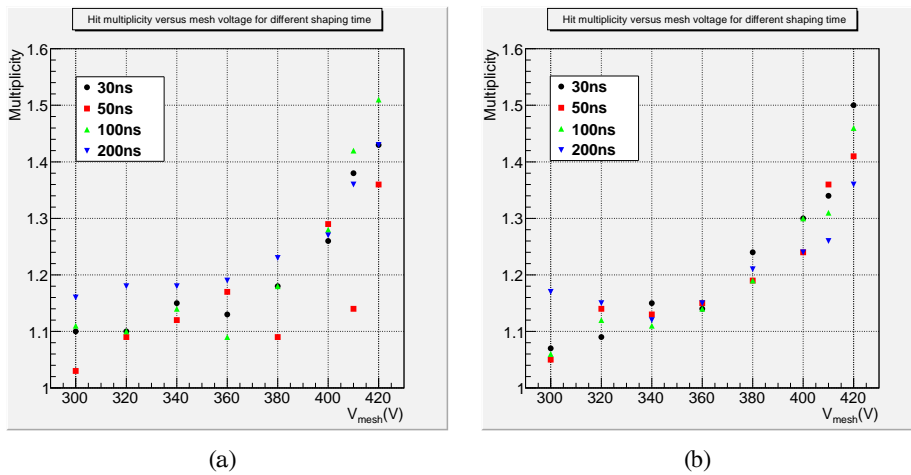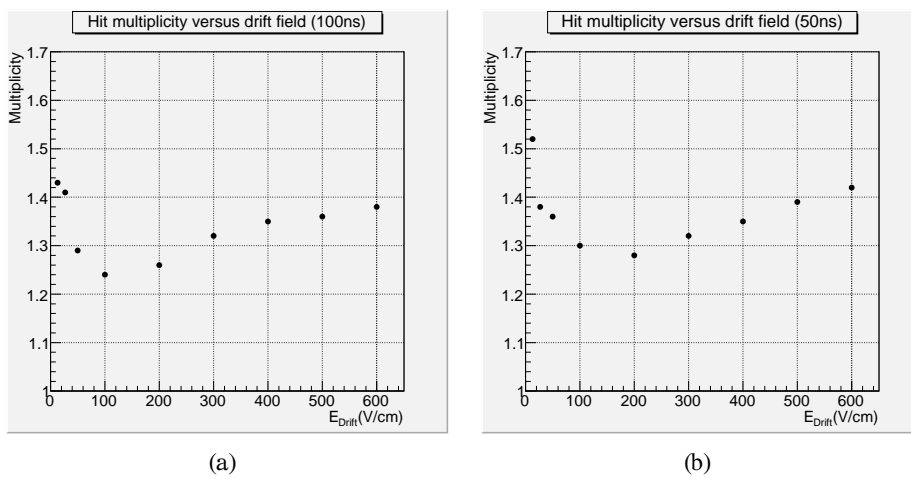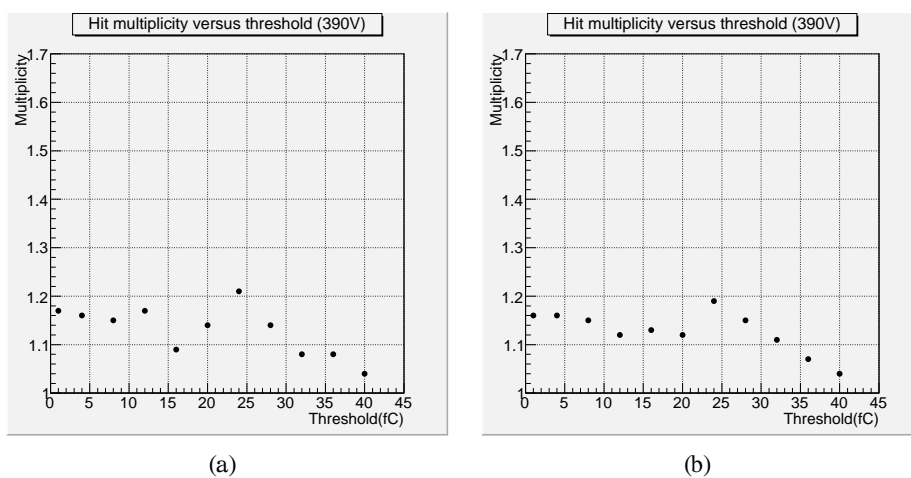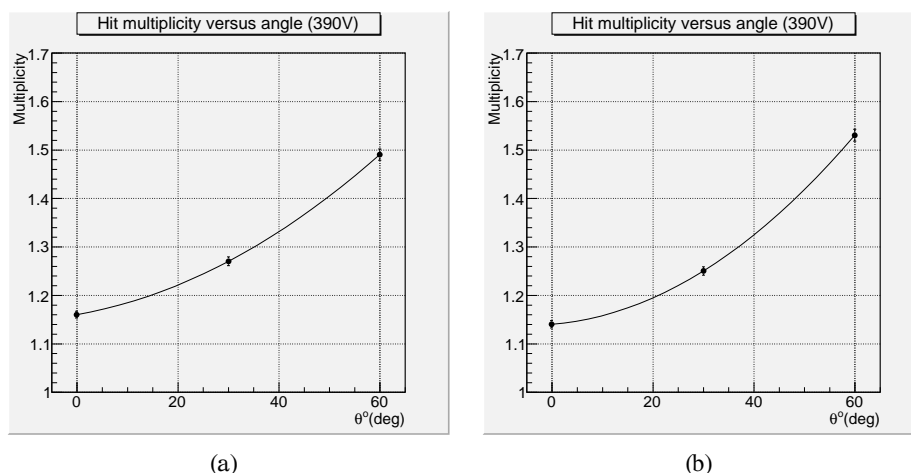πραγματικό για Χ (a) και Υ (b) επίπεδο.

Figure 1.22: Πολλαπλότητα συναρτήσει της γωνίας πρόσπτωσης της δέσμης για X (a) και Y (b) επίπεδο.

επιμέρους κομματιών, στην απόδοση του ανιχνευτή. Για να γίνει αυτό κατασκευάζουμε τους χάρτες αποδοτικότητας του ανιχνευτή και έτσι μπορούμε να εκτιμήσουμε την πτώση στην απόδοση του ανιχνευτή λόγω των νεκρών περιοχών

Με διακριτική ικανότητα της τάξης των 1.2 *mm* για την επέκταση των τροχιών στο επίπεδο του μεγάλου ανιχνευτή. Χρησιμοποιώντας δεδομένα στα οποία η δέσμη ήταν κεντραρισμένη στην νεκρή περιοχή μεταξύ δύο ASU καταφέραμε να κάνουμε μια πρώτη εκτίμηση για πτώση μεγαλύτερη από 80% στη αποδοτικότητα του ανιχνευτή (εικόνα 7.14). Αντίθετα δεν παρατηρείται κάποια πτώση αν παρατηρήσουμε το χάρτη αποδοτικότητας για μια ενεργή περιοχή του ανιχνευτή αλλά η απόδοση είναι ομοιόμορφη (εικόνα 7.15).
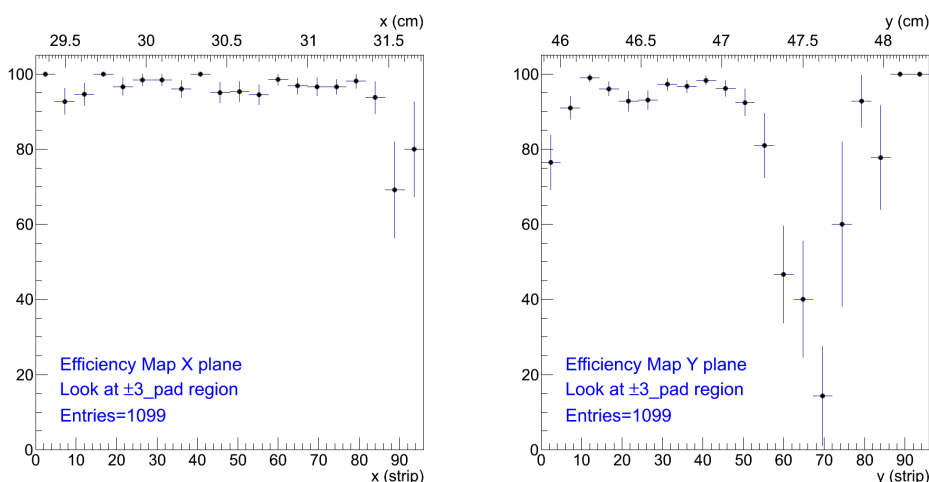

Figure 1.23: Χάρτης αποδοτικότητας για δεδομένα όπου η δέσμη είναι κεντραρισμένη σε μία νεκρή περιοχή.

1.7.8   Μελέτη απόκρισης σε δέσμες πιονίων

Κατά τη διάρκεια των πειραμάτων χρησιμοποιήθηκε μια δέσμη πιονίων 150 *GeV/c* για να μελετηθεί η απόκριση του μεγάλου ανιχνευτή στους αδρονικούς καταιγισμούς. Αυτό επιτεύχθη-
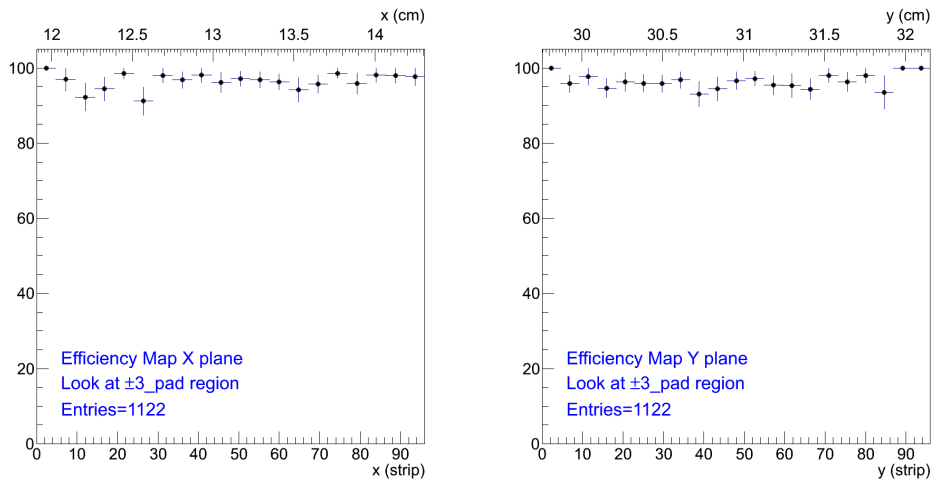
Figure 1.24: Χάρτης αποδοτικότητας για δεδομένα όπου η δέσμη είναι κεντραρισμένη σε μία ενεργή περιοχή.

κε με τη βοήθεια ενός τούβλου από σίδηρο το οποίο τοποθετήθηκε μπροστά από το πρωτότυπο. Γενικά, παρατηρήθηκε καλή απόκριση στους αδρονικούς καταιγισμούς υψηλής πολλαπλότητας, το οποίο ήταν και το ζητούμενο ενώ και σε αυτή την περίπτωση είναι δυνατό να δούμε την επίδραση των νεκρών περιοχών, όπως φαίνεται στο προφίλ της δέσμης σε μια ή περισσότερες διαστάσεις.
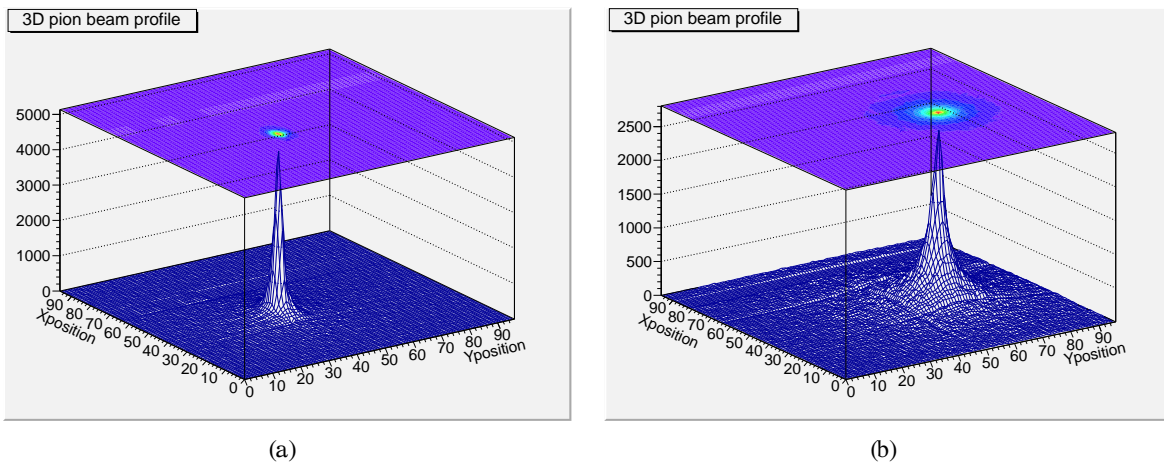
Figure 1.25: Τρισδιάστατο προφίλ της δέσμης των πιονίων με (a) ή χωρίς (b) την προσθήκη ενός τούβλου από σίδηρο.

Figure 1.26: Μονοδιάστατο προφίλ της δέσμης των πιονίων με την προσθήκη ενός τούβλου από σίδηρο για X (a) και Y (b) επίπεδο. Είναι εμφανής η επίδραση των νεκρών περιοχών του ανιχνευτή.

Figure 1.27: Πολλαπλότητα γεγονότων που παρατηρείται στον ανιχνευτή από αδρονικούς καταιγισμούς για διάφορες τάσεις στο mesh.
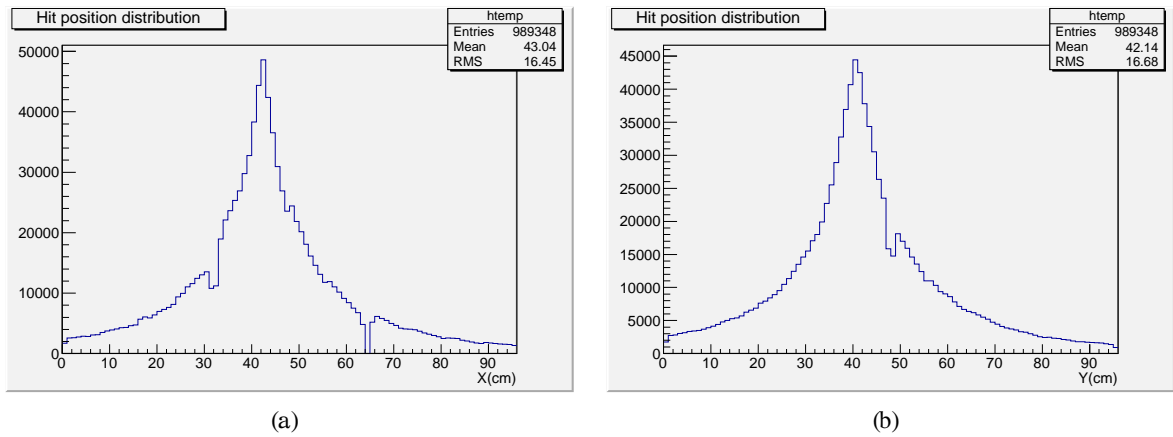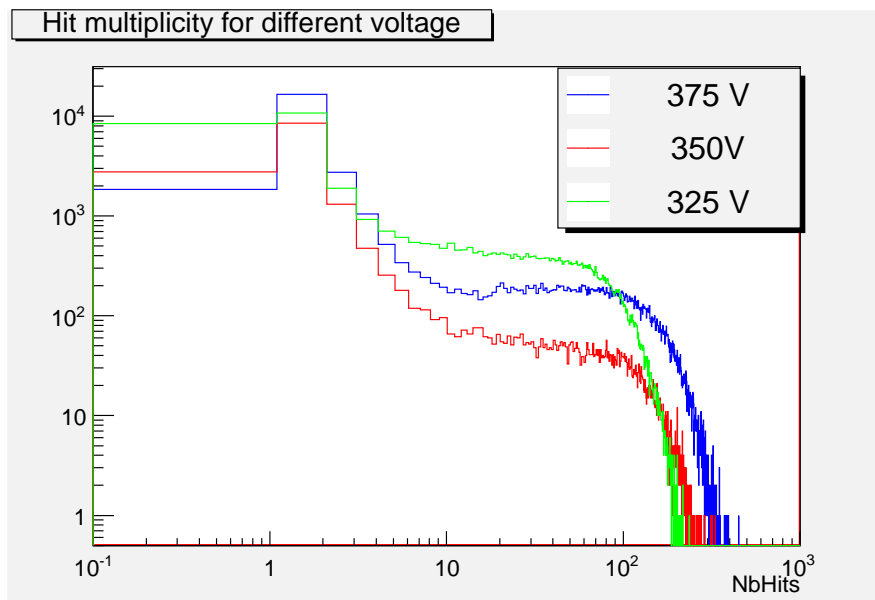
$$2$$

Introduction

2.1 Particle physics and Standard Model

Particle physics is the study of the fundamental constituents of matter and their interactions. However, which particles are regarded as fundamental has changed with time as physicists knowledge has improved. Modern theory, called the standard model, attempts to explain all the phenomena of particle physics in terms of the properties and interactions of a small number of particles of three distinct types: two spin-$\frac{1}{2}$ families of fermions called leptons and quarks, and one family of spin-1 bosons, called gauge bosons, which act as "force carriers" in the theory. In addition, at least one spin-0 particle, called the Higgs boson, is postulated to explain the origin of mass within the theory, since without it all the particles in the model are predicted to have zero mass. All the particles of the standard model are assumed to be elementary, i.e. they are treated as point particles, without internal structure or excited states.

The most familiar example of a lepton is the electron e^- (the superscript denotes the electric charge), which is bound in atoms by the electromagnetic interaction, one of the four fundamental forces of nature. A second well-known lepton is the electron neutrino v_e , which is a light, neutral particle observed in the decay products of some unstable nuclei (β-decays). The force responsible for the β-decay of nuclei is called the weak interaction.

Another class of particles called hadrons is also observed in nature. Familiar examples are the neutron n and proton p (collectively called nucleons) and the pions (π^+, π^-, π^0), where the superscripts again denote the electric charges. These are not elementary particles, but are made of quarks bound together by a third force of nature, the strong interaction. The theory predicts that the quarks themselves are not directly observable, only their bound states. The strong interaction between quarks gives rise to the observed strong interaction between hadrons, such as the nuclear force that binds nucleons into nuclei. There is an analogy here with the fundamental electromagnetic interaction between electrons and nuclei that also gives rise to the more complicated forces between their bound states, i.e. between atoms.

In addition to the strong, weak and electromagnetic interactions between quarks and leptons, there is a fourth force of nature, gravity. However, the gravitational interaction between elementary particles is so small that it can be neglected at presently accessible energies. Because of this, we will often refer in practice to the *three* forces of nature. The standard model also specifies the origin of these forces. Consider, firstly, the electromagnetic interaction. In classical physics this is propagated by electromagnetic waves, which are continuously emitted and absorbed. While this is an adequate description at long distances, at short distances

the quantum nature of the interaction must be taken into account. In quantum theory, the interaction is transmitted discontinuously by the exchange of spin-1 photons, which are the gauge bosons or "force carriers" of the electromagnetic interaction and the long-range nature of the force is related to the fact that photons have zero mass. The use of the word "gauge" refers to the fact that the electromagnetic interaction possesses a fundamental symmetry called *gauge invariance*. This property is common to all three interactions of nature and has profound consequences.

The weak and strong interactions are also associated with the exchange of spin-1 particles. For the weak interaction, they are called W and Z bosons, with masses about 80-90 times the mass of the proton. The resulting force is very short range, and in many applications may be approximated by an interaction at a point. The equivalent particles for the strong interaction are called gluons g. There are eight gluons, all of which have zero mass and are electrically neutral, like the photon. The strong interaction between the quark bound states (hadrons) is not the same as the fundamental strong interaction between quarks and has short range.
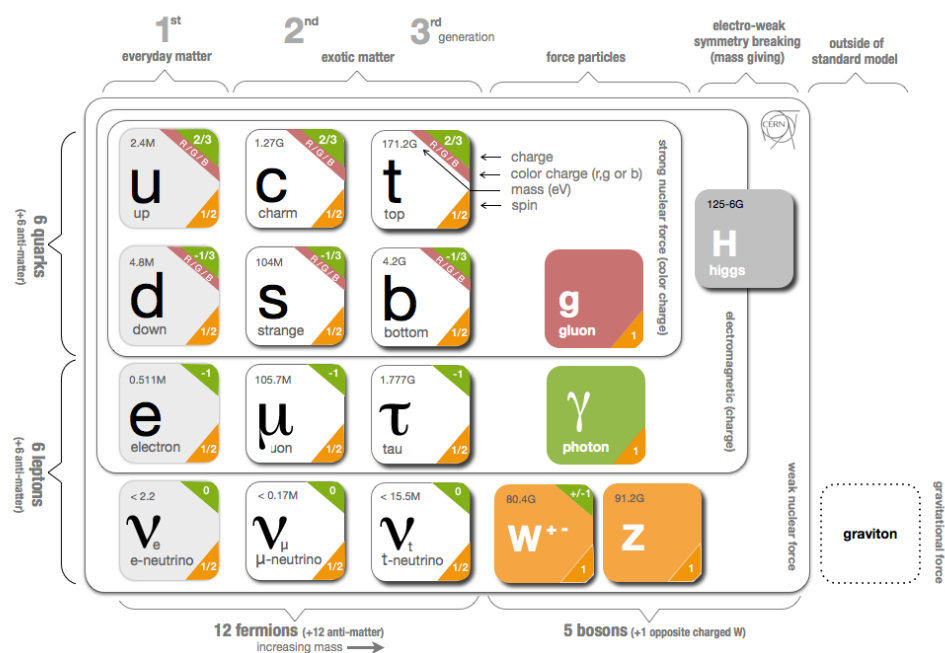
Figure 2.1: Elementary particles of Standard Model.

In particle physics, high energies are needed both to create new particles and to explore the structure of hadrons. The latter requires projectiles whose wavelengths λ are at least as small as hadron radii, which are of order $10^{-15}m$. It follows that their momenta, $p = \frac{h}{\lambda}$, and hence their energies, must be several hundred MeV/c (1 MeV = 10^6 eV). Because of this, any theory of elementary particles must combine the requirements of both special relativity and quantum theory.

2.2 Phycics at a Terascale $e^+ e^-$ linear collider

2.2.1 Questions about the universe

The central question of particle physics today is how the Standard Model has to be extended or can be succeeded by a theory that explains open questions and possible new phenomena of past, current and future experiments. The most prominent open question of the Standard Model is the existence of the Higgs boson which is responsible for the so called electroweak symmetry breaking and it is the gauge boson which generates massless photons and massive W and Z bosons as well as the masses of all elementary particles. Latest results presented by ATLAS and CMS collaborations at CERN's LHC indicate that the particle discovered is a Higgs boson. However, some time is needed in order to determine what kind of Higgs boson this particle is.

One of the problems of the Standard Model is its failure to explain Dark Matter. Only 5% of the mass of our universe consists of atoms, 23% is made of Dark Matter and 72% of Dark Energy. The Standard Model does not include any particle that could account for Dark Matter. However, models beyond the Standard Model, like super-symmetry models (SUSY), can provide an answer for Dark Matter. In SUSY models, all known elementary particles get super-partners, which have a spin that differs by 1/2 from that of their Standard Model partners. SUSY has to be a broken symmetry in order to separate the masses of the super-symmetric particles from the masses of the known elementary particles. The lightest super-symmetric particle in SUSY models can be constructed to be neutral and stable, and therefore would be a suitable candidate for Dark Matter.
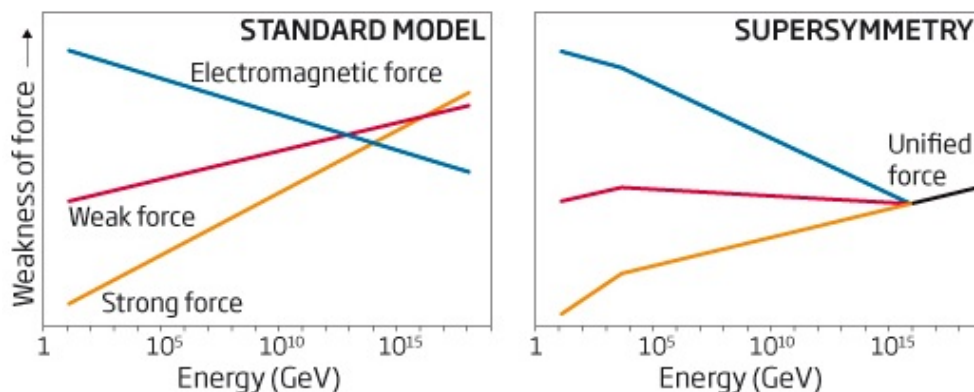

Figure 2.2: At high energies found in the early universe, the electromagnetic, weak and strong forces are all thought to have had the same strength, becoming a single force. In the standard model they fail to unite at a single energy, but do so with supersymmetry.

One major quest for our universe is to understand if fundamental forces originate from a single grand unified force, and search for evidence of a related unified origin of matter involving super-symmetry [Fig. 2.2]. They could distinguish among patterns of phenomena to judge different unification models, providing a telescopic view of the ultimate unification.

The Standard Model also does not explain the baryon asymmetry in our universe, since the size of CP-violation in weak interactions is not large enough. Ideas like electroweak baryogenesis in Minimal Super Symmetric Models or leptogenesis try to address this open question. Another indication for the existence of physics beyond the Standard Model is provided by neutrinos. The Standard Model predicts three types of neutrinos, which are massless in the model. This

assumption is valid in many cases so that precision calculations are not affected. However, since the discovery of neutrino oscillations, it is known that at least two of the three neutrino flavours have non-zero masses.

2.2.2 Future linear collider

During the past and next few years, experiments at CERN's Large Hadron Collider will have the first direct look at Terascale physics.The LHC, as a hadron collider, has a very large discovery potential,but it suffers from limited precision in certain areas of measurement because the exact energy of each collision is unknown. This is due to the composite aspect of the proton. The proton is not an elementary particle and as a result, its energy shared between its constituents and at high energy collisions occurs between constituents rather than entire protons. Therefore, only a small random fraction of the proton energy is involved in the hard collision. This leads to large uncertainty in the initial state of the collisions resulting in a limited precision of the measurements. On the other hand, the possibility of continuously browsing a wide scope of collision energies without modifying the machine settings gives a high discovery potential. Moreover, given the large mass of the proton (compared to electron), the synchrotron radiation is much lower and therefore much higher energies are possible. These are the major advantages of hadron colliders, sometimes dubbed as "discovery machines".

As electrons are elementary particles, the initial energy of an e^+e^- collision is well known. Limited discrepancies from nominal energy come from energy spread within particle bunches and electromagnetic radiation of the incoming particles before the collision. Nevertheless, the initial center of mass energy precisely peaks at the nominal value. Such a knowledge of the initial state opens to measurements impossible or very difficult at hadron colliders. Therefore, e^+e colliders are envisioned to succeed the LHC to obtain precise measurements on its discoveries and perhaps even more.

For electron colliders , the highest energy that has been reached was in the LEP tunnel (now LHC tunnel, 27km circumference) at about 200GeV. Above this value, the energy loss due to synchrotron radiation in a tunnel such as the LEP or LHC one, becomes too high and as a result a solution based on a larger ring in not considered. The only way to reach high energies, is to build a linear collider where the electrons will be accelerated at collision energy in only one passage.

Two projects are currently investigation, the International Linear Collider (ILC) and the Compact Linear Collider (CLIC). Each project is based on different acceleration technologies, each of which will reach different energies with a very different collision environment. The ILC with a design center-of-mass energy of $\sqrt{s} = 500$ GeV and a possible upgrade to 1 TeV and the Compact LInear Collider (CLIC) with $\sqrt{s} = 3$ TeV, which would be built in staged approach, starting around $\sqrt{s} = 500$ GeV. A CLIC machine at $\sqrt{s} = 500$ GeV is able to measure the same physics as the ILC.

However, if it is decided that the main answers to the present questions in particle physics can be answered with a machine at $\sqrt{s} < 1$ TeV, it is most likely that the ILC will be build, because it is based on well known and stable acceleration techniques. The main reason to built CLIC is the high energy option. At $\sqrt{s} = 3$ TeV, particle energies even higher than in present measurements at LHC can be studied.

2.2.3 International Linear Collider

The International Linear Collider (ILC) is an e^+e^- collider of the next generation. This machine and its experiments will operate at the forefront of science and provide novel and deep insight into the most fundamental aspects of nature, complementing and extending the capabilities of CERN's LHC.

It is planned that the machine will be initially operated at centre of mass energies ranging from $\sqrt{s}$ = 91 to 500 GeV, and up to 1 TeV in the second stage. This energy range combined with the clean initial state condition gives the possibility of a deeper investigation of the Standard Model (SM) as well as its possible extensions like Supersymmetry (SUSY) or extra dimensions. This physics program is complementary to the LHC's one. The LHC, due to its high centre of mass energy of 14 TeV, will be a powerful discovery machine to reveal the new physics which is expected on the TeV scale. The ILC will be better adapted to perform high precision tests like the determination of the Higgs properties. The layout of the accelerator is shown in figure [2.3].
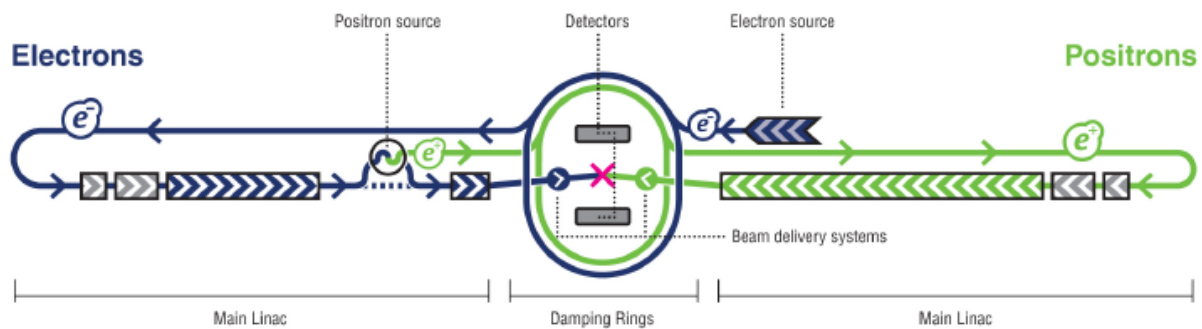

Figure 2.3: The layout of International Linear Collider (ILC).

Polarized electrons are produced by the illumination of photocathodes by two drive laser beams in a DC gun. The electron bunch train is created and accelerated over several stages before it is injected into the superconducting booster linac for the acceleration to 5 GeV. Afterwards, the electron beam travels through a 6.7 km long damping ring, whose main purpose is to reduce the beam emittance. Additionally, the beam is accelerated from 5 GeV to 15 GeV. The final acceleration to an energy of 250 GeV, over a distance of 12 km, is done in the main linac.

At an energy of 150 GeV, the electron beam is used to produce the positron beam in an undulator-based source, which is a periodic structure of dipole magnets. Electrons traversing this undulator are forced to undergo oscillations and thus, emit polarized photons of an energy of $\sim$ 10 MeV. The polarized photons are focused on a thin titanium foil to produce polarized positrons by pair production. Further positron acceleration happens analog to the electron acceleration in a second damping ring and main linac.

Before colliding with a crossing angle of 14 mrad, which is needed to reduce beam induced backgrounds at the interaction point, the beams are transported by a 4.5 km long beam delivering system from the main linac to the interaction point.

The key element of the accelerator are the two main linacs with their 1.3 GHz superconducting radio-frequency accelerating cavities, which are operated at a gradient of 31.5 MV/m. The total length of the accelerator is about 31 km. Physics runs are possible for every energy above $\sqrt{s}$ =

200 GeV and calibration runs with limited luminosity are possible at $\sqrt{s} = 91$ GeV. In order to perform mass and spin measurement via threshold scans, the beam energy can be changed in small steps. The electron beam should have a polarization higher than 80% and the positron beam should have an upgradable polarization of up to 50%

The design beam parameters would give approximately 2600 bunches per pulse with a length of ~ 1.6 ms at a pulse rate of 5.0 Hz. Design and technology of the ILC are advanced and ready to be built.

2.3 Calorimetry at a future linear collider

As mentioned in the previous sections, the detailed study of electroweak symmetry breaking and of the properties of a Higgs boson are some of the physics goals motivating the construction of a linear electron collider. The two candidate technologies are the 500 GeV (ILC) or the 3 TeV (CLIC). In both cases, however, several interesting physics channels will appear in multi-jet final states, often accompanied by charged leptons and missing transverse energy. The di-jet energy resolution should be such that Z and W masses can be determined with an accuracy comparable to the natural decay width of these bosons. This translates into a jet energy resolution of 3–4 % over the whole energy range.

Two kind of calorimeters are under study to meet this requirement. One proposes to measure and correct the fluctuations of the electromagnetic and hadronic components on a shower by shower basis. The second is based on the *Particle Flow* (*PF*) approach: the momentum of jet charged particles is measured with the tracking system, tracks and showers being matched thanks to a high segmentation of the calorimeters.

Several technological options are studied by the CALICE collaboration: silicon or scintillator for a sampling ECAL with tungsten absorbers, scintillator or gaseous chambers for the Fe or W HCAL. In the gaseous detector case, R&D on RPC, GEM and Micromegas are actively pursued. They are an attractive option with respect to the large area to be instrumented: $3000 \, m^2$ in the SiD detector concept. In addition, because there is only one sensor per layer (a gas layer), higher cell segmentation can be achieved than with scintillators (1 versus $9 \, cm^2$) with plausibly better *PF* performance. On the other hand, due to the large signal fluctuations in gaseous detectors, the charge information is of limited use. This may limit the single particle energy resolution necessary for measuring the neutral content of jets. As a result, gaseous hadronic calorimeters are essentially digital (1-2 bits per channel).

2.3.1 The Particle Flow approach to calorimetry

The concept of particle flow techniques is to consider the physics events in terms of reconstructed particles rather than signal in detectors and use the most suitable subdetector to measure a particle four-vector. As mentioned in table [2.1], different kinds of particles give specific signals in the different sub-detectors allowing them to be individually identified. In a particle flow algorithm, the electron energy is deduced from its momentum measurement in the tracker rather than from the direct energy measurement in the ECAL. The same stands for charged hadrons. Only neutral particle energies are measured in calorimeters.

A detector optimised for the application of particle flow techniques must be able to distinguish single particle signals in every sub-detector. This task is already well undertaken by trackers, which can easily distinguish separate particle tracks, provided they don't completely overlap.
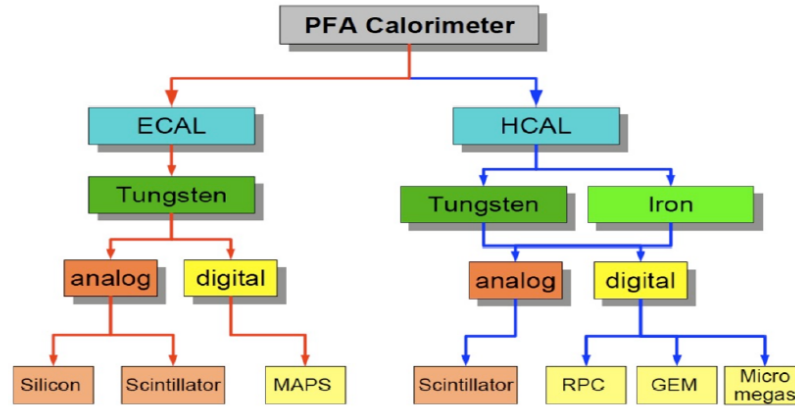
Figure 2.4: Overview of the various calorimeter technologies being pursued by the ILC/CLIC community

However, calorimeters are usually made out of large tiles representing a certain segmentation of the solid angle (e.g. segmentation of $\Delta\phi\Delta\eta = 0.1\times0.1$ in ATLAS HCAL) making single particle shower separation impossible. To allow single particle recognition, a particle flow optimised calorimeter must have an unprecedented lateral and longitudinal segmentation (3×3 cm^2 for the Analog Hadronic Calorimeter (AHCAL) project and 1×1 cm^2 for the Digital Hadronic Calorimeter (DHCAL) one), giving rise to the concept of "imaging calorimetry". This way, hit clusters in calorimeters can be isolated and matched with tracks from the tracker to reconstruct the entire signal from individual particles. Placing the magnet coil outside of the HCAL would be necessary to allow an efficient matching of reconstructed tracks with clusters and is therefore mandatory for a particle flow optimised detector.

**Table 2.1:** Specific signals of particle in subdetectors

Particle	Tracker	ECAL	HCAL	Muon Chamber
γ	–	El. shower	–	–
$e^{\pm}$	track	El. shower	–	–
$\mu^{\pm}$	track	track	track	track
$\pi^{\pm}$	track	track	Had. shower	-
$K^{\pm}$	track	track	Had. shower	–
K_L^0	–	–	Had. shower	–
$p,\overline{p}$	track	track	Had.shower	–
$n,\overline{n}$	–	–	Had.shower	–

The main successive steps of a particle flow algorithm are summarised as follows:

- Reconstruct the tracks.

- Regroup calorimeter hits in clusters.

- Match together clusters and tracks pointing to them to build the charged particles.

- Isolated clusters remaining must be taken as neutral particles.

- Charged particle energy is deduced from its precise momentum measurement and the deduction of its mass after the particle identification:

  ▶ Cluster mainly in ECAL: electron.

> ▶ Cluster mainly in HCAL: pion.

> ▶ Track across the whole detector: muon.

- Charged clusters are removed and the energy of neutral particles only is measured thanks to classical calorimetry.
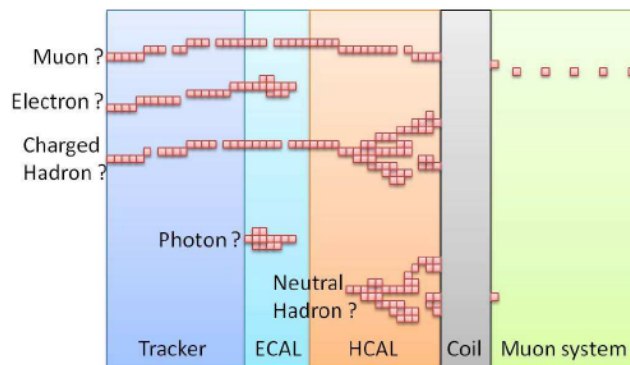
The next figure shows an illustration of particle's interaction in the various subdetectors at figure [2.5(a)], of the corresponding signal in classical detectors at figure [2.5(b)] and in a PFA optimised detector at figure [2.5(c)].
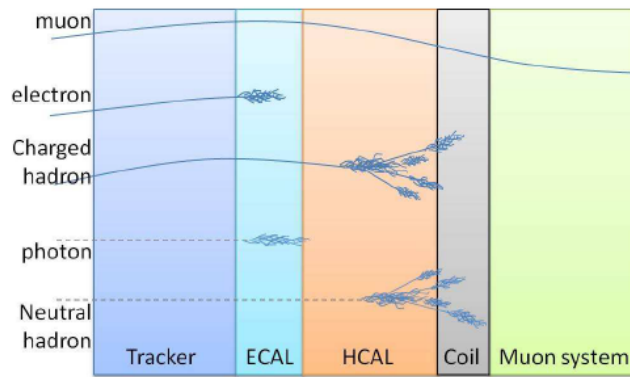
(a) Particle's interaction
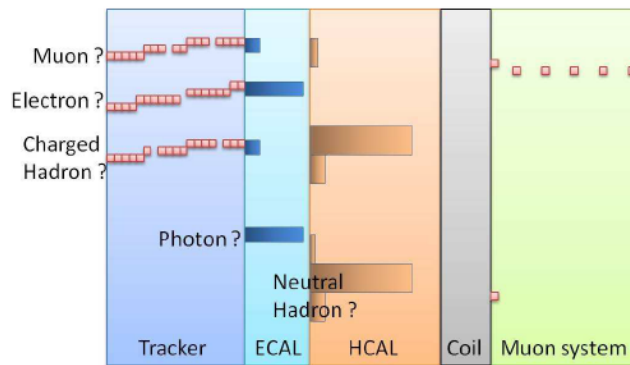
(b) Corresponding signal

(c) Particle flow detector

Figure 2.5: Illustration of particle's interaction in various subdetectors systems is shown in the top figure. While, the corresponding signal in a classical detector and in a PFA optimized detector is shown in middle and bottom figures respectively.

3

Interaction of particles and radiation with Matter

Particles and radiation can be detected only through their interactions with matter. There are specific interactions for charged particles which are different from those of neutral particles like photons. A heavy charged particle traversing matter loses energy primarily through the ionization and excitation of atoms. (Except at low velocities, a heavy charged particle loses a negligible amount of energy in nuclear collisions.) The moving charged particle exerts electromagnetic forces on atomic electrons and imparts energy to them. The energy transferred may be sufficient to knock an electron out of an atom and thus ionize it, or it may leave the atom in an excited, non-ionized state. A heavy charged particle can transfer only a small fraction of its energy in a single electronic collision. Its deflection in the collision is negligible. Thus, a heavy charged particle travels an almost straight path through matter, losing energy almost continuously in small amounts through collisions with atomic electrons, leaving ionized and excited atoms in its wake.

Electrons and positrons also lose energy almost continuously as they slow down in matter. However, they can lose a large fraction of their energy in a single collision with an atomic electron (having equal mass), thereby suffering relatively large deflections. Because of their small mass, electrons are frequently scattered through large angles by nuclei.
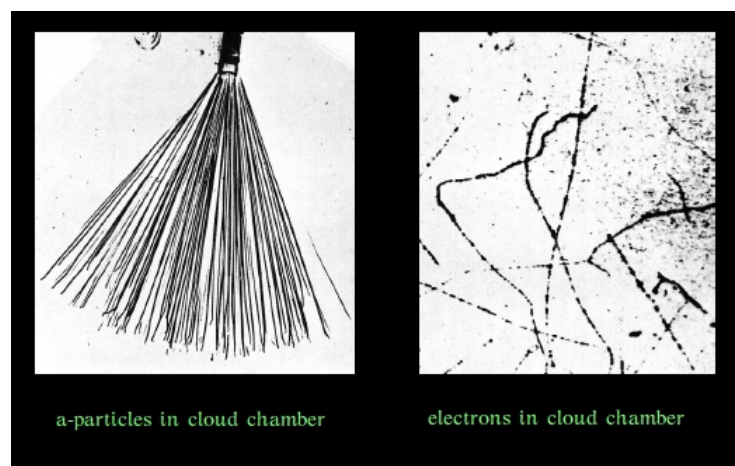

a-particles in cloud chamber   electrons in cloud chamber

Figure 3.1: Contrast between the straight tracks of alpha particles and electrons in cloud chamber.

In contrast to heavy charged particles, electrons and positrons do not generally travel through matter in straight lines. An electron can also be sharply deflected by an atomic nucleus, causing it to emit photons in the process called bremsstrahlung (braking radiation).

3.1   Interaction of heavy charged particles with matter

3.1.1   Maximum Energy Transfer in a Single Collision

In this section the maximum energy that a charged particle can lose in colliding with an atomic electron. We assume that the particle moves rapidly compared to the electron and that the energy transferred is large compared to the binding energy of the electron in the atom. Under these conditions the electron can be considered to be initially free and at rest, and the collision is elastic. We treat the problem classically and then give the relativistic results.

Figure 3.2 in (a) shows schematically a charged particle (mass M and velocity V) approaching an electron (mass m, at rest). After the collision, which for maximum energy transfer is head-on, the particles in (b) move with speeds V_1 and v_1 along the initial line of travel of the incident particle. Since the total kinetic energy and momentum are conserved in the collision, we have the two relations.

$$\frac{1}{2}MV^2 = \frac{1}{2}MV_1^2 + \frac{1}{2}mv_1^2 \tag{3.1}$$

and

$$MV = MV_1 + mv_1 \tag{3.2}$$

If we solve equation (3.2) for v_1 and substitute the result into equation (3.1), we obtain

$$V_1 = \left(\frac{M - m}{M + m}\right)V \tag{3.3}$$

Using this expression for V_1 , we find for the maximum energy transfer

$$Q_{max} = \frac{1}{2}MV^2 - \frac{1}{2}MV_1^2 = \frac{4mME}{(M + m)^2} \tag{3.4}$$

where $E = MV^2/2$ is the initial kinetic energy of the incident particle.
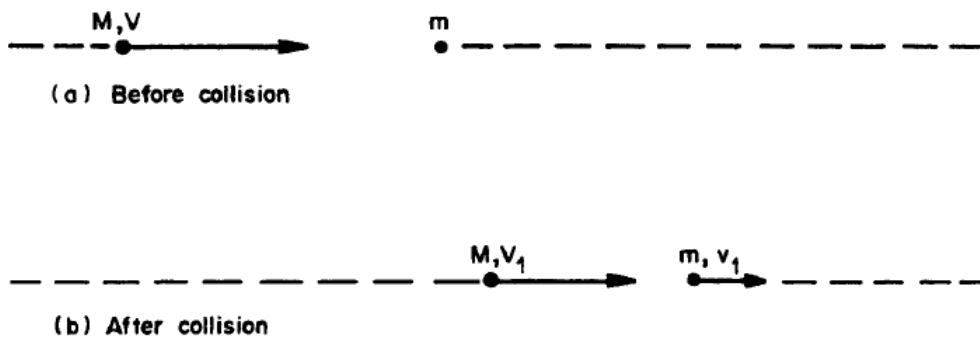

Figure 3.2: Representation of head-on collision of a particle of mass M and speed V with an electron of mass m, initially free and at rest.

Proton Kinetic Energy E(MeV)	Q_{max} (MeV)	Maximum Percentage Energy Transfer $100 Q_{max}/E$
0.1	0.00022	0.22
1	0.0022	0.22
10	0.0219	0.22
10^2	0.229	0.23
10^3	3.33	0.33
10^4	136.	1.4
10^5	$1.06 \cdot 10^4$	10.6
10^6	$5.38 \cdot 10^5$	53.8
10^7	$9.21 \cdot 10^6$	92.1

Table 3.1: Maximum Possible Energy Transfer, Q_{max}, in Proton Collision with Electron

When the incident particle is an electron or positron, the special circumstance arises in which its mass is the same as that of the struck particle: $M = m$. Equation (3.4) then implies that $Q_{max} = E$, and so its entire energy can be transferred in a single, billiard-ball-type collision. As already mentioned, electrons and positrons can thus experience relatively large energy losses and deflections, which contribute to their having tortuous paths in matter. The next particle more massive than the electron is the muon, having a mass $M = 207 \times m$) The maximum fraction of energy that a muon can transfer in a single collision is, from Equation (3.4),

$$\frac{Q_{max}}{E} = \frac{4m(207m)}{(208m)^2} \simeq \frac{4}{208} = 0.0192 \qquad (3.5)$$

Thus, the muon (and all heavy charged particles) travel essentially straight paths in matter, except for occasional large-angle deflections by atomic nuclei.

The exact relativistic expression for the maximum energy transfer, with m and M denoting the rest masses of the electron and the heavy particle, is

$$Q_{max} = \frac{2\gamma^2 m V^2}{1 + 2\gamma m/M + m^2/M^2} \qquad (3.6)$$

where $\gamma = 1/\sqrt{1-\beta^2}$, $\beta = V/c$, and c is the speed of light. Except at extreme relativistic energies, $\gamma m/M << 1$, in which case (3.6) reduces to

$$Q_{max} = 2\gamma^2 m V^2 = 2\gamma^2 m c^2 \beta^2 \qquad (3.7)$$

which is the usual relativistic result.

Table (3.1) gives numerical results for a range of proton energies. Except at extreme relativistic energies, where Equation (3.6) must be used, the maximum fractional energy loss for a heavy charged particle is small. At these extreme energies, the rest energy of the colliding particle contributes little to its total energy. The difference in rest mass between the proton and the struck electron then has little effect on the collision. One sees that Q_{max}/E approaches 100% in Table (3.1). Encounters in which an amount of energy comparable to Q_{max} is transferred are very rare, though, particularly at high energies.

Equations (3.4), (3.6), and (3.7) for maximum energy loss are kinematic in nature. That is, they follow from the simultaneous conservation of momentum and kinetic energy, independently of the kinds of forces that act. Under the conditions stated at the beginning of this section, it is a good approximation to calculate Q_{max} as though the struck electron were not bound, the collision then being elastic. Charged particle energy losses to atomic electrons are, in fact, inelastic; the stated conditions do not apply when a small amount of energy is transferred.

3.1.2 Stopping power at intermediate energies

The mean rate of energy loss by moderately relativistic charged heavy particles is described by the following equation which is called "Bethe-Bloch" formula:

(a) Muons   (b) Pions
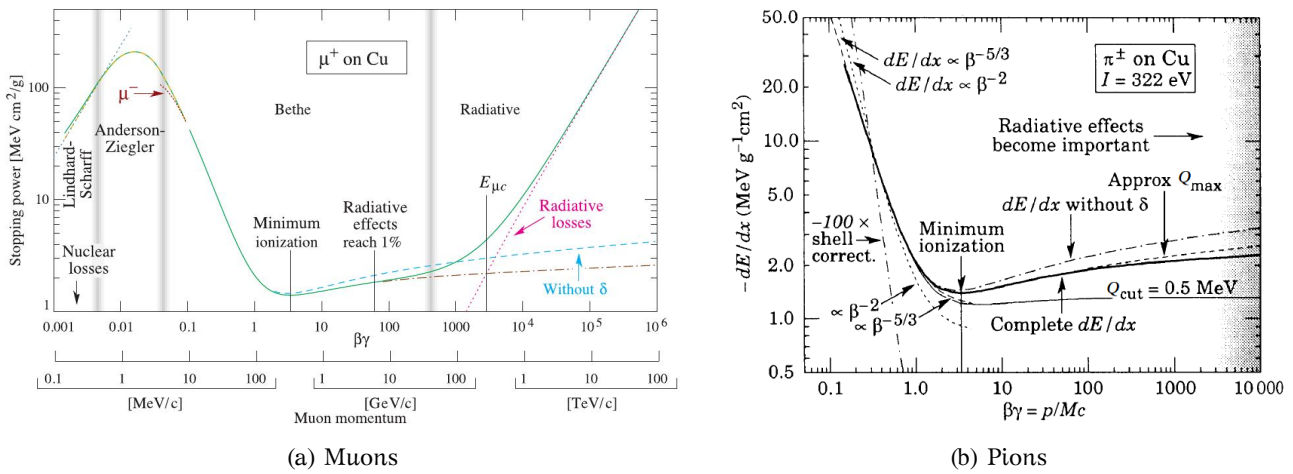
Figure 3.3: Stopping power for for muons ($\mu^{\pm}$) and pions ($\pi^{\pm}$) in copper as a function of $\beta\gamma$.

$$-\left(\frac{dE}{dx}\right) = Kz^2\frac{Z}{A}\frac{1}{\beta^2}\left[\frac{1}{2}\ln\frac{2m_ec^2\beta^2\gamma^2Q_{max}}{I^2} - \beta^2 - \frac{\delta(\beta\gamma)}{2} - \frac{C}{Z}\right] \qquad (3.8)$$

where,

m_ec^2	:	Electron mass $\times c^2$
r_e	:	Classical electron radius
ze	:	Charge of incident particle
N_A	:	Avogadro's number
Z	:	Atomic number of the absorber
A	:	Atomic mass of the absorber
K/A	:	$4\pi N_A r_e^2 m_e c^2/A$
I	:	Mean excitation energy of the medium
$\delta(\beta\gamma)$	:	Density effect correction to ionisation energy loss
C	:	Shell corretion

The Bethe-Bloch describes the mean rate of energy loss in the region $0.1 < \beta\gamma < 1000$ for intermediate-Z materials accurately. Q_{max} is the maximum energy transferred to a free electron in a single collision (see subsection 3.1.1). A minor dependence on the mass of the incident mass particle, at the highest energies, is introduced through Q_{max}, but for all practical purposes

dE/dx in a given material is a function of β alone. For heavy projectiles, like ions, additional terms are required to account for higher-order photon coupling to the target, and to account for the finite size of the target radius. These can change dE/dx by a factor of two or more for the heaviest nuclei in certain kinematic regimes.

The function as computed for muons on copper is shown as the "Bethe" region of figure (3.3(a)). Only in the Bethe region is it a function of β alone; the mass dependencies more complicated elsewhere. The stopping power in several other materials is shown in figure (3.5). Except in hydrogen, particles with the same velocity have similar rates of energy loss in different materials, although there is a slow decrease in the rate of energy loss with increasing Z. The qualitative behavior difference at high energies between a gas (He in the figure) and the other materials shown in the figure is due to the density-effect correction, $\delta(\beta\gamma)$. The stopping power functions are characterized by broad minima whose position drops from $\beta\gamma = 3.5$ to 3.0 as Z goes from 7 to 100.
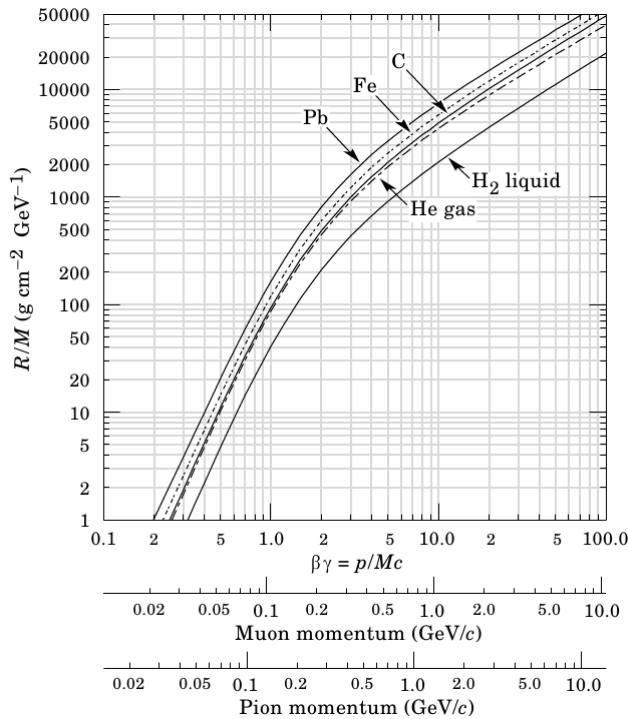
Figure 3.4: R/M as a function of $\beta\gamma = p/Mc$ for a variety of materials
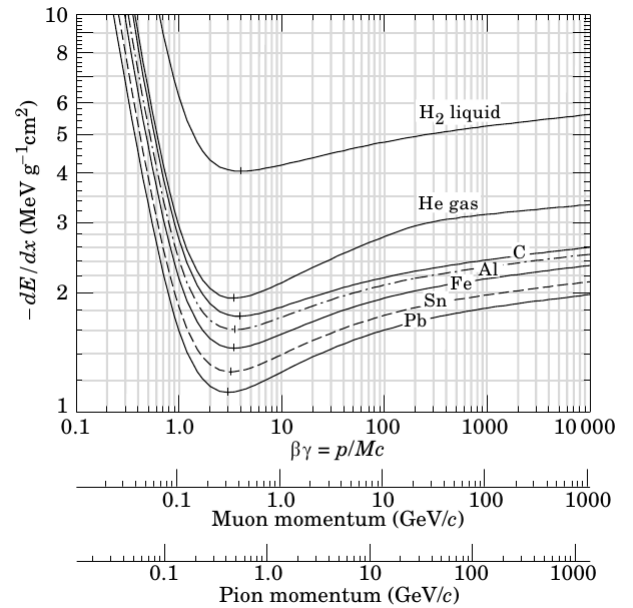
Figure 3.5: Mean energy loss rate in liquid (bubble chamber) hydrogen, gaseous helium, carbon, aluminum, iron, tin, and lead. Radiative effects, relevant for muons and pions, are not included. These become significant for muons in iron for $\beta\gamma > 1000$, and at lower momenta for muons in higher-Z absorbers.

In practical cases, most relativistic particles (e.g., cosmic-rays, muons) have mean energy loss rates close to the minimum; they are "minimum-ionizing particles," or MIPs. Knowing that particles lose energy when they pass through matter, the question is: how far they can travel, before they lose all of their energy? The quantity to describe this penetration is the so-called "range" and it depends on the type of the material, the particle type and its energy. If we assume that energy loss is continuous, for identical particles with the same initial energy in the same material, we expect the same range. But our nature is not identical, so when we have to calculate the range many particles of the same type, we have to deal with a statistical phenomenon. From a theoretical point of view, one can calculate the "mean range" of particles with a given energy E_0, by integrating the dE/dx formula:

$$Mean\ Range = R = \int_{E_0}^{0} \left(\frac{dE}{dx}\right)^{-1} dE \tag{3.9}$$

3.1.3   Energy loss at low energies

In the equation (3.8), the term that corresponds to the shell corrections must be included to correct for atomic binding having been neglected in calculating some of the contributions to equation (3.8). The C/Z term, accounts for the fact that, at low energies for light elements and at all energies for heavy ones, the probability of collision with the electrons of the inner atomic shells (K, L, etc.) is negligible. The semi-empirical formula used in calculations or simulations, applicable to all materials, is due to Barkas :

$$C(I, \beta\gamma) = \frac{a(I)}{(\beta\gamma)^2} + \frac{b(I)}{(\beta\gamma)^4} + \frac{c(I)}{(\beta\gamma)^6}. \tag{3.10}$$

where $a(I), b(I), c(I)$ some appropriate functions. This formula breaks down at low energies, and is valid only when $\beta\gamma > 0.13$ ($Q > 7.9$ MeV for a proton). For $\beta\gamma \leq 0.13$ the shell correction term is calculated as:

$$C(I, \beta\gamma)\bigg|_{\beta\gamma\leq 0.13} = C(I, \beta\gamma = 0.13)\frac{\ln(Q/Q_{2l})}{\ln(7.9\ \mathrm{MeV}/Q_{2l})} \tag{3.11}$$

i.e. the correction is switched off logarithmically from $Q = 7.9$ MeV to $Q = Q_{2l} = 2$ MeV.

3.1.4   Density effect

As the particle energy increases, its electric field flattens and extends, so that the distant-collision contribution to equation (3.8) increases as $\ln(\beta\gamma)$. However, real media become polarized, limiting the field extension and effectively truncating this part of the logarithmic rise. At very high energies,

$$\delta/2 \to \ln(\hbar\omega_p/I) + \ln(\beta\gamma) - 1/2. \tag{3.12}$$

where $\delta(\beta\gamma)/2$ is the density effect correction introduced in equation (3.8) and ω_p is the plasma energy. The density effect correction is usually computed using Sternheimer's parametrisation:

$$\delta(\beta\gamma) = \left\{ \begin{array}{ll} 2(\ln 10)x - \overline{C} & , if\ x \leq x_1 \\ 2(\ln 10)x - \overline{C} + a(x1 - x)^k & , if\ x_0 \leq x \leq x_1 \\ 0 & , if\ x < x_0\ (nonconductors) \\ \delta_0 10^{2(x-x_0)} & , if\ x < x_0\ (conductors) \end{array} \right\} \tag{3.13}$$

Here $x = log_{10}(\beta\gamma)$. $\overline{C}$ is obtained by equating the high-energy case of equation (3.13) with the limit given in equation (3.12). The other parameters are adjusted to give a best fit to the results of detailed calculations for several momenta.
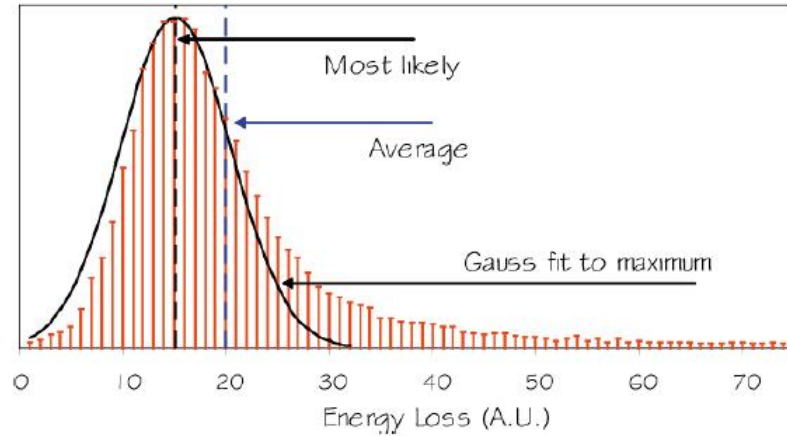
Figure 3.6: The Landau distribution

3.1.5 Fluctuations to energy loss

The Bethe-Bloch formula gives only the average energy loss of charged particles by ionisation and excitation. For thin absorbers, strong fluctuations around the energy loss exist. The energy-loss distribution for this absorbers is strongly asymmetric. This behaviour can be parametrized by the *Landau distribution*. The Landau distribution is described by the inverse Laplace transform of the function s^s. A reasonable approximation of the Landau distribution is given by:

$$L(\lambda) = \frac{1}{\sqrt{2\pi}} \cdot \left[-\frac{1}{2} \left(\lambda + e^{-\lambda} \right) \right] \tag{3.14}$$

where λ characterizes the deviation from the most probable energy loss,

$$\lambda = \frac{\Delta E - \Delta E^W}{\xi}, \tag{3.15}$$

ΔE :   actual energy loss in a layer of thickness x,
ΔE^W :   most probable energy loss in a layer og thickness x,

and

$$\xi = 2\pi N_A r_e^2 m_e c^2 z^2 \frac{Z}{A} \frac{1}{\beta^2} \rho x = k \rho x$$

where ρ is the density in g/cm^3 and x is the absorber thickness in *cm*.

The general formula for the most probable energy loss is

$$\Delta E^W = \xi \left[\ln \left(\frac{2m_e c^2 \gamma^2 \beta^2}{I} \right) + \ln \frac{\xi}{I} + 0.2 - \beta^2 - \delta(\beta\gamma) \right] \tag{3.16}$$

Experimentally, one finds that the actual energy-loss distribution is frequently broader than represented by the Landau distribution. For thick absorbers, the tail of the Landau distribution

originating from high energy transfers, however, is reduced. For very thick absorbers the energy-loss distribution can be approximated by a Gaussian distribution.

The energy loss dE/dx in a compound of various elements i is given by

$$\frac{dE}{dx} = \sum_i f_i \left[\frac{dE}{dx}\right]_i \tag{3.17}$$

where f_i is the mass fraction of the ith element and $(dE/dx)_i$, the average energy-loss in this element. Corrections to this relation because of the dependence of the ionisation constant on the molecular structure can be safely neglected.

The energy transfers to ionisation electrons ca be so large that these electrons can cause further ionisation. These electrons are called δ rays or knock-on electrons. The energy spectrum of knock-on electrons, for $I \ll Q \le Q_{max}$, is given by:

$$\frac{dN}{dQ} = \xi \cdot \frac{F}{Q^2} \tag{3.18}$$

F is a spin-dependent factor of order unity, if $Q \ll Q_{max}$. Of course, the energy spectrum of knock-on electrons falls to zero if the maximum transferable energy is reached. This kinematic limit also constraints the factor F. The spin dependence of the spectrum of the knock-on electrons only manifests itself close to the maximum transferable energy.

A δ ray with kinetic energy Q_e and corresponding momentum p_e is produced at an angle θ given by

$$\cos \theta = \left(\frac{Q_e}{p_e}\right)\left(\frac{p_{max}}{Q_{max}}\right) \tag{3.19}$$

where p_{max} is the momentum of an electron with the maximum possible energy transfer Q_{max}.

The strong fluctuations of the energy loss in thin absorber layers are quite frequently not observed by a detector. Detectors only measure the energy which is actually deposited in their sensitive volume, and this energy may not be the same as the energy lost by the particle. For example, the energy which is transferred to knock-on electrons may only be partially deposited in the detector because the knock-on electrons can leave the sensitive volume of the detector.

3.1.6 Restricted energy loss rates for relativistic ionizing particles

Further insight can be obtained by examining the mean energy deposit by an ionizing particle when energy transfers are restricted to $Q \le Q_{cut} \le Q_{max}$. The restricted energy loss rate is

$$-\left[\frac{dE}{dx}\right]_{Q<Q_{max}} = Kz^2\frac{Z}{A}\frac{1}{\beta^2}\left[\frac{1}{2}ln\frac{2m_e c^2 \beta^2 \gamma^2 Q_{cut}}{I^2} - \frac{\beta^2}{2}\left(1 + \frac{Q_{cut}}{Q_{max}}\right) - \frac{\delta(\beta\gamma)}{2}\right] \tag{3.20}$$

This form approaches the normal Bethe-Bloch formula as $Q_{cut} \to Q_{max}$. It can be verified that the difference between equation (3.8) and (3.20) is equal to

$$\int_{Q_{cut}}^{Q_{max}} Q\left(\frac{dN}{dQ}\right) dQ$$

where dN/dQ is given by equation (3.18)

Since Q_{cut} replaces Q_{max} in the argument of the logarithmic term of (3.8), the $\beta\gamma$ term producing the relativistic rise in the close-collision part of dE/dx is replaced by a constant, and (3.20) approaches the constant "Fermi plateau". The density effect correction δ eliminates the explicit $\beta\gamma$ dependence produced by the distant-collision contribution.

3.1.7 Multiple scattering through small angles

A charged particle transversing a medium is deflected by many small-angle scatters. Most of this deflection is due to Coulomb scattering from nuclei, and hence the effect is called multiple Coulomb scattering. (However, for hadronic projectiles, the strong interactions also contribute to multiple scattering.) The Coulomb scattering distribution is well represented by the theory of Moliere. It is roughly Gaussian for small deflection angles, but at larger angles (greater than a few θ_0 , defined below) it behaves like Rutherford scattering, with larger tails than does a Gaussian distribution. If we define

$$\theta_0 = \theta_{plane}^{rms} = \frac{1}{\sqrt{2}}\theta_{space}^{rms} \tag{3.21}$$

then it is sufficient for many applications to use a Gaussian approximation for the central 98% of the projected angular distribution, with a width given by

$$\theta_0 = \frac{13.6 MeV}{\beta cp} z \sqrt{\frac{x}{X_0}}\left[1 + 0.038\ln\left(\frac{x}{X_0}\right)\right] \tag{3.22}$$

Here p,βc and z are the momentum, velocity and charge of the incident particle, and x/X_0 is the thickness of the scattering medium in radiation lengths.

Equation (3.22) describes scattering from a single material, while the usual problem involves the multiple scattering of a particle traversing many different layers and mixtures. Since it is from a fit to a Moliere distribution, it is incorrect to add the individual θ_0 contributions in quadrature; the result is systematically too small. It is much more accurate to apply equation (3.22) once, after finding x and X_0 for the combined scatterer.
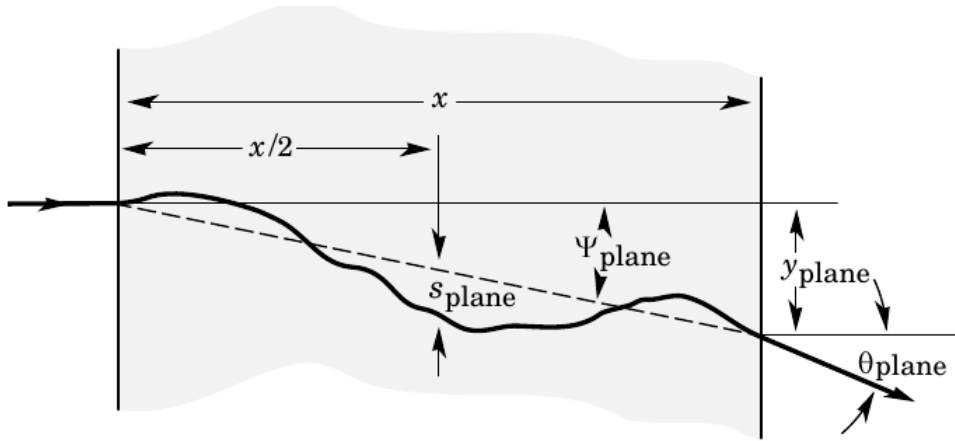
Figure 3.7: Quantities used to describe multiple Coulomb scattering. The particle is incident in the plane of the figure.

The non-projected(space) and projected(plane) angular distributions are given approximately by

$$\frac{1}{2\pi\theta_0} exp\left(-\frac{\theta_{space}^2}{2\theta_0^2}\right) d\Omega \tag{3.23}$$

$$\frac{1}{\sqrt{2\pi}\theta_0} exp\left(-\frac{\theta_{plane}^2}{2\theta_0^2}\right) d\theta_{plane} \tag{3.24}$$

where θ is the deflection angle. I this approximation, $\theta_{space}^2 \approx (\theta_{plane,x}^2 + \theta_{plane,y}^2)$, where the x and y axes are orthogonal to the direction of motion, and $d\Omega \approx d\theta_{plane,x} \cdot d\theta_{plane,y}$. Deflections into $\theta_{plane,x}$ and $\theta_{plane,y}$ are independent and identically distributed.

Figure (3.7) shows these and other quantities sometimes used to describe multiple Coulomb scattering. They are

$$\psi_{plane}^{rms} = \frac{1}{\sqrt{3}}\theta_{plane}^{rms} = \frac{1}{\sqrt{3}}\theta_0 \tag{3.25}$$

$$y_{plane}^{rms} = \frac{1}{\sqrt{3}}x\theta_{plane}^{rms} = x\frac{1}{\sqrt{3}}\theta_0 \tag{3.26}$$

$$s_{plane}^{rms} = \frac{1}{4\sqrt{3}}x\theta_{plane}^{rms} = \frac{1}{4\sqrt{3}}x\theta_0 \tag{3.27}$$

All the quantitative estimates in this apply only in the limit of small θ_{plane}^{rms} and in the absence of large-angle scatters. This random variables s, ψ, y and θ in a given plane are correlated. Obviously $y \approx x\psi$. In addition, y and θ have correlation coefficient $\rho_{y\theta} = \sqrt{3}/2 \approx 0.87$.

3.2   Interaction of electrons with matter

Electrons (e^-) and positrons (e^+) possess great similarity. As a result their interactions with matter slightly differ, mainly at their final destination. When a positron loses all its energy, i.e.

it tends to rest, likely it approaches an electron, resulting to the production of two photons with the same energy in opposite directions, due to the annihilation process. However, electrons due to the absence of positrons in matter, when they lose their energy, they become atomic electrons. Consequently, when we refer to the energy loss of electrons, we mean the mechanisms that both electrons and positrons lose their energy.

3.2.1 Energy loss by electrons e^-

Electrons, during their passage through matter, lose energy due to inelastic collisions with the atomic electrons and the nuclei. These interactions dominated by Coulomb force, cause ionisation and excitation processes and declination of the initial trajectory. The energy loss per unit length due to ionisation and excitation processes is given by the following equation:

$$\left(\frac{dE}{dx}\right)_{exc} = \frac{2\pi e^4 NZ}{m_e \upsilon^2}\left(\ln\frac{m_e c^2}{2I^2(1-\beta^2)} - \ln 2(2\sqrt{1-\beta^2}-1+\beta^2) + \frac{(1-\sqrt{1-\beta^2})^2}{8}\right) \quad (3.28)$$

It is obvious that energy loss depends on the inverse square of the velocity υ of the particle. If high energetic electrons cause an ionisation, then its possible that the ejected electrons have enough energy to cause further ionisation. Therefore, we can also have δ-rays produced from high energetic knock-on electrons.

During the inelastic collisions with the nuclei, electrons lose their energy due to braking radiation well-known as Bremsstrahlung radiation. Bremsstrahlung is electromagnetic radiation produced by the deceleration of a charged particle when deflected by another charged particle, typically an electron by an atomic nucleus. The moving particle loses kinetic energy, which is converted into a photon because energy is conserved. The term is also used to refer to the process of producing the radiation. The effect is larger for electrons due to their small mass compared to heavy charged particles where the effects is negligible.

Energy loss of electrons due to Bremsstahlung effect is given by the equation (3.29):

$$\left(\frac{dE}{dx}\right)_{rad} = \frac{e^4 NZ(Z+1)E}{137 m_e^2 c^4}\left(4\ln\frac{2E}{m_e c^2} - \frac{4}{3}\right) \quad (3.29)$$

The total energy loss of electrons per unit length is the sum of the energy loss due to ionisation and excitation and the energy loss due to Bremsstrahlung:

$$\left(\frac{dE}{dx}\right)_{total} = \left(\frac{dE}{dx}\right)_{exc} + \left(\frac{dE}{dx}\right)_{rad} \quad (3.30)$$

3.2.2 Correlation of energy loss due to excitation-ionisation and Bremsstrahlung

The energy loss per unit length of electrons due to excitation and ionisation depends on the inverse square of the velocity, for low energies. Therefore the lower the energy, the greater the loss. This dependence for the braking radiation is different. The energy loss increases with the increasing kinetic energy of the particles. Thus, for high energies, the energy loss due to the Bremsstrahlung is comparable to the loss due to excitation-ionisation.

A precise approximation for the ratio of these losses for velocities approaching the speed of light in vacuum is:

$$\frac{\left(\frac{dE}{dx}\right)_{exc}}{\left(\frac{dE}{dx}\right)_{rad}} = \frac{Z \cdot E(MeV)}{700} \tag{3.31}$$

where Z is the atomic number of the absorber.

The energy in which the energy loss due to ionization is equated to the energy loss due to braking radiation, called *Critical Energy* (see figure 3.8(a)) and depends mainly on the type of the material. Approximately the critical energy for solids and gases given by the following formulas, respectively:

$$E_{cr}^{solid} = \frac{610(MeV)}{Z + 1.24} \qquad , \qquad E_{cr}^{gas} = \frac{710(MeV)}{Z + 0.92} \tag{3.32}$$
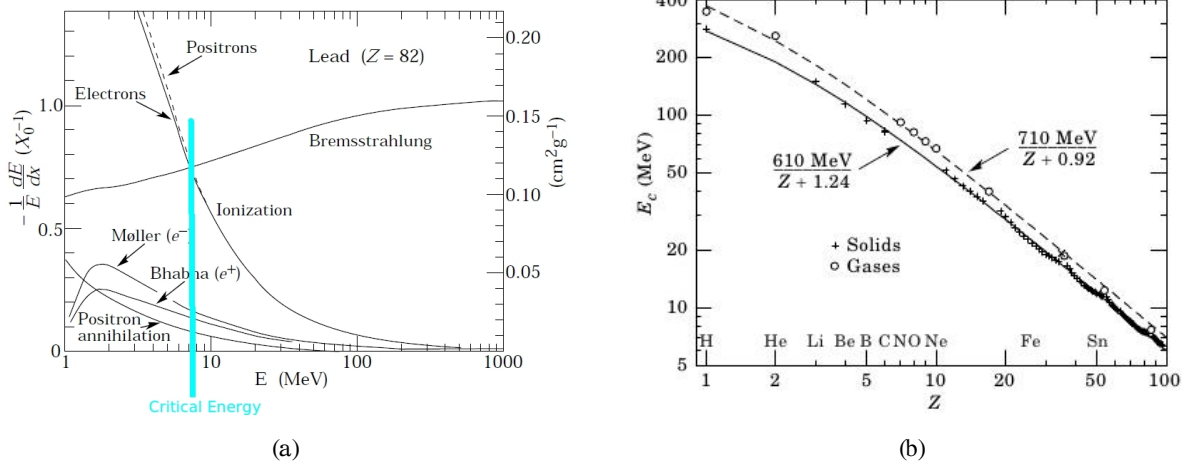
Figure 3.8: In (a) the critical energy for e^- and e^+ in lead (Pb) is shown, while, the dependence of critical energy on atomic number is shown in (b).

3.3   Interaction of photons with matter

Photons interact with matter mainly with tree mechanisms:

- Photoelectric effect.

- Compton Scattering.

- Pair production.

Each mechanism has a different dependence on the energy of the photons and the material of the absorber.

3.3.1 Photoelectric effect

The photoelectric effect (Fig. 3.9) is an interaction mechanism of photons which involves a photon with energy $E_\gamma = hf$ and one of the atomic electrons. The of the photon absorbed from the electron and as a result the electron ejected from the atom with kinetic energy:

$$E_{kin} = hf - \Phi_j \qquad (3.33)$$

where Φ_j is the binding energy of the electron for the atomic enrgy level j= K, L, M, ...
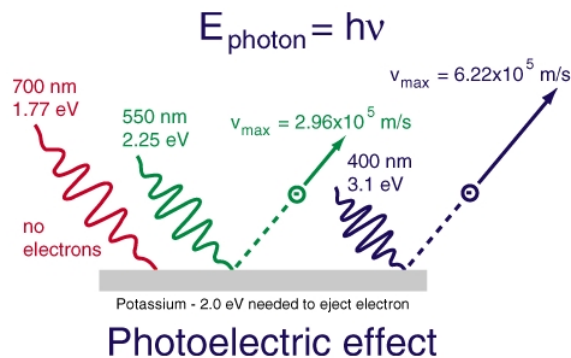
Figure 3.9: Photoelectric effect.

Consequently, it is obvious that the photoelectric effect happens if the photon energy is larger than the binding energy of the electron. Although, we expect the photoelectric to occur easily for large photon energies, this is not the case, because the larger the photon energy is compared to the binding energy of electrons, the lower the phenomenon's probability. Generally the photoelectric effect dominates at low energies.

The hole that created after the electron ejection covered by another electron came from a higher atomic shell with binding energy $\Phi_i < \Phi_j$, leading to two alternate mechanisms:
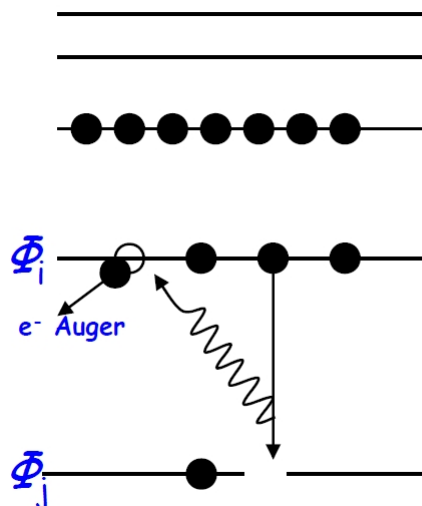
Figure 3.10: Auger effect

- **X-ray production**: production of secondary X-rays, with energy $\Phi_j - \Phi_i$ while the charge of the remaining ion does not change.

- **Auger effect**: the Auger effect (Fig. 3.10) is a physical phenomenon in which the filling of an inner-shell vacancy of an atom is accompanied by the emission of an electron from the same atom. When a core electron is removed, leaving a hole, an electron from a higher energy level may fall into the hole, resulting in a release of energy. Although sometimes this energy is released in the form of an emitted photon, the energy can also be transferred to another electron, which is ejected from the atom. This second ejected electron is called an Auger electron.

The new holes covered by electron transitions from higher shells until the ionized atom comes to a situation that new transition can not longer exist.

3.3.2   Compton Scattering

Compton scattering (Fig. 3.11) occurs for energies approaching the rest mass of electron and describes the scattering of a photon at an angle θ, by an atomic electron. The photon scattered at a different direction and a fraction of its energy transferred at the recoil electron which, after the scattering moving to a direction at an angle ϕ. The probability for the scattering to occur is independent of the atomic number of the material.
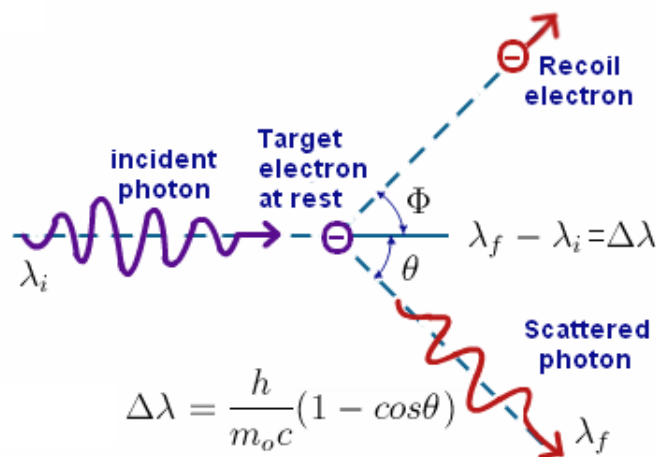
Figure 3.11: Compton scattering.

If someone apply the principles of energy and momentum conservation for the Compton scattering, leads to the following interesting conclusions:

- **Wavelength shift of scattered photon**

$$\Delta\lambda = \lambda' - \lambda = \frac{h}{m_e c} \cdot (1 - \cos\theta) \tag{3.34}$$

- **Energy of scattered photon**

$$E'_\gamma = hf' = \frac{E_\gamma}{1 + a(1 - \cos\theta)} \tag{3.35}$$

όπου

$$a = \frac{hf}{m_e c}$$

- **Kinetic energy of recoil electron**

$$E_{kin} = E_\gamma \cdot \frac{a(1 - \cos\theta)}{1 + a(1 - \cos\theta)} \tag{3.36}$$

If $\theta = 180^o$, then E_{kin} gets maximum and gives the Compton peak at the energy spectra. On the other hand, if $\theta = 0$, then E_{kin} get the minimum value. That fact lead to a continuous energy spectra and the Compton plateau.

- **Relation of θ and ϕ angles**

$$\cot\phi = \frac{(1 - \cos\theta) \cdot (1 + \alpha)}{\sin\theta} \tag{3.37}$$

The angular distribution of the scattered photons (3.12) gives us information for the differential cross section of the Compton effect. The Klein–Nishina formula (3.38) gives the differential cross section of photons scattered from a single free electron, derived in 1928 by Oskar Klein and Yoshio Nishina, and was one of the first results obtained from the study of quantum electrodynamics:

$$\left(\frac{d\sigma}{d\Omega}\right) = Zr_e^2\left(\frac{1}{1 + a(1 - \cos\theta)}\right)\left(\frac{1 + \cos^2\theta}{2}\right)\left(1 + \frac{a^2(1 - \cos\theta)^2}{(1 + \cos^2\theta)[1 + a(1 - \cos\theta)]}\right) \tag{3.38}$$

where

$$\alpha = \frac{E_\gamma}{m_e c^2}$$

and r_e is the classical electron radius.
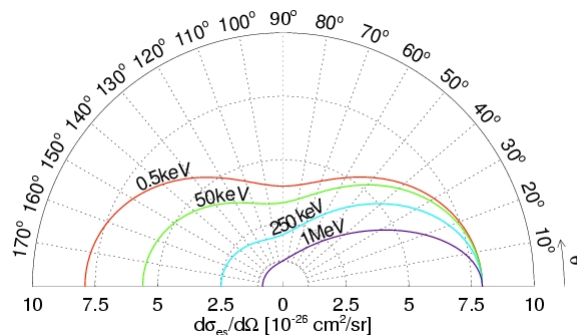
Figure 3.12: Angular distribution of the scattered photons

3.3.3 Pair production and annihilation

During the pair production effect (Fig. 3.13) we have a conversion of a photon into a pair of $e^+ - e^-$. The presence of the Coulomb field (near the nucleus) is mandatory and a minimum energy required ($E \geq 1.02 MeV$). The probability for of pair production effect, given by the pair production coefficient, depends on the energy of photon and the atomic number of the material.

After the pair production, the positron loses its energy and attracts an electron and annihilates into two photons each with energy $0.511 MeV$. At high energies, the positron loses its energy through ionisation and braking radiation processes until its energy is low enough for the annihilation to occur. Generally, the pair production effect occurs at high energies.
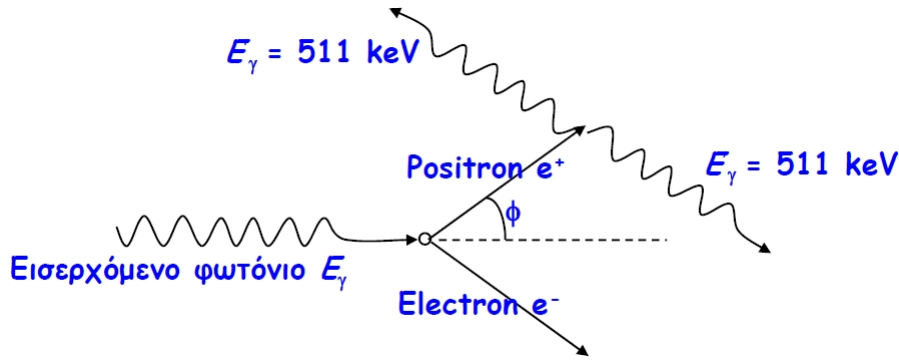
Figure 3.13: Pair production and annihilation

3.3.4 Energy loss by photons

For a photon beam which passes through matter, the attenuation is given by:

$$I = I_o \cdot e^{-\mu x} \tag{3.39}$$

where $\mu = N \cdot \sigma = \frac{1}{\lambda}$ is the mass attenuation coefficient of photons, I_o the incident intensity of the beam, σ the total cross section per atom, N the density of atom and λ is the mean free path, in the absorber material.

$$\lambda = \frac{\int_0^\infty x e^{-\mu x} dx}{\int_0^\infty e^{-\mu x} dx} \tag{3.40}$$

In order to study the cross section, we have to take into account that the interaction mechanism changes with the energy. Photoelectric effect occurs at low energies, while at intermediate energies the Compton effect dominates. At high energies, greater than 1.02 *MeV*, the effect that dominates is the pair production. When travelling through a material, photons are attenuated by all of the aforementioned processes, each one dominating at different energies. The measured cross-section is due to the combination of all three:

$$\sigma = \sigma_{photoelectric} + \sigma_{compton} + \sigma_{pair} \tag{3.41}$$

Figure [3.14(a)] shows an illustration of the relative importance of the three photon interaction as function of photon energy and the atomic number of the absorber. The solid lines correspond to equal interaction cross sections for the neighboring effects, while in figure [3.14(b)] is shown the measured cross section for iron due to the combination of all three mechanisms, versus the energy of photons.

3.4 Calorimetry

High energetic particles interact with matter and loose their energy. The initial energy E of the primary particle is converted into a cascade of particles, well-known as particle shower. In these iterative interactions with matter the primary energy is shared over more particles until their energy is too low to generate additional ones. After passing this limit the particles are slowed down by elastic interactions until they are stopped and the shower extinguishes.
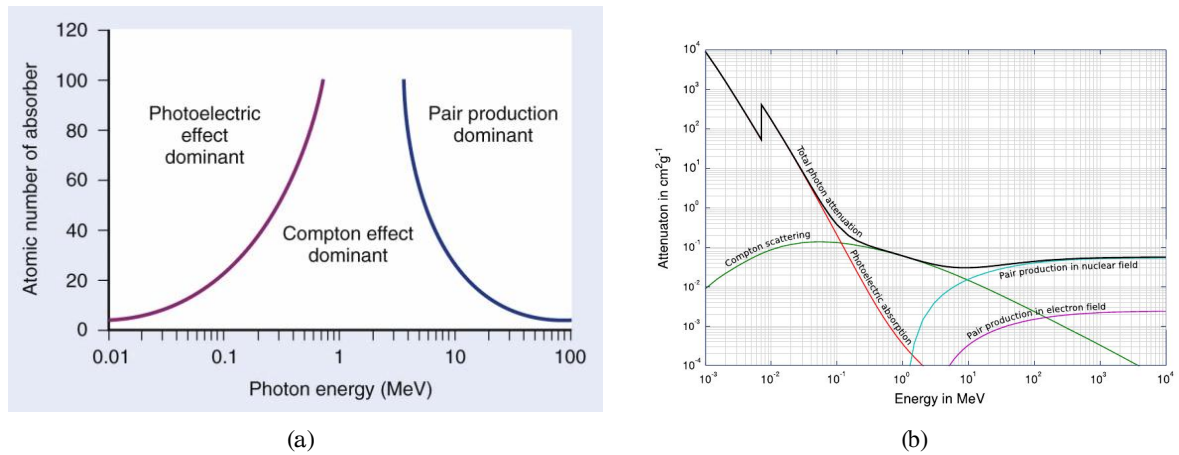
Figure 3.14: (a) Illustration of the relative importance of the three photon interaction mechanisms as function of photon energy and the atomic number of the absorber. (b) Measured cross section for iron due to the combination of all three mechanisms, versus the energy of photons.

Showers can be classified into two main types: electromagnetic and hadronic showers. Leptons do not undergo strong interactions, therefore, they can only contribute to electromagnetic showers. Hadrons having mass heavier in comparison to electrons and positrons are not initiating radiation processes, though characterizing the second type of shower.

Calorimetry for high energy physics is using shower cascades to measure the initial energy of particles. Although the name calorimetry refers to temperature measurements, the energies we are trying to measure, generate in matter only temperature changes in the order of 10^{-8} K. Therefore, calorimeters exploit other processes to measure the energy of a particle, like light generation or ionisation effects of these particles. Calorimeters are instrumented blocks of matter in which the particle to be measured interacts and deposits all its energy in the form of a cascade of particles whose energy decreases progressively down to the threshold of ionisation and excitations that are detectable by the readout media. The deposited energy is detectable in the form of a signal which is roughly proportional to the incoming energy. This proportionality is the base of calorimetric measurements.

Electromagnetic calorimeters are used to measure the energy deposited by electromagnetically interacting particles (electrons, positrons, photons) while the hadron (i.e. pion, kaon, proton) energy measurement is mainly performed by hadron calorimeters. Furthermore, calorimeters are classified into two types: homogeneous calorimeters, in which the incoming particle energy is measured in a homogeneous block of sensitive absorbing material; and sampling calorimeters, in which the incoming particle energy is measured in a number of sensitive layers interspersed with the layers of absorbing material, the later enabling a fast cascade process.

The total depth of the calorimeter must be large enough to allow a longitudinal containment of the shower in order to completely absorb the incoming energy. The necessary longitudinal depth of a calorimeter varies with the incoming energy, E, as $\ln E$ and therefore the calorimeter can remain a compact construction even at the high energies. The incoming energy being distributed among a large number of secondary particles, can be deposited at large angles with respect to the longitudinal axis of the initial particle trajectory. The result is that the transverse containment of the shower imposes a minimal radial extension of the calorimeter which has to reach at least several times the average radius of a shower. Therefore, the calorimeter dimensions must be large enough to avoid longitudinal and lateral leakage of showers. The granularity is another important requirement for a calorimeter and characterises the spatial

separation between readout cells. The granularity is imposed by physics and is fixed in practise by the minimum angle between particles to be detected. In order to separate adjacent showers in a dense jet environment care should be taken in the choice of the transverse calorimeter cell size. In addition, the detailed measurement of the shower position during its development in the calorimeter volume also demands the best possible longitudinal granularity and, therefore, requires a longitudinal segmentation of the calorimeter readout.

Calorimeters must have an energy resolution compatible with the experimental goals. In the case of hadron calorimeters, this possibility is mostly dictated by their relative response to the electromagnetic (e) and hadronic (π) shower, measured by the e/π signal ratio. The equalisation between the electromagnetic and hadronic signals ($e/\pi = 1$, i.e. the compensation condition) is the condition for obtaining the linearity of the energy response of the calorimeter to incoming hadronic showers, and to achieve an energy resolution that improves as the incident energy increases.

The physics conditions met in the experimental zone by a test calorimeter differ from those encountered in an operating beam collision experiment. For instance, the energy resolution of a test calorimeter is assessed from the measurement, in its volume, of the energy deposition from particles of well known dedicated beams, while a calorimeter operating in a physics experiment will face particles produced in collisions. The energy of these particles will cover a large range and many will be produced with relatively low energy, leading to a degradation of the calorimeter energy resolution. The calorimeter performance is also affected by the amount of material in front and by beam conditions, such as the momentum spread of the beam and its degradation due to detectors in front of the calorimeter, and by the precision of beam counters.

3.4.1 Electromagnetic showers

High energetic electrons, positrons and photons, above their critical energy, generate an electromagnetic cascade due to the production of secondary particles, via multiple successive bremsstrahlung and pair production processes in an absorber. The number of produced particles is roughly proportional to the incident particle energy. The electromagnetic shower development in an absorber material depends on the radiation length X_0. The radiation length depends on the atomic number and the atomic mass of the absorber material, shown in equation 3.42, and denotes the distance after which the incident particle with energy E_0, lose a fraction E_0/e of its energy due to bremsstrahlung.

$$X_0 \left(\frac{g}{cm^2} \right) = \frac{716.4 g \cdot cm^{-2} A}{Z \cdot (Z+1) \cdot \ln \frac{287}{\sqrt{Z}}} \tag{3.42}$$

Since the longitudinal shower development is primarily driven by the high energy part of the electromagnetic cascade, the electromagnetic shower length scales with the radiation length of the absorber material.

Consider a simplified model of development of an electromagnetic shower initiated by an electron or a photon of energy E. A universal description, independent of material, can be obtained if the development is described in terms of scaled variables:

$$t = \frac{x}{X_0} \quad \text{and} \quad y = \frac{E}{\epsilon}$$
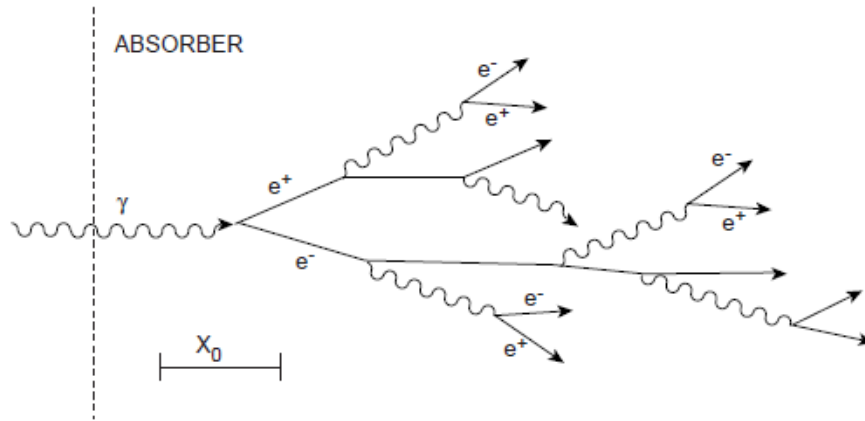
Figure 3.15: Schematic development of an electromagnetic shower.

Since, in one X_0 an electron loses about 2/3 of its energy and a high energy photon has a probability of 7/9 of pair conversion, we can naively take one X_0 as a generation length. In each generation the number of particles increases by a factor of 2. After t generations the energy and number of particles, respectively is :

$$e(t) = \frac{E}{2^t} \quad \text{and} \quad n(t) = 2^t$$

At the shower maximum, where $e \approx \epsilon$, the number of particles is:

$$n(t_{max}) = \frac{E}{\epsilon} = y \quad \text{and} \quad t_{max} = \ln \frac{E}{\epsilon} = \ln y$$

Critical energy electrons do not travel far ($\leq 1X_0$). After the shower maximum the remaining energy of the cascade is carried forward by photons giving the typical exponential falloff of energy deposition caused by the attenuation of photons. Longitudinal development of 10 GeV showers in Al, Fe and Pb is shown in figure 3.16(a). It can be noted that the shower maximum is deeper for higher Z materials because multiplication continues down to lower energies. The slower decay beyond the maximum is due to the lower energies at which electrons can still radiate. Both of the above effects are due to lower e for higher Z materials.

The mean longitudinal profile of energy deposition is given by:

$$\frac{dE}{dt} = Eb\frac{(bt)^{a-1}e^{-bt}}{\Gamma(a)} \tag{3.43}$$

The maximum of the shower occurs at $t_{max} = (a-1)/b$. Fits to t_{max} give

- $t_{max} = \ln y - 0.5$ for electron-induced cascades.
- $t_{max} = \ln y + 0.5$ for photon-induced cascades.

The coefficient a can be found using t_{max} and assuming $b \approx 0.5$. The photon induced showers are longer since the energy deposition only starts after the first pair conversion has taken place. The mean free path length for pair conversion of a high energy photon is $X_\gamma = (9/7)X_0$.

The lateral spread of an e.m. shower is determined by multiple scattering of electrons away from the shower axis. Also responsible are low energy photons which deposit their energy a

(a) Longitudinal development of 10 *GeV* electron showers in Al, Fe and Pb.

(b) Lateral profile of energy deposition by 50 *GeV* electrons showers in $PbWO_4$ at various depths
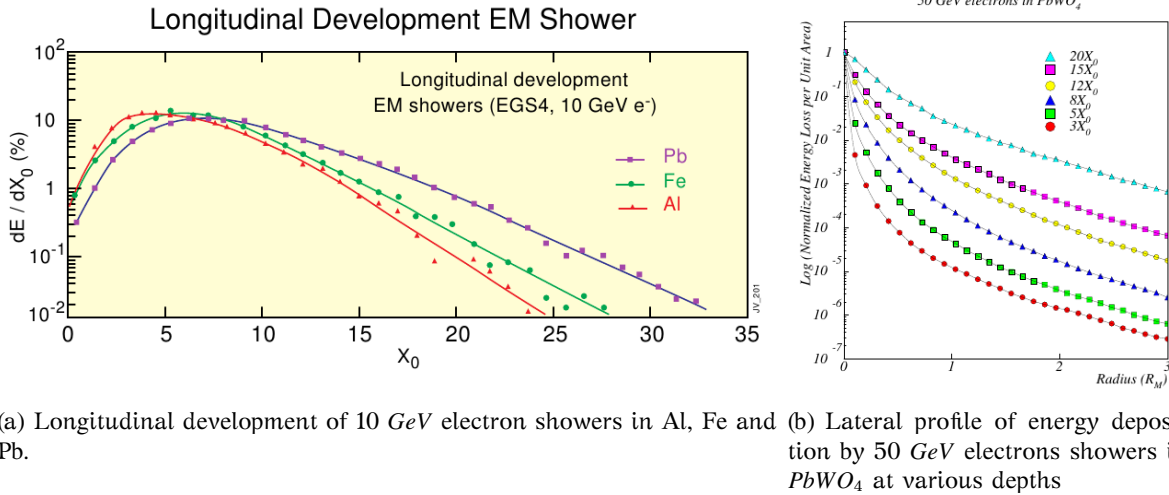
Figure 3.16: Longitudinal and lateral development of electromagnetic shower.

long way away from their point of emission, especially when emitted from electrons that already travel at large angles with respect to the shower axis. The e.m. shower begins, and persists, with a narrow core of high energy cascade particles, surrounded by a halo of soft particles which scatter increasingly as the shower depth increases. This is shown in figure 3.16(b) for 50 *GeV* electrons incident on lead tungstate.

In different materials the lateral extent of e.m. showers scales fairly accurately with the Moliére radius.The Moliére radius gives the average lateral deflection of critical energy electrons after traversal of 1 X_0 and is parameterized as:

$$R_M = \frac{21_{MeV}X_0}{\epsilon} \quad \oplus \quad \frac{7A}{Z} \quad g \cdot cm^{-2} \tag{3.44}$$

An infinite cylinder with a radius of ≈ 1 R_M contains $\approx 90\%$ of the shower energy. The fact that e.m. showers are very narrow at the start can be used to distinguish single photons from π^0.

3.4.2 Hadronic showers

A situation analogous to that for electromagnetic showers exists for hadronic showers. The interaction responsible for shower development is the strong interaction rather than electromagnetic. The interaction of the incoming hadron with absorber nuclei leads to multi-particle production. The secondary hadrons in turn interact with further nuclei leading to a growth in the number of particles in the cascade. Nuclei may breakup leading to spallation products. The cascade contains two distinct components namely the electromagnetic one (π^0 etc.) and the hadronic one ($\pi^\pm$, n, etc.) one. This is illustrated in figure 3.17.

The multiplication continues until pion production threshold is reached. The average number n, of secondary hadrons produced in nuclear interactions is given by n a $\ln E$ and grows logarithmically. The secondaries are produced with a limited transverse momentum of the order of 300 *MeV*.

It is convenient to describe the average hadronic shower development using scaled variables
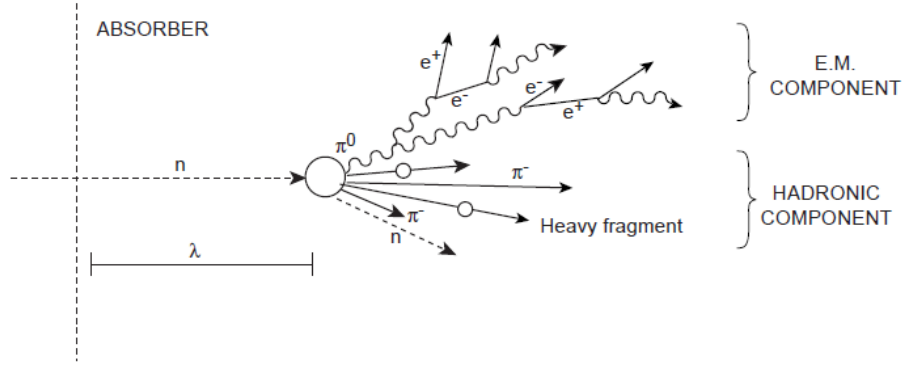
Figure 3.17: Schematic of development of a hadronic shower.

$$v = x/\lambda \quad \text{and} \quad E_{th} \approx 2m_\pi = 0.28 GeV$$

where λ is the interaction length and is the scale appropriate for longitudinal and lateral development if hadronic showers. The generation length can be taken to be λ. Note that, $\lambda \oplus 35A^{1/3}g \cdot cm^{-2}$. Furthermore, if it is assumed that $\langle n \rangle$ secondaries/primary are produced for each generation and that the cascade continues until no more pions can be produced. Then in generation v

$$e(v) = \frac{E}{\langle n \rangle^v}$$

$$e(v_{max}) = E_{th} \quad \therefore \quad E_{th} = \frac{E}{\langle n \rangle^{v_{max}}}$$

$$n^{v_{max}} = \frac{E}{E_{th}} \quad \Rightarrow \quad v_{max} = \frac{\ln(E/E_{th})}{\ln \langle n \rangle}$$

The number of independent particles in the hadronic cascades compared to electromagnetic ones is smaller by E_{th}/ϵ and hence the intrinsic energy resolution will be worse at least by a factor $\sqrt{E_{th}/\epsilon} = 6$. The average longitudinal energy deposition profiles are characterised by a sharp peak near the first interaction point (from π_0) followed by a exponential fall-off with scale λ. This illustrated in figure **??**. The maximum occurs at $t_{max} \oplus 0.2 \cdot \ln E + 0.7$ (E in GeV).

A parametrisation for the depth required for almost full containment (95%) is given by $L_{0.95}(\lambda) \approx t_{max} + 2\lambda_{att}$ where $\lambda_{att} \oplus \lambda E^{0.13}$. Figure 3.18(a) shows that over 9λ are required to contain almost all the energy of high energy hadrons. However there is a considerable variation from one hadronic shower to another. The peaks arise from energy deposited locally by π^0 produced in the interactions of charged hadrons. These interactions take place at differing depths from shower to shower. The energy carried by π^O's also varies considerably from shower to shower.

The secondary hadrons are produced typically with $\langle p_t \rangle \approx 300 MeV$. This is comparable to the energy lost in 1λ in most materials. At shower maximum, where the mean energy of the particles is $E_{th} \approx 280\,MeV$, the radial extent will have a characteristic scale of $R_\pi \approx l$. High energy hadronic showers show a pronounced core, caused by the π_0 component with a characteristic transverse scale of R_M, surrounded by an exponentially decreasing halo with scale λ. This is illustrated in figure 3.18(b) for a lead/scintillating fibre calorimeter.
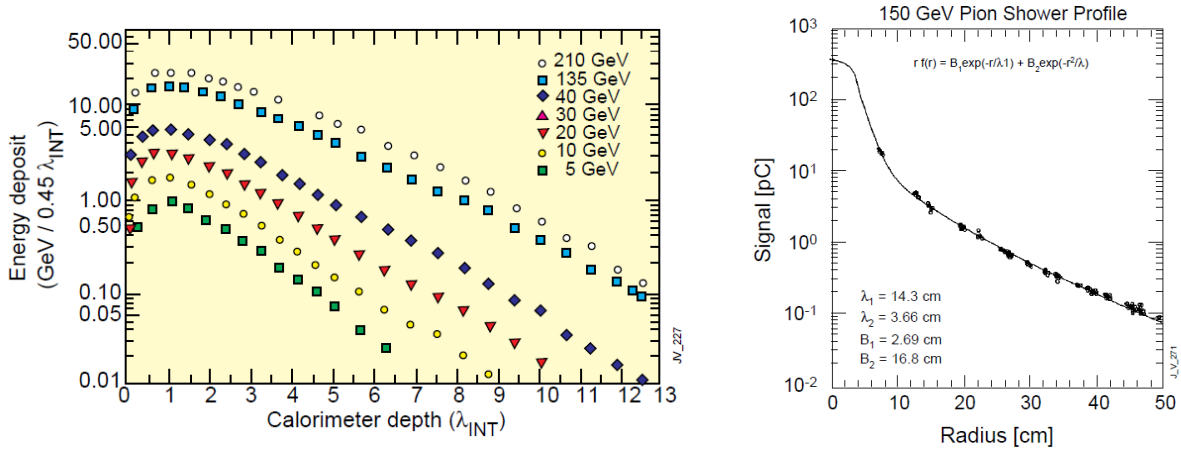
(a) Longitudinal profile of energy deposition for pion showers of different energies.

(b) The lateral profile of energy deposition for pion showers.

Figure 3.18: Longitudinal and lateral profile of energy deposition for pion showers

3.4.3 Energy resolution

The energy resolution of calorimeters is usually parametrised as shown in the next equation:

$$\frac{\sigma}{E} = \frac{a}{\sqrt{E}} \oplus \frac{b}{E} \oplus c \qquad (3.45)$$

where the right hand side is square root of the quadratic sum of the three terms.

The first term, with coefficient a, is the stochastic or sampling term and accounts for the statistical fluctuation in the number of primary and independent signal generating processes, or any further process that limits this number. An example of the latter is the conversion of light into photoelectrons by a photo-device.

The second term, with coefficient b, is the noise term and includes:

- the energy equivalent of the electronics noise and

- the fluctuation in energy carried by particles, other than the one(s) of interest, entering the measurement area. This is usually labelled pileup.

The last term, with coefficient c, is the constant term and accounts for:

- imperfect quality of construction of the calorimeter

- non-uniformity of signal generation and/or collection

- cell-to-cell inter-calibration error

- the fluctuation in the amount of energy leakage from the front or the rear (though somewhat increasing with energy) the volume used for the measurement of energy

- the contribution from the fluctuation in the electromagnetic component in hadronic showers

The tolerable size of the three terms depends on the energy range involved in the experiment. The above parametrisation allows the identification of the causes of resolution degradation.

The quadratic summation implies that the three types of contributions are independent which may not always be the case.

3.4.4 Sampling calorimeters

Calorimeters are designed to measure the energy of an electromagnetic or a hadronic shower by its complete absorption and sometimes measure also the shape and direction of the shower. Two types of calorimeters exist, namely homogeneous calorimeters and sampling calorimeters.

Homogeneous calorimeters are made out of active material only, which has the advantage that all measurable energy can be detected, in principle. In order to achieve a complete energy loss of the incoming particle, calorimeters have to have a high density. Table (3.2) shows physical properties of some materials used in calorimeters. For electromagnetic calorimeters, which typically have to have a total radiation length of $30 X_0$, the choice of a high density material can be suitable. Instead, for a hadronic calorimeter, its interaction length is usually too high to construct a calorimeter with an affordable depth. Typically, a total interaction length of $5 - 8\,\lambda$ is needed in high energy particle physics.

Table 3.2: Physical properties of some materials used in calorimeters.

Material	Z	ρ $[g \cdot cm^{-2}]$	I/Z $[eV]$	ϵ $[MeV]$	X_0 $[cm]$	λ_{int} $[cm]$
C	6	2.2	12.3	103	≈ 19	38.1
Al	13	2.7	12.3	47	8.9	39.4
Fe	26	7.87	10.7	24	1.76	16.8
Cu	29	8.96		≈ 20	1.43	15.1
W	74	19.3		1.14	≈ 8.1	9.6
Pb	82	11.35	10.0	6.9	0.65	17.1
U	92	18.7	9.56	6.2	0.32	10.5

Sampling calorimeters are built out of a multitude of successive active and passive layers. Particles lose their energy mainly in the passive materials. For electromagnetic calorimeters, high Z materials, whereas for hadron calorimeters metallic absorbers are preferred. The energy measurement takes place in the active material, typically made out of ionizing gases or liquids, scintillators or semiconductors. Hence, only a fraction of the total absorbed energy is deposited in the active layers. The sampling fraction characterizes this sharing of deposited energy and is defined as the ratio of the energy deposited in the active and passive layers.

Gas Detectors

4.1 Transport of Electrons and Ions in Gases

One of the most important issues about ionization detectors is to understand the ionization process and the movement of electrons and ions in the gas mixture, as these factors influence many operating characteristics of the detector. In, most of the cases, the movement of electrons and ions described by the classical kinetic theory of gases. We shall, therefore, devote some time to reviewing in the following sections, drift and diffusion, which are of particular importance.

On the microscopic scale, the electrons or ions that drift through the gas are scattered on the gas molecules so that their direction of motion is randomized in each collision. On the average, they assume a constant drift velocity u in the direction of the electric field E. The drift velocity u is much smaller than the instantaneous velocity c between collisions.

4.1.1 Diffusion

In the absence of an electric field, electrons and ions liberated by passing radiation diffuse uniformly outward from their point of creation. In the process they suffer multiple collisions with the gas molecules and lose their energy. They thus come quickly into thermal equilibrium with the gas and eventually recombine. At thermal energies, the velocities of the charges are described by the Maxwell distribution which gives a mean speed of

$$u = \sqrt{\frac{8kT}{m}} \tag{4.1}$$

where k is Boltzmann's constant , T the temperature and m the mass of the particle. Quite obviously, the average speed of the electrons is much greater than that of the ions due their smaller mass. At room temperature, the electron speed is a few times $10^6 cm/s$ while the positive ion speeds are on the order of $10^4 cm/s$.

From kinetic theory, the linear distribution of charges after diffusing a time t can be shown to be Gaussian:

$$\frac{dN}{N0} = \frac{N_0}{\sqrt{4\pi Dt}} e^{-\frac{x^2}{4Dt}} \tag{4.2}$$

where N_0 is the total number of charges, x the distance from the point of creation and D the diffusion coefficient. The rms spread in x is thus

$$\sigma(x) = \sqrt{2Dt}\frac{a}{b} \tag{4.3}$$

If three dimensions are considered, the spherical spread is given by

$$\sigma(r) = \sqrt{2Dt} \tag{4.4}$$

where r is the radial distance. The radial spread of ions in air under normal conditions, for example, is about 1 mm per second. The diffusion coefficient is a parameter which can be calculated from kinetic theory and can be shown to be

$$D = \frac{1}{3}u\lambda \tag{4.5}$$

where λ is the mean free path of the electron or ion in the gas. For a classical ideal gas, the mean free path is related to the temperature T, and the pressure p, by

$$\lambda = \frac{1}{\sqrt{2}} \cdot \frac{kT}{\sigma_0 p} \tag{4.6}$$

where σ_0 is the total cross section for a collision with a gas molecule. Substituting (4.1) and (4.6) into (4.5) gives the explicit expression where the dependence of D on the various parameters of the gas now becomes evident.

$$D = \frac{2}{3\sqrt{\pi}} \cdot \sqrt{\frac{(kT)^3}{m}} \tag{4.7}$$
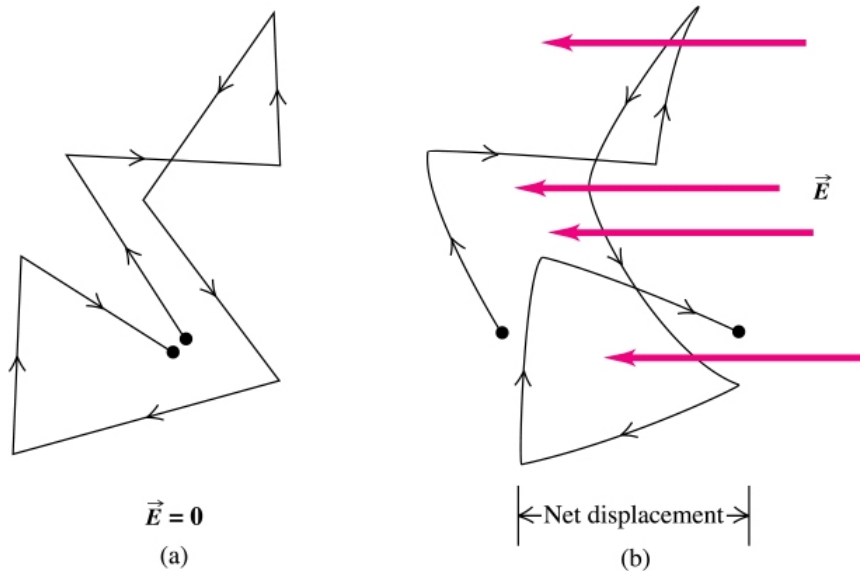
Figure 4.1: Diffusion (a) and drift(b)

4.1.2 Drift

In the presence of an electric field, the electrons and ions freed by radiation are accelerated along the field lines towards the anode and cathode respectively. This acceleration is interrupted by collisions with the gas molecules which limit the maximum average velocity which can be attained by the charge along the field direction. The average velocity attained is known as the drift velocity of the charge and is superimposed upon its normal random movement. Compared to their thermal velocities, the drift speed of the ions is slow; however, for electrons this can be much higher since they are much lighter.

In kinetic theory, it is useful to define the *mobility* of a charge as

$$\mu = \frac{u}{E} \tag{4.8}$$

where u is the drift velocity and the electric field strength. For positive ions, the drift velocity is found to depend linearly on the ratio E/p , (also known as the reduced electric field), up to relatively high electric fields. At a constant pressure, this implies that the mobility μ is a constant. For a given E, it is also quite clear that μ varies as the inverse of the pressure p.

For ideal gases, in which the moving charges remain in thermal equilibrium, the mobility can be shown to be related to the diffusion constant by

$$\frac{D}{\mu} = \frac{kT}{e} \tag{4.9}$$

Unlike positive ions, the mobility for electrons is much greater and is found to be a function of E. The electrons take advantage of their small mass and increase their velocity to high values:

$$u = \frac{eE}{2m_e}\tau \tag{4.10}$$

where τ is the mean time between two collisions of an electron (e, m_e) in an electric field E.

Velocities as high as a few times $10^6 cm/s$ can generally be attained before saturation sets in. The electric fields at this point are generally on the order of 1 kV/cm - atm.

In figure (4.2) the drift velocity versus the electric field for different gas mixtures, calculated by a simulation with Garfield is shown.

4.2   Ionisation mechanisms

The energy loss of a charged particle in matter is divided between two types of reaction: (a) excitation and (b) ionization in which a free electron and ion are created. The excitation of an atom X

$$X + p \rightarrow X + p$$
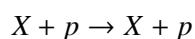
where p is a charged particle, is a resonant reaction which requires the correct amount of energy to be transferred. Typical cross sections in noble gases at resonance are on the order of $\sigma \sim 10^{-17} cm^2$. While no free electrons or ions are created, the excited molecule or atom may participate in further reactions which do result in ionization. For an ionization
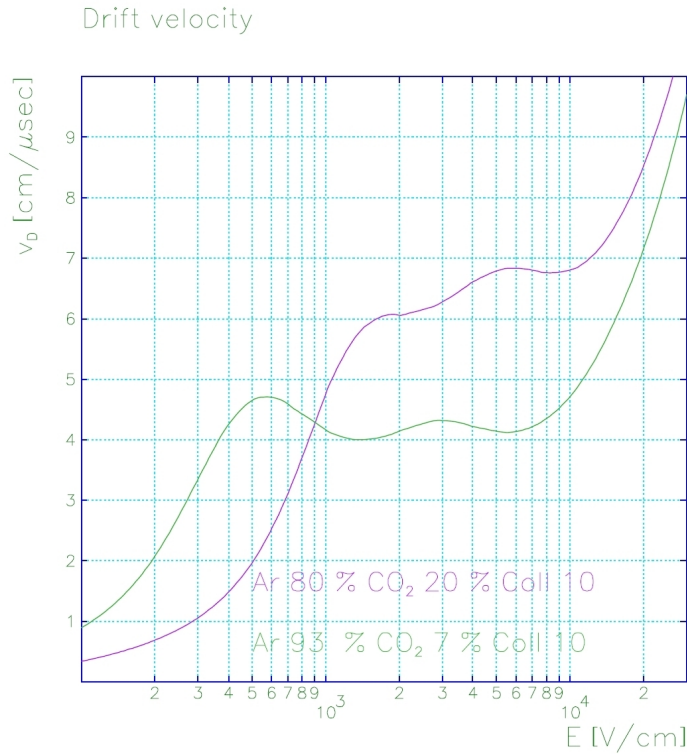
Figure 4.2: Drift velocity versus electric field

$$X + p \rightarrow X^+ + p + e$$
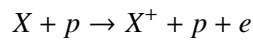
there is no energy requirement and its cross section is somewhat higher with $\sigma \simeq 10^{-16} cm^2$. However, ´the ionization process has an energy threshold which is relatively high, and since low energy transfers are more probable, the excitation reactions dominate.

The electrons and ions created by the incident radiation itself, are known as primary ionisation. In a number of these ionizations, however, a sufficiently large amount of energy is transferred to the electron(delta rays) such that this electron also creates further ionisation, the secondary ionisation. If the energy is high enough, the secondary ionization electrons may also ionize and so until the threshold for ionizing reactions is reached.

A second mechanism of ionization in gases is the Penning effect. In certain atoms, metastable states are excited which, because of the large spin-parity difference, are unable to deexcite immediately to the ground state by the emission of a photon. In such atoms, a deexcitation may occur through a collision with a second atom resulting in the ionization of the latter. Common examples are molecular gases on noble gases an noble gases on noble gases, e.g.

$$Ne + Ar \rightarrow Ne + Ar^+ + e$$
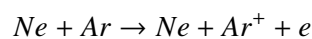
A third and important mechanism which occurs in noble gases is the formation of molecular ions. In this process, a positive gas ion interacts with a neutral atom of the same type to form molecular ion, i.e.

$$He^+ + He \rightarrow He_2^+$$
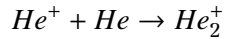
Mean number of electron-ion pairs

Since the occurrence of the ionizing reactions above is statistical in nature, two identical particles will not, in general, produce the same number of ion-electron pairs. We can ask, however: What is the average number of ion-electron pairs (from all mechanisms) created for a given energy loss? Note that this is not equal to the energy loss divided by the ionization potential, since some energy is also lost to excitation! For gases, this average turns out to be on the order of 1 ion-electron pair per 30 eV of energy lost, that is, for a 3 keV particle, an average of 3000/30 = 100 ion-electron pairs will be created. Moreover, what is surprising is that this average value does not depend very strongly on particle type and only weakly on the type of gas.

The average energy, w, required for creating an electron-ion pair is important since it determines the efficiency and the energy resolution of the detector. The resolution for a particle if energy E is

$$R = 2.35 \sqrt{\frac{Fw}{E}}$$

where F is the Fano factor for the gas medium, w the average energy required to produce an ionization is a fixed number. While the Fano factor is not well determined for most gases, it is clear that F is much less than 1.

Recombination and electron attachment

While the number of electron-ion pairs created is important for the efficiency and energy resolution of the detector, it is equally important that these pairs remain free, long enough to be collected. Two processes, in particular, hinder this option, recombination and attachment.

When there is no electric field, ion-electron pairs will generally recombine under force of their electric attraction, emitting a photon in the process,

$$X^+ + e \rightarrow X + hf$$
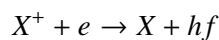
For molecular ions, a similar recombination reaction occurs,

$$X + Y^+ \rightarrow XY + hf$$
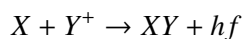
In general, the rate of recombinations will depend on the concentrations if the positive and negative ions so that,

$$dn = b \cdot n \cdot n^+ \cdot dt$$

where b is a constant dependent on the type of gas and n^+, n are the positive and negative ion concentrations respectively. If we set $n^+ = n = n$, integration then yield to the result

$$n = \frac{n_0}{1 + bn_0 t}$$

where n_0 is the initial concentration at t = 0.

Electron attachment involves the capture of free electrons by electronegative atoms to form negative ions,

$$e + X \rightarrow X + hf$$
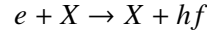
These are atoms which have an almost full outer electron shell so that the addition of an extra electron actually results in the release of energy. The negative ion formed consequently stable. The energy released in this capture is known as the electron affinity. Clearly, therefore, the presence of any , electronegative gases in the detector will severely diminish the efficiency of electron-ion collection by trapping the electrons before they can reach the electrodes. Some well known electronegative gases are O_2, H_2O, CO_2, CCl_4 και SF_6 . The noble gases He,Ne,Ar, in contrast, have negative electron affinities.

4.3   Multiplication factor

For moderate electric fields the energy carried by the electron will be rather constant on average, due to the random collisions with the gas molecules. However, for higher fields (in the time between collisions with the gas molecules) its energy may increase over the first ionization potential of the gas, and an electron-ion pair will be produced, while the first electron continues its travel possibly producing more pairs. In the same way, these secondary electrons can produce further ionization forming finally an avalanche. The mobility of the electron is much greater than that of the ions, therefore the electrons are the front of this cloud of charges, while the newly produced ions are still close, parting towards the first produced ions at their pace. The result of this movement is a drop-like distribution as shown in the schematic of figure (4.3)

The distance that this electron will travel until ionization defines the mean free path for ionization. Probably the most interesting quantity is the first Townsend coefficient α, the inverse of the mean free path of ionization. α represents the number of pairs produced per unit length of travel. If at some point there are n electrons, after they drift for a path dx

$$dn = n\alpha dx$$

new electrons will have been produced, hence the total number of electrons created in a path x is

$$n = n_0 e^{\alpha x}$$

where n_0 is the number of primary electrons. Then, the multiplication factor or gas gain given by

$$G = \frac{n}{n_0} = e^{\alpha x} \tag{4.11}$$
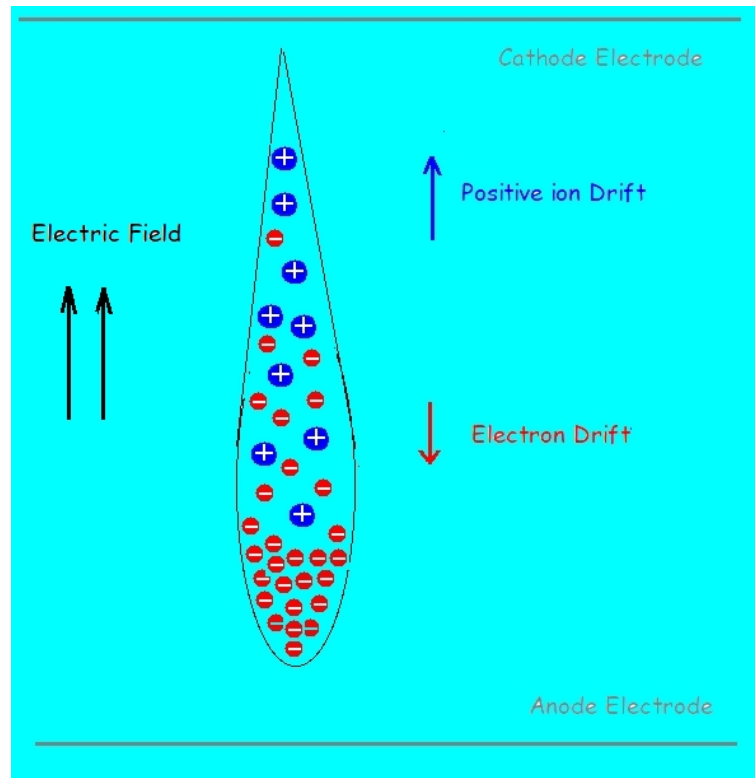
Figure 4.3: The drop-like shape of an avalanche.

In the general case of a non-uniform electric field, $\alpha = \alpha(x)$ and G can be expressed as

$$G = e^{\int_{r_1}^{r_2} \alpha(x)dx} \tag{4.12}$$

Figures 4.4(a) and 4.4(b) show the multiplication factor and the first Townsend coefficient for different gas mixtures, measured with a micromegas detector using a ^{55}Fe source.

The multiplication factor has an upper limit and cannot be increased at will. Secondary processes, like photon emission inducing the generation of avalanches spread over the gas volume, and space-charge deformation of the electric field (which is strongly increased near the front of the avalanche), eventually result in a spark breakdown. A phenomenological limit for the multiplication before breakdown is given by the Raether limit,

$$G < 10^8 \quad \text{or} \quad \alpha x < 20$$

The statistical distribution of the energy of electrons, and therefore of G, in general does not allow the operation at average gains above 10^6 in order to avoid breakdowns. Notice also that by increasing the gap thickness, the Raether condition will be met at decreasing values of α, in other words, for a given field strength, the breakdown probability increases with the gap thickness.

In general, the primary amount of electrons are not enough for efficient detection. The solution for that is to amplify our signal via the avalanche process in a proper gas mixture that contains a noble gas. The choice of noble gas is made because they are not electronegative and therefore they do not capture free electrons that are going to produce our signal. Typical noble gases,

(a) Gas gain versus mesh voltage

(b) First Townsend coefficient versus electric field
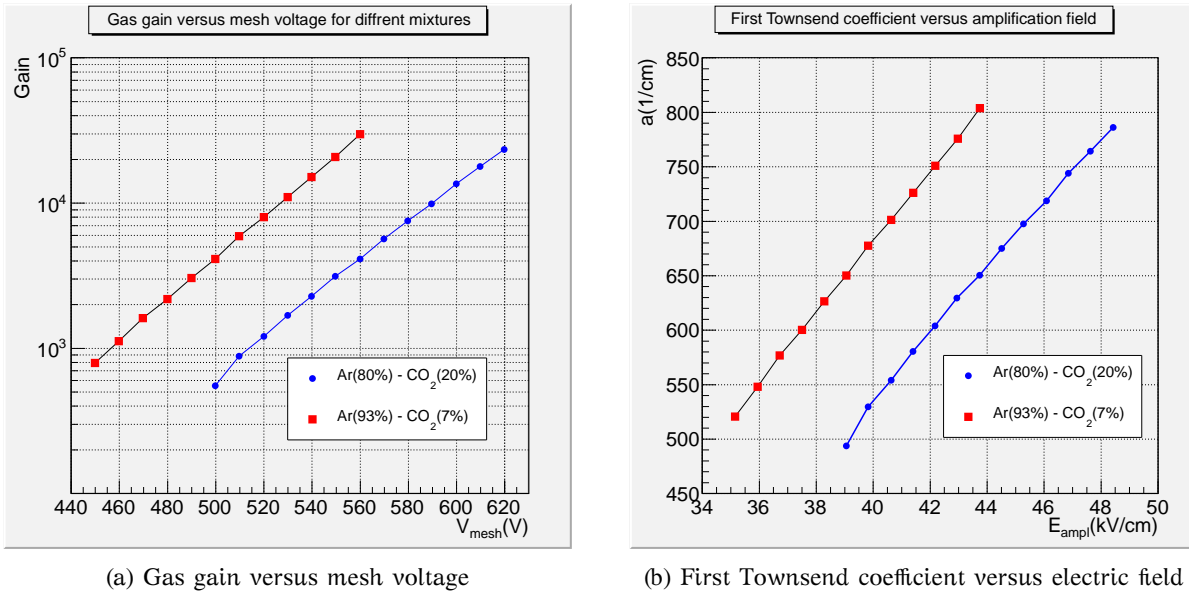
Figure 4.4: Comparison of gas gain versus mesh voltage in (a) and first Townsend coefficient versus electric field in (b), for different gas mixtures.

which have low ionizing potential, are *Ar*, *Kr* and *Xe*. A detector with only *Ar* as a gas is not possible to provide a gain greater than $10^3 - 10^4$. That came as a result of the behavior of the excited noble gas. The noble gas that is usually used, deexcite emitting a photon with energy bigger than the ionizing potential of the metal that is usually used inside the detector.

In order to suppress this phenomenon the addition of a quantity of a polyatomic gas to the detector is done. This molecules have a lot of different ways of excitations and that gives them the advantage to be able to adsorb a wide range energetic photons without being obliged to deexcite by photon emissions (i.e. methane CH_4 can absorb photons with energy starting from 7.9 *eV* to 14.5 *eV*, CO_2 can absorb the range of 6.2 *eV* to 15.8). This process called quenching and with that we are able to use noble gases to detectors with gain up to 10^6. The usage of polyatomic gas to the detector leads to some unpleasant chemicals processes which cause the density of them to decrease. In order to overcome that we take care to renew the whole volume of the gas inside the detector with constant flux.

4.4 The Micromegas Detector

Micromegas (which stands for MICRO MEsh GAseous Structure) detector was introduced by G. Charpak and Y. Giomataris in the middle '90s. In the beginning it was proposed to detect low energy photons (1 – 10 *keV*). Micromegas is a high gain gaseous detector, which can stand up alone without the need of an additional preamplification. The Micromegas technique is based on the gaseous micropattern detector technology and is well known for its:

- Excellent stability and fast response.

- High energy and excellent spatial resolution.

- Low cost and robust construction.

- High radiation resistance.

The detector covering the special needs of many experiments has been already used in COM-PASS, NA48, CAST, n-TOF it is already approved for the ATLAS Muon detector upgrade (MAMMA[1]). It is also under study for low energy neutrino experiments i.e. HELLAZ, NOSTOS or possible applications in medical physics.

Description of the detector

Micromegas is a gaseous parallel plate detector in which several innovative properties rely on a narrow amplification space, typically 128 μm, between two parallel electrodes, the cathode and anode conducting plates. The cathode is made of a thin metallic electrode, few microns thick, while the anode (could be used strips or pads) of a conductor, printed on a insulator board, PCB (Printed Circuit Board). The technological challenge of such a detector is to keep the small gap constant over the active area. The cathode - anode distance is kept stable throughout the whole active area by small insulating pillars every 2 mm, deposited by standard photographic methods on the anode or cathode, covering a small part (~1%) of the surface. This technical solution gives the opportunity to construct large surface chambers up to $1 \times 1 m^2$ easily.
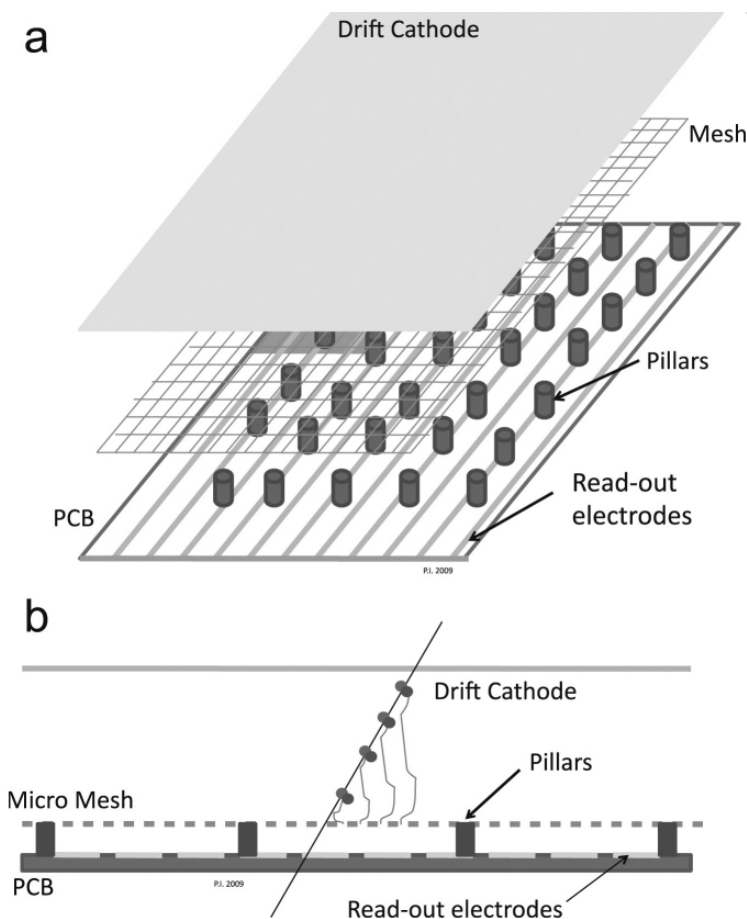
Figure 4.5: Illustration of a typical micromegas detector

The operation principle can easily be described with the help of figure 4.5 where all the basic elements are shown. We can see that the micromesh (grid) is separating the detector volume in

---

[1]MAMMA = Muon ATLAS MicroMegas Activity. It is proposed to develop muon chambers based on the Mi-croMegas technique of approximate size of $1m \times 2m$ that would combine precision measurement and triggering capability.

two regions. The upper one (between micromesh and cathode) is called drift region and extent for 3-5 *mm*. This is the first part of the detector that the incoming particles have to cross. The electric field there, is rather weak (of the order of 1 *KV/cm*). In this volume the ion-electron pair production takes place. The electrons guided by the electric field are drifting towards the next region and the ions are collected by the cathode.

The region between the micromesh and the anode (PCB) is called amplification region and is extended for about 128 *μm*. The role of the grid is multiple, and does more than marking the end of the conversion gap (drift area) and the beginning of the amplification one. It is made out of copper (5 *μm*) with a process which relies on the photolithograhy technique that allows to print on it 50 *μm* openings and a pitch of 100 *μm* (see figure 4.6). At the same time, micromesh provide an easy access to electrons to the amplification region, while it prevents ions created through the avalanche to enter there. The voltage applied to it (up to 400 *V*) is such that the ratio of the electric field in the amplification gap over the field of the conversion gap is very big. The bigger the ratio the higher the electron transmission to the amplification gap reached. Having a small ratio of electric fields can cause the mesh to loose its transparency to electron passing through. Once in the amplification gap, the avalanche is easily started; the gap is so small that the electric field achieved is very high (up to 30-50 *KV/cm*). At the same time as providing a smooth way for the electrons into the amplification gap, the micromesh prevents the ions produced by the avalanche to enter the conversion gap.
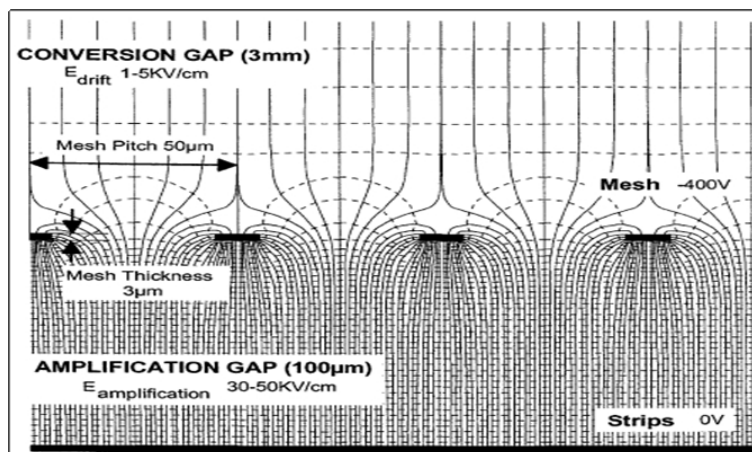
Figure 4.6: Electric field lines of micromegas detector

While the ions are collected by the grid with a high efficiency and speed (which sometimes is used as an inside trigger signal), the electrons continue in the amplification gap and end their travel on the anode electrode. The anode electrode consists of 96 copper strips with a typical size of 150 *μm* and distance 100 *μm*, grounded through low-noise charge preamplifiers of high gain to an isolating layer (usually kapton).

The knowledge of the shape of the electric field lines close to the grid is a key issue for an optimal operation of the detector and especially for an efficient transfer of electrons to the amplification gap, where the avalanche and the signal readout take place. The uniformity of the electric field in the amplification area is easy to obtain, despite the smallness of the gap and insures a good stability in the development of the avalanche. The electric field shape is, however, disturbed around the holes of the micromesh (figure 4.6). Its knowledge is a fundamental issue for the operation of the detector, especially for the efficiency of the passage of the electrons through the holes, as well as for the fast evacuation of the positive ions. The fraction of the electric field lines due to the charge distribution on the outer part of the mesh exhibits a funnel-like shape

<table>
</table>

(a)	(b)
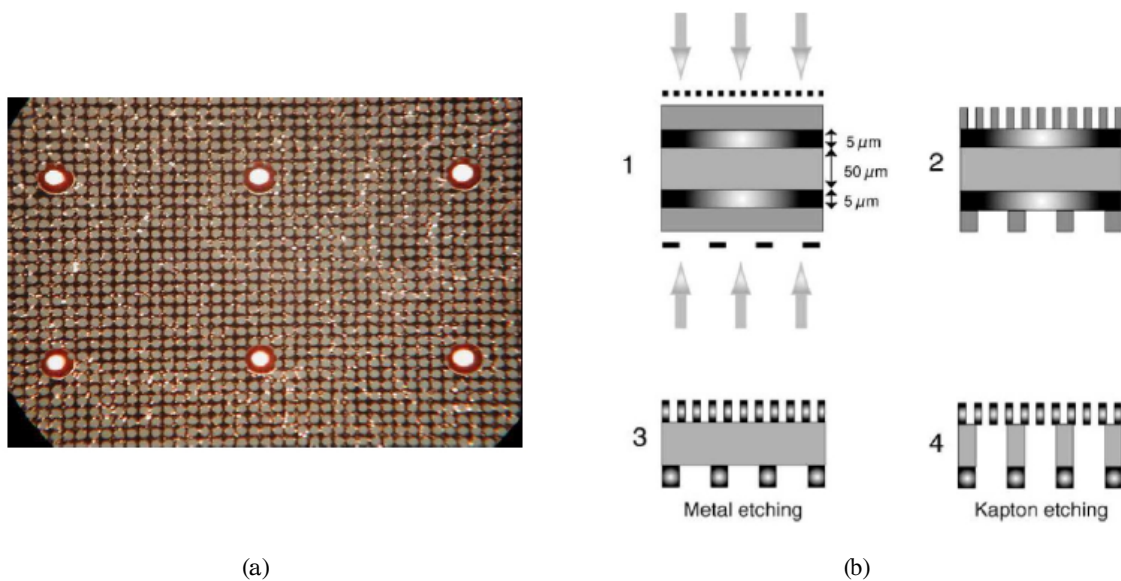
Figure 4.7: (a) A photography of the micromesh taken with a microscope. (b) Photolithography process for fabrication.

close to the openings of the grid. With a thin micromesh, as long as the amplification field is one order of magnitude larger than the field in the conversion region, any field line coming from the top of the mesh does not return to the bottom of the mesh. As a consequence, most of the electrons pass through the holes of the micromesh and are fully collected by the anode plane. The electric field lines from the top of the mesh also play an important role in the fast collection of the positive ions.

The amplification inside the holes of the mesh is negligible. It is in this respect different from all other structures with amplification in holes, tubes or slits. It is convenient for some applications to increase the field inside the conversion region in order to produce some preamplification. Due to the small pitch of the holes in the grid, the time dispersion in the path length of the different electron trajectories is very small. Therefore, the detector can provide an excellent time resolution. The transverse development of the induced signal is limited to a small area of the anode elements and therefore can provide an excellent spatial resolution. Very high reachable gain allows the detection of single electrons with a high efficiency, an exceptional property in the panel of the gaseous detectors.

The signal on the anode strips or the cathode mesh is induced by the movement of the negative electrons towards the anode and the positive ions towards the cathode. The charge signal due to the positive ions drifting to the micromesh electrode, which takes place typically at about $100ns$ is depending on the width of the amplification gap and on the gas mixture. Whereas, the fast current signal is mainly due to the electrons because of their higher mobility as mentioned in previous chapter. In Micromegas, the fast collection of the ions highly reduces the space charge effect which limits the gain in the common gaseous detectors in a high rate environment. It is known that parallel plate detectors exhibit high radiation resistance. The electric field is homogeneous over the whole amplification gap and accumulation of undesirable effects, like polymerization during the avalanche process, has a very small effect. The radiation resistance of the detector has been tested in the laboratory using an intense *X*-ray generator.

RD51 & CALICE testbeam

5.1 RD51 Collaboration

The proposed R&D collaboration, RD51, aims at facilitating the development of advanced gas-avalanche detector technologies and associated electronic-readout systems, for applications in basic and applied research. The main objective of the R&D programme is to advance technological development and application of Micropattern Gas Detectors.

The invention of Micro-Pattern Gas Detectors (MPGD), in particular the Gas Electron Multiplier (GEM), the Micro-Mesh Gaseous Structure (Micromegas), and more recently other micro pattern detector schemes, offers the potential to develop new gaseous detectors with unprecedented spatial resolution, high rate capability, large sensitive area, operational stability and radiation hardness. In some applications, requiring very large-area coverage with moderate spatial resolutions, more coarse Macro-pattern detectors, e.g. Thick-GEMs (THGEM) or patterned resistive-plate devices could offer an interesting and economic solution. The design of the new micro-pattern devices appears suitable for industrial production. In addition, the availability of highly integrated amplification and readout electronics allows for the design of gas-detector systems with channel densities comparable to that of modern silicon detectors. Modern wafer post-processing allows for the integration of gas-amplification structures directly on top of a pixelized readout chip. Thanks to these recent developments, particle detection through the ionization of gas has large fields of application in future particle, nuclear and astro-particle physics experiments with and without accelerators.

The RD51 collaboration involves ~ 450 authors, 75 Universities and Research Laboratories from 25 countries in Europe, America, Asia and Africa. All partners are already actively pursuing either basic- or application-oriented R&D involving a variety of MPGD concepts. The collaboration established common goals, like experimental and simulation tools, characterization concepts and methods, common infrastructures at test beams and irradiation facilities, and methods and infrastructures for MPGD production.

5.2 CALICE Collaboration

The CALICE collaboration was formed in 2001 with the goal to develop and propose options for highly granular calorimeters at future lepton colliders (LC) at the TeV scale. Today, the

most advanced proposal for such a machine is the International Linear Collider (ILC), which can operate at center-of-mass energies between about 0.1 TeV to 1 TeV. In the longer term the Compact LInear Collider, CLIC aims to reach center-of-mass energies of up to 3 TeV. Even more in the future is the project of a Muon Collider. CALICE is investigating several technological options for both electromagnetic calorimeters (ECAL) and hadronic calorimeters (HCAL), based on the particle flow approach.

Within the particle flow paradigm the principal role of the ECAL is to identify photons and measure their energy. The capability to separate photons from each other and from near-by hadrons is of primordial importance. The ECAL forms the first section for hadron showers and with its fine segmentation plays also an important role in the hadron hadron separation.

The role of the hadron calorimeter is to measure the energy associated with neutral hadronic particles, such as neutrons and long living Kaons. In this approach the challenge is to unambiguously identify energy deposits in the calorimeter as belonging to charged particles (and therefore to be ignored) or to neutral particles (and therefore to be measured). As a consequence, the optimal application of PFAs requires calorimeters with the finest possible segmentation of the readout.

Particle flow imposes further requirements on the active element. The calorimeters will be located inside the coil. Therefore the thickness of the active elements needs to be minimized, to keep the coil radius as small as possible. The noise rate needs to be reasonably small, to keep the confusion term manageable. Finally, the active elements need to satisfy general performance criteria, such as reliability, stability, a certain rate capability and be affordable.

The CALICE effort involves test beam campaigns with necessarily large installations, and due to the high granularity, some of these have channel counts exceeding those of the largest LHC calorimeter systems. This is only possible by maximizing the use of common infrastructure such as mechanical devices, electronics architectures and data acquisition systems, and by working within a common software and analysis framework that facilitates combination and comparison of test beam data. Over time, this has allowed CALICE to build up collaborative expertise and to achieve a common understanding of the relative strengths and weaknesses of the technologies under consideration.

The development of calorimeter prototypes is roughly organized in two steps, which in practice may overlap, of course. Firstly, "physics" prototypes provide a proof-of-principle of the viability of a given technology in terms of construction, operation and performance. In addition they are used to collect the large data sets which are invaluable for testing shower simulation programs, and for the development of particle flow reconstruction algorithms with real data. On the other hand, "technological" prototypes address the issues of scaling, integration and cost optimization. They are required for each technology, but many large area and multilayer issues have initially been addressed with so-called demonstrators, before instrumenting a full volume for larger scale system tests.

5.3   Experimental conditions

This chapter deals with the detector setup that used during the RD51 & CALICE testbeam at August 2011. The experiments took place at the SPS/H4[1] facility at CERN's Previssin site. The setup that installed, consisted of a new micromegas prototype constructed at LAPP[2] and a

---

[1] Super Proton Synchrotron
[2] Laboratoire d'Annecy-le-Vieux de Physique des Particules - CNRS/IN2P3
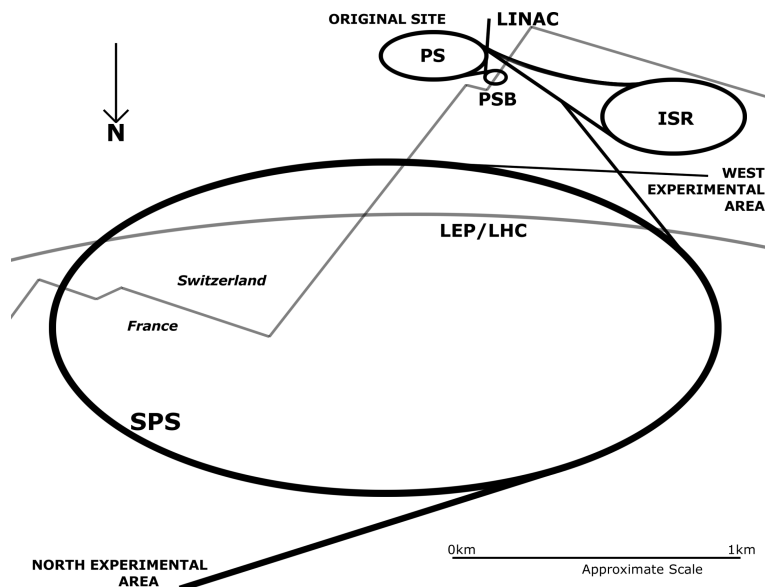
Figure 5.1: Super Proton Synchrotron's ring layout.

micromegas telescope, used for tracking, while scintillators plus photomultipliers for triggering. The prototype tested to muon and pions beams for 18 days during August. The whole setup is shown at the picture below.
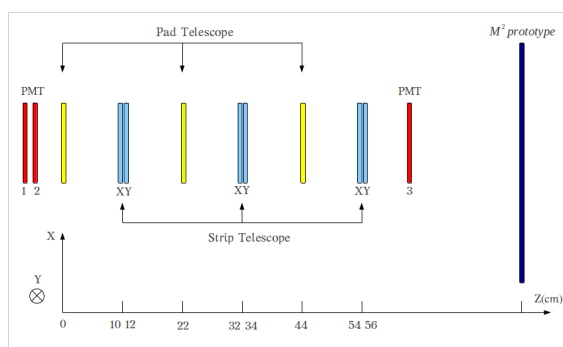
(a) Detector setup
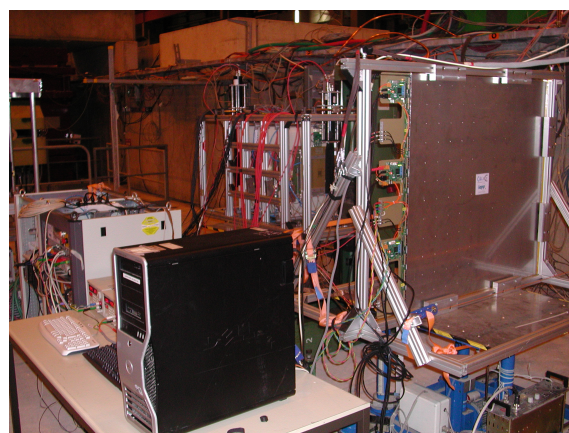
(b) Photo from taken at the testbeam

Figure 5.2: (a) Illustration of the detector setup that used (b) Photo taken at the testbeam area.

My analysis involves the strip telescope and the prototype, therefore, a detailed description of these detectors follows.

5.4 The RD51 Micromegas Telescope

5.4.1 Description of the telescope

The RD51 micromegas telescope designed and developed under the collaboration of National Technical University of Athens (NTUA) and National Center for Scientific Research "Demokri-

tos".

The telescope consists of three identical stations of *double* Micromegas detectors. The term double micromegas used to mention that there are two micromegas placed back to back and not two separate chambers. For each station there is a common frame which is actually the drift electrode. Alongside the common frame are placed two different mesh electrodes plus the PCB boards with the strips. Therefore, for each station three high voltage lines, one for the drift and two for the two mesh are required. The fact that we have two PCBs (dimension: 10×10 cm^2) board per station, one caring the X-strips and the other rotated by 90 degrees caring the Y-strips, gives the opportunity to measure both x and y position. Both PCBs, contain 96 strips with a pitch of $250\mu m$, give an active area of 2.4×10 cm at each PCB and total active area of 2.4×2.4 cm (96×250µm = 2.4 cm). A schematic that describe a single station can be found at figure (5.3)

(a) The station   **(b)** The strips
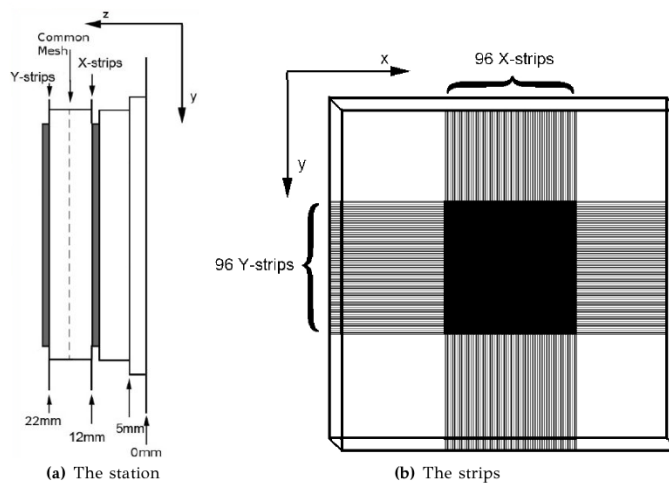
Figure 5.3: (a) Schematic of the double micromegas detector used in the tracker. The distances notated below the schematic are the distances from the mounting point (notated as 0 mm). (b) Schematic of the two PCB planes (10×10 cm) having 96 strips each at the center. The active area is a square box (2.4×2.4 cm) at the center of the station.

5.4.2   Analog readout

The data acquisition system that used in order to obtain the information needed from the telescope is based on analog readout with Gassiplex cards. The main parts of the system that used is:

- Tree scintillators plus photomultipliers passing a NIM discriminator before the NIM coincidence unit

- Two gassiplex cards (N^o613V) per station.

- One C-RAM sequencer (CAEN V-550).

- Five ADC converters (CAEN V-551).

- High Voltage power supply (CAEN SY2527).

- Online monitoring provided by the data acquisition software CENTAURE created by SUB-ATECH.

A simple illustration of the readout system for a telescope station is shown in figure 5.4
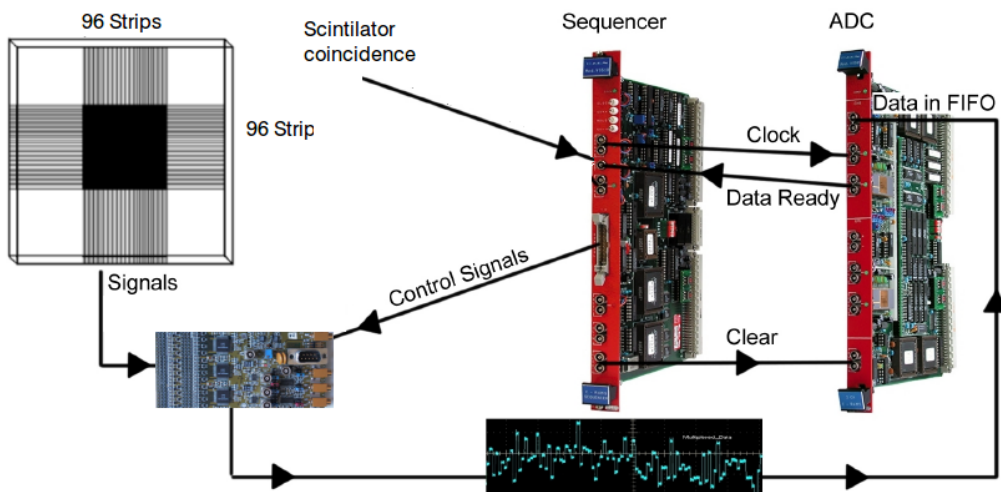
Figure 5.4: System used for analog readout

The trigger signal is external acquired from the scintillators and then send to a sequencer. With the arrival of the trigger signal, the readout sequence starts. When the sequence ends, the control signals that have been created, are sent to the gassiplex card connected to the chamber. With that signals the card is multiplexing all 96 channels of the chamber and sends the data to the ADC converter. Some properties of the gassiplex card are summarized in the next table.

Peaking time	1.2 μs
Peaking time adjust	1.1 to 1.3 μs
Noise at pF	530 e^- rms
Noise slope	11.2 e^- rms/pF
Dynamic range(+)	560 fC (0 to 2V)
Dynamic range(-)	300 fC (0 to 1.1V)
Gain	3.6 mV/fC
Non linearity	$\pm 2 fC$
Baseline recovery	$\pm 5\%$ after 5 μs
Analog readout speed	10MHz (50 pF load)
Power consumption n	8 $mW/chan.$ At 10 MHz
Output temp. coef.	0.05 $mV/^oC$

5.5 The one square meter Micromegas prototype

5.5.1 Description of the prototype

Hermeticity requirements and huge number of channels of an ILC/CLIC HCAL, make it unavoidable to integrate front-end ASIC on detectors. Therefore, LAPP group and CERN workshop made the Bulk process compatible with ASIC equipped PCB. Optimized for the efficient detection of Micromegas signals, a new ASIC called MICROROC was developed by the LAL/Omega group and the LAPP electronics department.The final assembly, called an Active Sensor Unit or

ASU, consists of a PCB with $1\,cm^2$ pads plus mesh on one side and ASICs on the other side (figure **??** left).
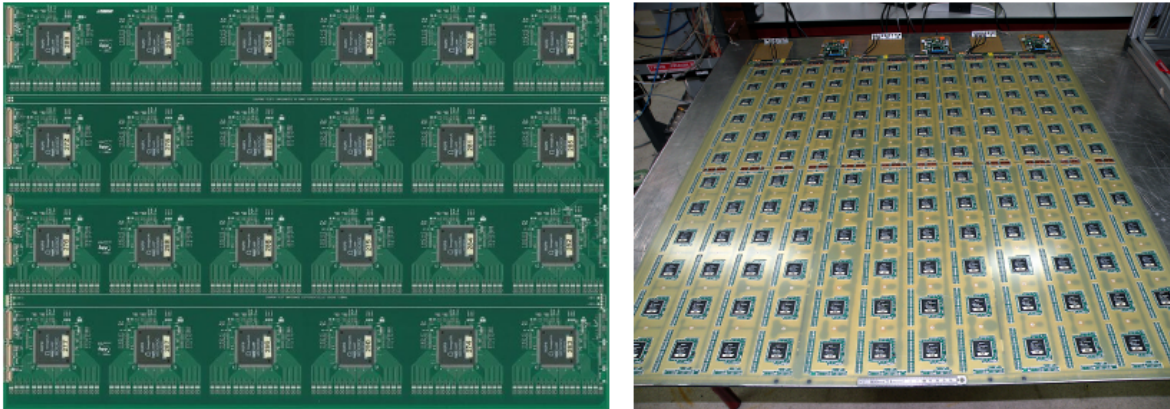
Figure 5.5: Photographs of an Active Sensor Unit and the $1\,m^2$ prototype during assembly.

The large scale prototype is a 1×1 m^2 chamber with 9216 readout channels (or 96×96 pads). In order to construct the prototype, the active sensor units (ASUs), are glued first in couples, on the stainless steel supporting plate. They are surrounded by a plastic frame and covered by another stainless steel plate which holds a copper drift electrode(cathode). Between the junction of two ASUs there is a 5mm spacer, to keep the ASUs in the correct position. The 3 mm drift gap is defined by the frame height and is kept constant over all chamber area by tiny spacers placed between the ASUs. Each ASU consists of woven mesh and a PCB with 48×32 readout pads of 1×1 cm^2 and 24 MICROROC chips.

The readout of two ASU is chained serially and connected to the data acquisition system by three detector interface boards (DIF). The DIF is a mezzanine board, it allows to load the ASIC configuration, readout the data from the ASIC memory and also to provide system clock and power. Another board, called inter-DIF, is placed between the DIF and the ASU to provide voltage to drift and mesh electrodes ($\leq 500\,V$). The addition of the DIF, the inter-DIF and two ASUs, gives one fraction of the total detector called slab. The gas is distributed by one inlet and outlet traversing the frame of the chamber whose total thickness is about $1\,cm$.

Finally, the one square meter prototype consists of 3 slabs i.e. two ASUs plus DIF and inter-DIF. This design introduces a very little fraction(below 2%) of dead area due to the ASU junction compared to the total active area of the detector (see 5.6). These dead areas are very important and one crucial question about the prototype performance is the response of the detector near the dead areas.

5.5.2   Semi-Digital readout with MICROROC ASIC

MICROROC is a 64 channels integrated circuit, made in AMS SiGe $0.35\mu m$ technology. Its area is 20 mm^2 and each channel consists in (Fig 5.7):

- A spark protection network.

- A charge preamplifier.

- Two shapers (low gain and high gain).
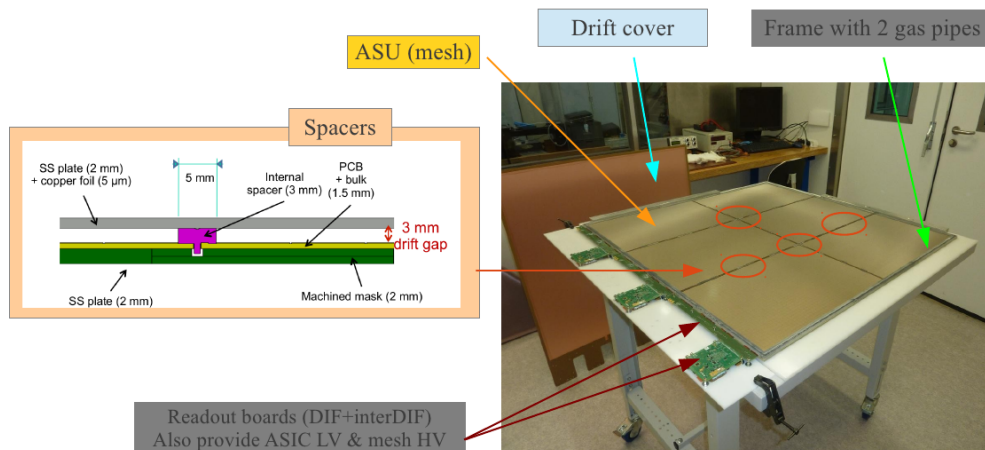
Figure 5.6: Dead areas of the detector because of the ASU junction.

- Three discriminators with a 2-bit encoder.

- A shared 127 event digital memory.

- A 24-bit bunch-crossing identifier counter @5MHz (BCID).

The operation of MICROROC is optimized for the ILC beam structure which is divided into two main phases. During the first phase the beam is on ($1ms$): for each channel, the detector signal is collected and the resulting voltage pulse amplitude is compared to three programmable thresholds. Every $200ns$, the result is latched and stored inside the digital memory if at least one channel has a charge above the lowest threshold (auto-trigger mode), and associated with a 24 bit time stamp (BCID).

During the second phase ($199ms$), i.e. between two bunch trains, the analog part is powered down, and a serial daisy-chained readout is performed. For test with cosmic or beam particles, an external trigger is available, as well as an analog multiplexed readout for detector fine characterization.

In order to reduce inter channel disparities, a 4-bit DAC per channel is included to tune the reference voltage of the high gain shaper and thus compensate its offset. This allows to have uniform low threshold for all channels of one chip.

The output of the high gain shaper is connected to 2 discriminators which are used to define the low and medium channel threshold while a third discriminator, linked to the low gain shaper, is available to set the high threshold.

The 3 thresholds are common to the 64 chip channels. A 4-bit offset, however, can be used to vary the individual pedestal positions. It virtually provides a channel to channel control of the 3 thresholds. A detailed characterization of ASICs was carried out to verify their overall functionality and determine their settings (offsets and thresholds).

The printed circuit board is a 8-layer PCB, with impedance controlled strips (50Ω for calibration and 100Ω for differential LVDS clocks), with $1.2mm$ thickness. The anode pads are copper squares of $9.8 \times 9.8mm^2$ with 1cm pitch, and the PCB final dimension is $32 \times 48cm^2$ (1536 pads), so that each PCB hosts 24 MICROROC circuits (figure 5.7). There are two possible cabling, according to the place of the PCB inside the detector, i.e. without or with termination network for respectively first/middle and last PCB of a chain. The ground plane below the anodes has been hatched to reduce detector capacitance, thus reducing noise.
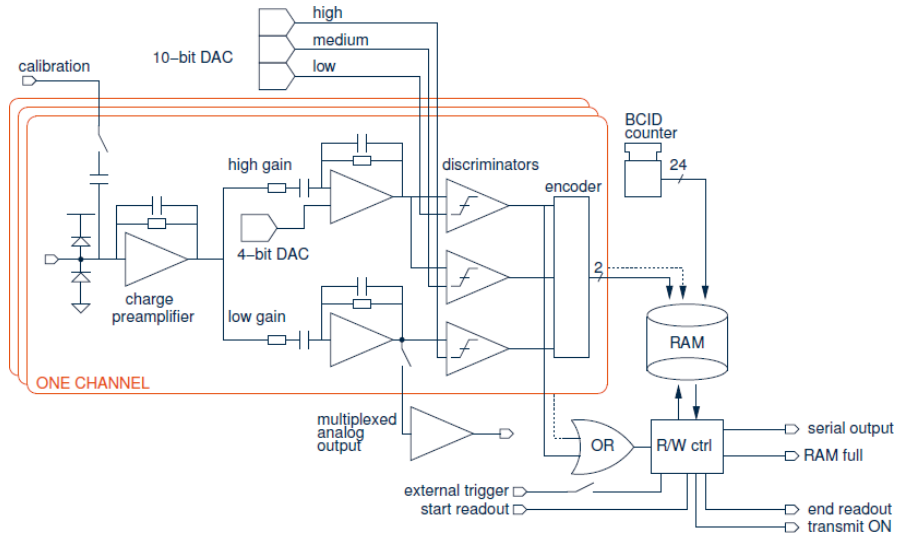
Figure 5.7: Schema of the MICROROC circuitry.
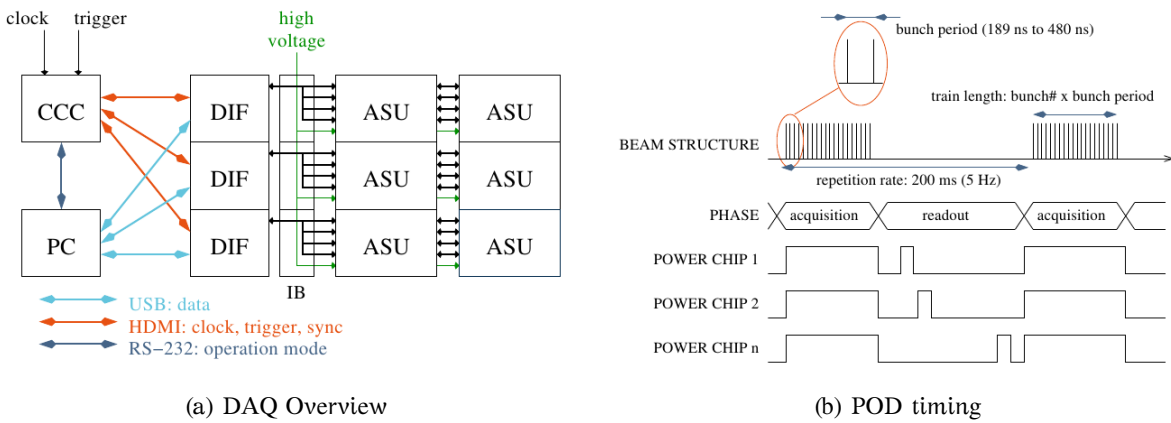
(a) DAQ Overview

(b) POD timing

Figure 5.8: Data acquisition.

Because of the very high number of electronic channels foreseen in a complete calorimeter, MICROROC is embedded inside the detector and is designed to be chained without any external circuitry. Open collector output signals and daisy-chained token are used to minimize the number of output lines on the detector.

There is one serial output which is transferred to the DAQ during the inter bunch. Control tokens are daisy chained across the PCB. Moreover, to save power, during the inter bunch the POD (Power-On Digital) module shuts down the transceivers of chips which are not transmitting data (5.8(b)). The data format is: `chipID+BCID+depth(datachannels)`.

Both ASIC and PCB have two redundant lines for data acquisition control and readout, selectable by a configuration register. This allows to bypass one or several chip in the readout chain. Each ASU line is read independently, in order to ensure maximum reliability: if an unrecoverable hardware failure occurs, only a line is lost, not the whole detector.

This kind of detector is foreseen to be read out by the so-called CALICE DAQ. At the moment, this system is under development, therefore a Labview based DAQ with USB link is used. An acquisition rate up to $500Hz$ ($200Hz$ with telescope synchronization) has been reached. All triggers and acquisition mode commands are distributed in a synchronous way, with the Clock and Control Card (5.8(a)). A Labview based software allows to manage the ASIC configuration files (pedestal, thresholds, offsets), test ASIC, test ASU, record data in test-box and record data of the whole detector, with or without external trigger, because of its versatility. It also provides a simple display for online monitoring which is used to verify the overall response of the detector. Data analysis are performed off-line with the ROOT-based framework.

Treatment of telescope data

6.1 Introduction

The telescope and the square meter prototype were installed in SPS/H4 for 18 days during August 2011. At an average trigger rate of 100 Hz per spill, 6 millions muons(6.1(a)) and pions(6.1(b)) in the ratio 85/15 were recorded. Muons were used to assess the prototype performance to MIPs under various detector settings. Shower signals were measured with a pion beam focused at a small iron block placed 0.5 m upstream of the prototype. The telescope and the prototype each placed on a movable table, while the gas distribution panel, two racks with trigger electronics, power supplies and a fast acquisition PC completed the setup.
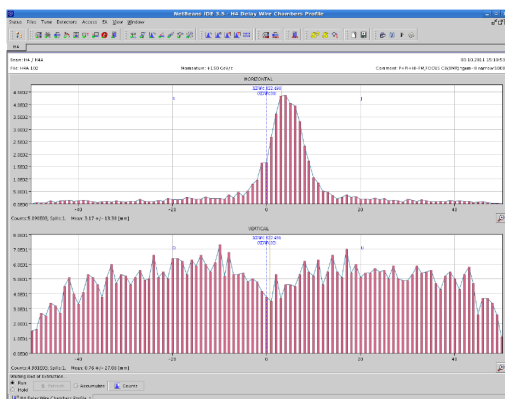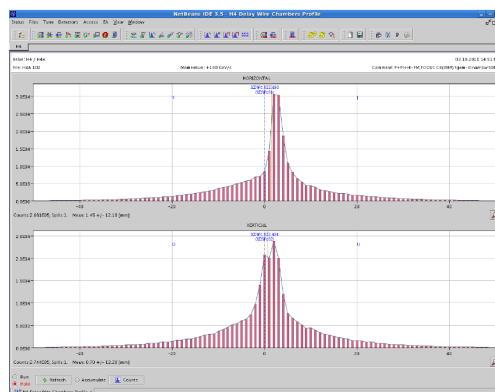
(a) Muon beam profile   (b) Pion beam profile

Figure 6.1: In this figure the muon in (a) and the pion beam profile in (b), that used during the testbeam is shown.

All the detectors were flushed with a non flammable gas mixture of $Ar/CF_4/iC_4H_{10}$ 95/3/2 the so called *T2K* gas, at a total flow of 4 l/h. The mesh and drift voltage for the telescope chambers adjusted at $420V$ and $530V$ respectively, while for the photomultipliers 1,2 and 3 adjusted at $1700V$, $1750V$ and $1750V$.

6.2 Micromegas Framework

The Micromegas Framework [1] is a C++ based framework created by LAPP in order to support
the data analysis of the linear collider group activities. The fact that the framework developed
with the C++ language, makes it to co-operate perfectly with ROOT, so that every one who
wants, can use it for data analysis.

The framework is a common software for both analog and digital readout and also supports
micromegas detectors with strip or pad readout. The output files from the acquisition program
stored in the computer and then the data reconstruction to root files is performed using the
framework so that each user can compose his own analysis scripts. All the information needed
for the reconstruction, contained in a xml file (an example xml file follows).

Code/telescope.xml

```
 1  <micromegas xmlns:run="http://lappweb.in2p3.fr/LC">
 2  <run name="cal01"/>
 3  <info date="200411"/>
 4  <input path="/Telescope/Beam/Labview files/b1208 6.acq" type="centaure"/>
 5  <output path="/New Reco/Telescope/b1208 6.root" />
 6
 7  <detector name="calibMicroroc" description = "Micromegas Strip Telescope">
 8
 9      <chamber type="GASSIPLEXSTRIPCHAMBER1"  xPos="3" yPos="8" zPos="56" xRotation= "false" ↩
            yRotation = "false" zRotation="90" stripHorizontal = "true"  id="1"/>
10      <chamber type="GASSIPLEXSTRIPCHAMBER1"  xPos="3" yPos="8" zPos="54" xRotation= "false" ↩
            yRotation = "false" zRotation="90" stripHorizontal = "false" id="2"/>
11      <chamber type="GASSIPLEXSTRIPCHAMBER1"  xPos="3" yPos="8" zPos="34" xRotation= "false" ↩
            yRotation = "false" zRotation="90" stripHorizontal = "true"  id="3"/>
12      <chamber type="GASSIPLEXSTRIPCHAMBER1"  xPos="3" yPos="8" zPos="32" xRotation= "false" ↩
            yRotation = "false" zRotation="90" stripHorizontal = "false" id="4"/>
13      <chamber type="GASSIPLEXSTRIPCHAMBER1"  xPos="3" yPos="8" zPos="12" xRotation= "false" ↩
            yRotation = "false" zRotation="90" stripHorizontal = "true"  id="5"/>
14      <chamber type="GASSIPLEXSTRIPCHAMBER1"  xPos="3" yPos="8" zPos="10" xRotation= "false" ↩
            yRotation = "false" zRotation="90" stripHorizontal = "false" id="6"/>
15
16    </detector>
17  </micromegas>
```
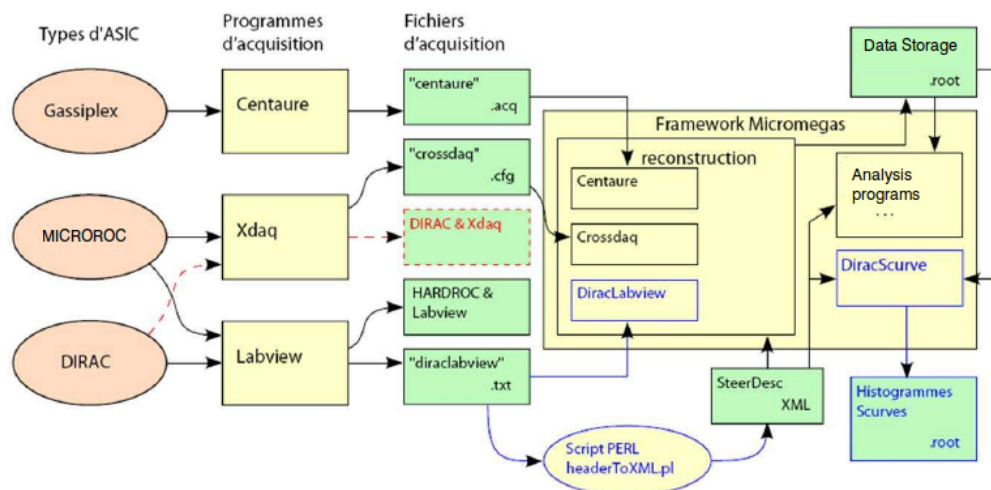

Figure 6.2: Micromegas framework block diagram

---

[1] http://lappweb.in2p3.fr/LC/Doxygen/pro/index.html

6.3   Pedestal subtraction for the telescope

One critical point for the detector operation is to understand the background level of the detector's signal. Telescope chambers contain 96 strips, therefore the information we have consists of 96 integers, (one per ADC channel) which correspond to the charge collected at each strip. Theoretically, we expect non zero values only for strips which collect charge due to the amplification of primary electrons that insert to the amplification gap. Unfortunately our world is not ideal and as a result there is always background superimposed with the expected signal. A large fraction of the background added by the electronic noise. In order to remove the background, we turn on the detector voltage and record data for some time without a radiation source or a particle beam. This is what we call a pedestal run. With the appropriate data analysis of a pedestal run we can define the pedestal position of each channel and then subtract it from the original data, so that the new data, contain in a good approximation signals due to the particle interaction in the detector and prevent us to record fake noise hits. In the next figures is shown a simple event before (6.3(a)) and after(6.3(b)) pedestal subtraction

Knowing the pedestal position, we have to define an value to subtract. In order to do this we follow a procedure:

- Find pedestal position of each channel for each chamber(i.e each gassiplex card).

- Fit a Gaussian distribution to each channel for each chamber.

- Obtain the parameters of the previous fit and fill histograms with mean and sigma distributions for each chamber.

- Mean and sigma distributions will give a good approximation of the pedestal value to be subtracted.

- Calculate and store to a data file the pedestal value to be subtracted for each chamber.

(a) Before pedestal subtraction   (b) After pedestal subtraction
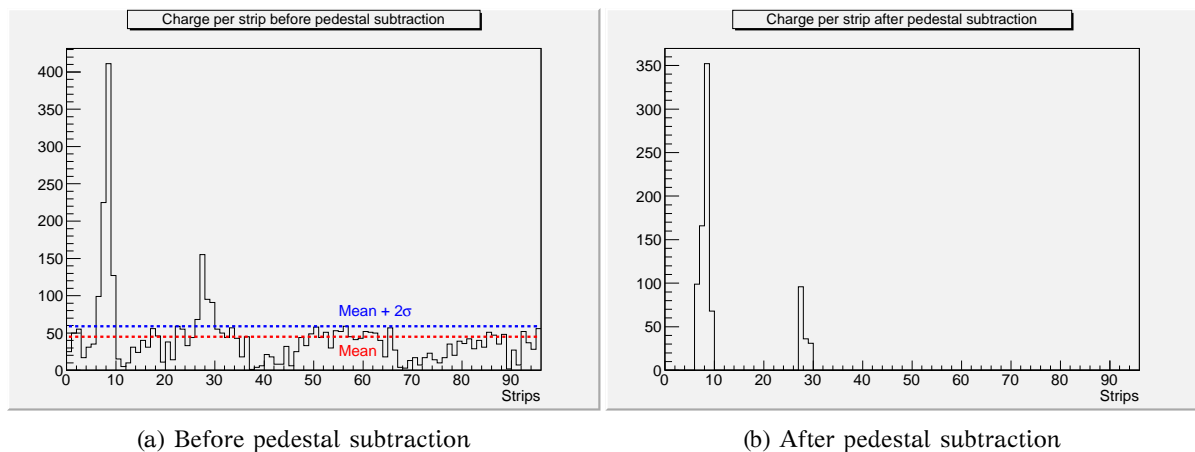
Figure 6.3: A recorded event with two clusters, before (a) and after (b) the pedestal subtraction.

The pedestal position of the channels of each chamber is shown in figure 6.4. The mean and sigma distributions for a telescope station is shown in figure 6.5. As a good approximation for the pedestal value to be subtracted is the mean pedestal position of the channel plus two sigmas. With this subtraction we have an efficient removal of the electronic noise and we are confident that our signal corresponds to the energy deposited by the particles inside the detector.
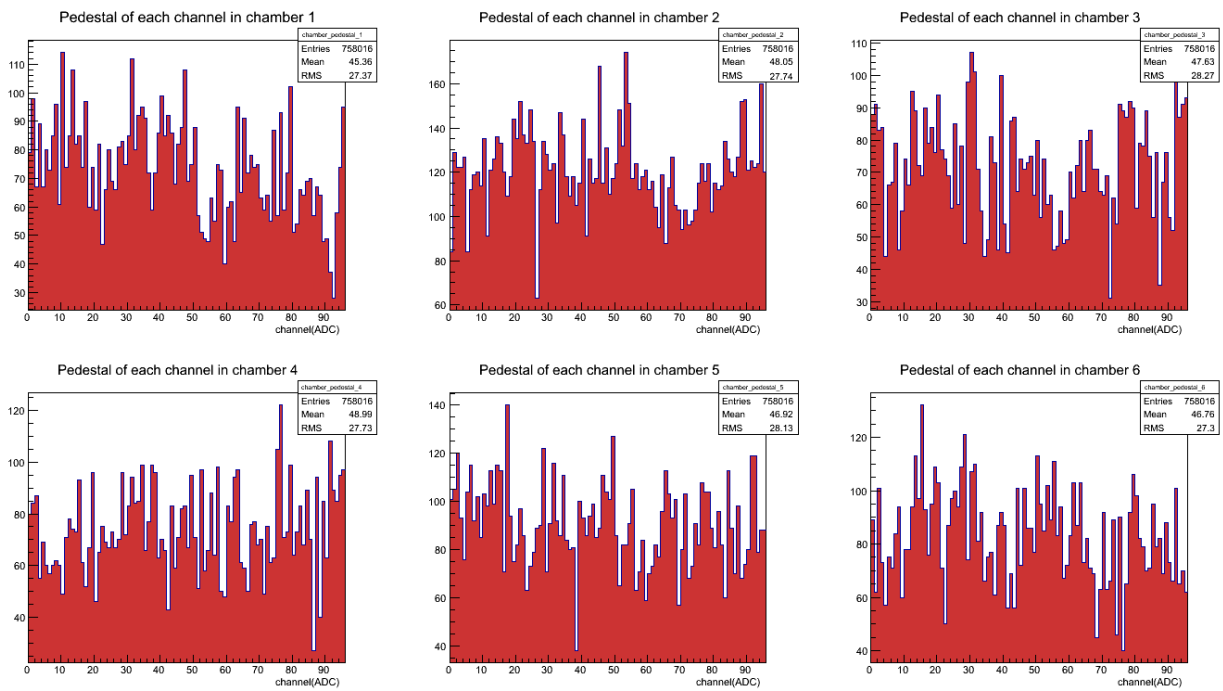
Figure 6.4: Pedestal position distribution for telescope chambers
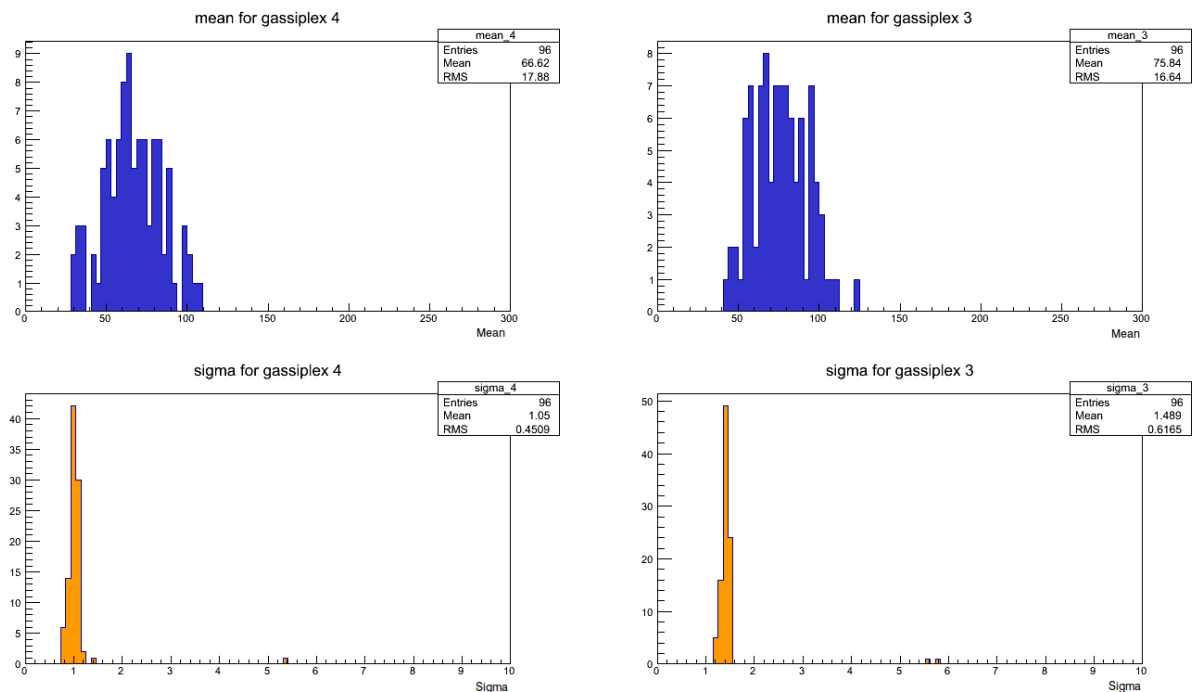
Figure 6.5: Mean and sigma distributions of a telescope station

Last step is to save the values to be subtracted in a data file. Then, we will use this file as an input to the data acquisition program (CENTAURE). This program uses the pedestal file and for every event that is recorded, the pedestal value subtracted and then saved to the data storage.

6.4   Beam profiles

After procedure described in the previous section, we are ready to start the data acquisition for our physics runs (with a particle beam). Assuming that the telescope placed at the right place in order the beam to travel through the active region of our detectors, we expect to record the first events due to the particle's passage through the detector.

The only information we have from the telescope chambers is the charge collected by each strip. Therefore, the first thing we have to do when we reconstruct our events, is to create the charge per strip histograms for single events or hitmaps for all the events of a run. The first step which is of great importance is to find the correspondence of the ADC channels to the gassiplex channels (strips) of the telescope chambers which is the so called *mapping* of the detector. The correct correspondence, shown in figure 6.6 give us the opportunity to reconstruct our first events.
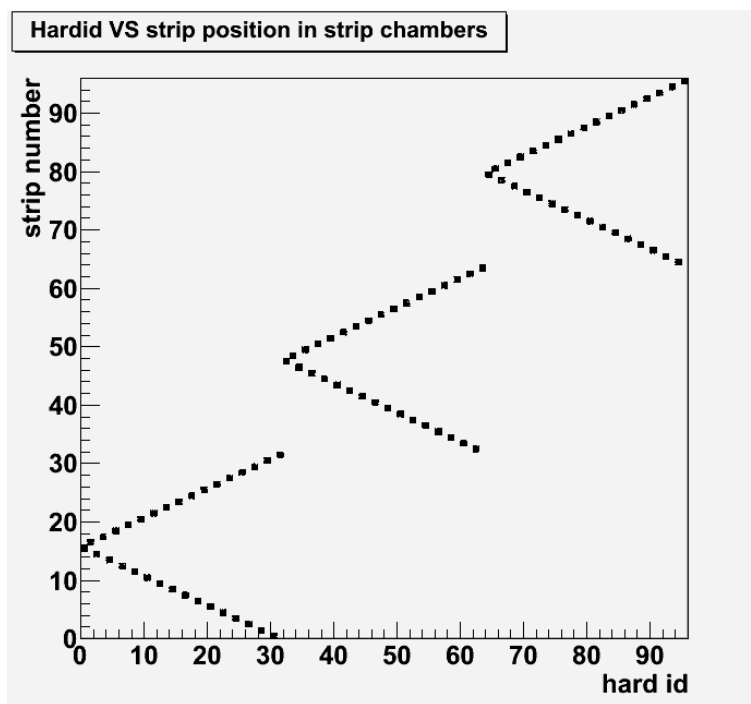
Figure 6.6: Strip number correspondence to ADC channel numbers

As mentioned, during the test beam used two different types of particle beams. The broad muon (6.1(a)) beam covers all the active area of the telescope, so we do not expect to see a clear beam profile at telescope chambers but a uniform distribution. On the other hand, we expect to see a clear profile of the pion beam (6.1(b)) in one direction at least, because it was highly collimated. Figures 6.7 and 6.8 confirm the previous expectations.
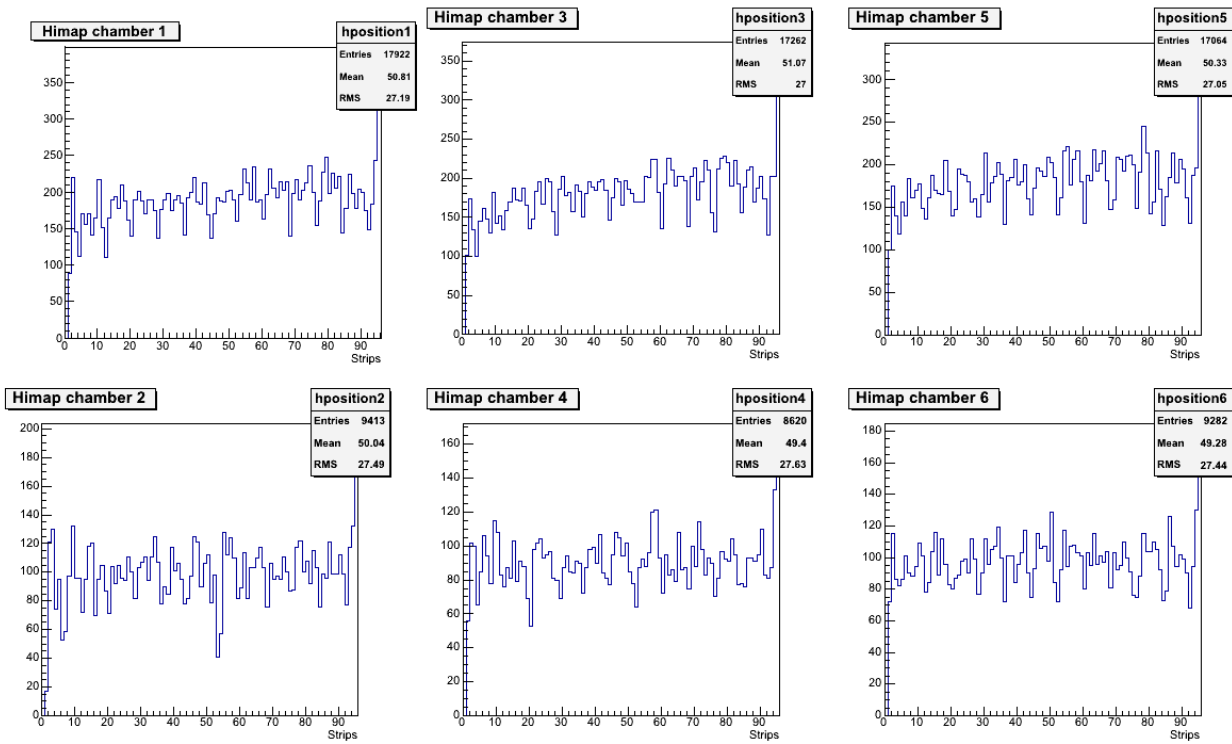
Figure 6.7: Hitmaps of 150 *GeV/c* muons for telescope chambers
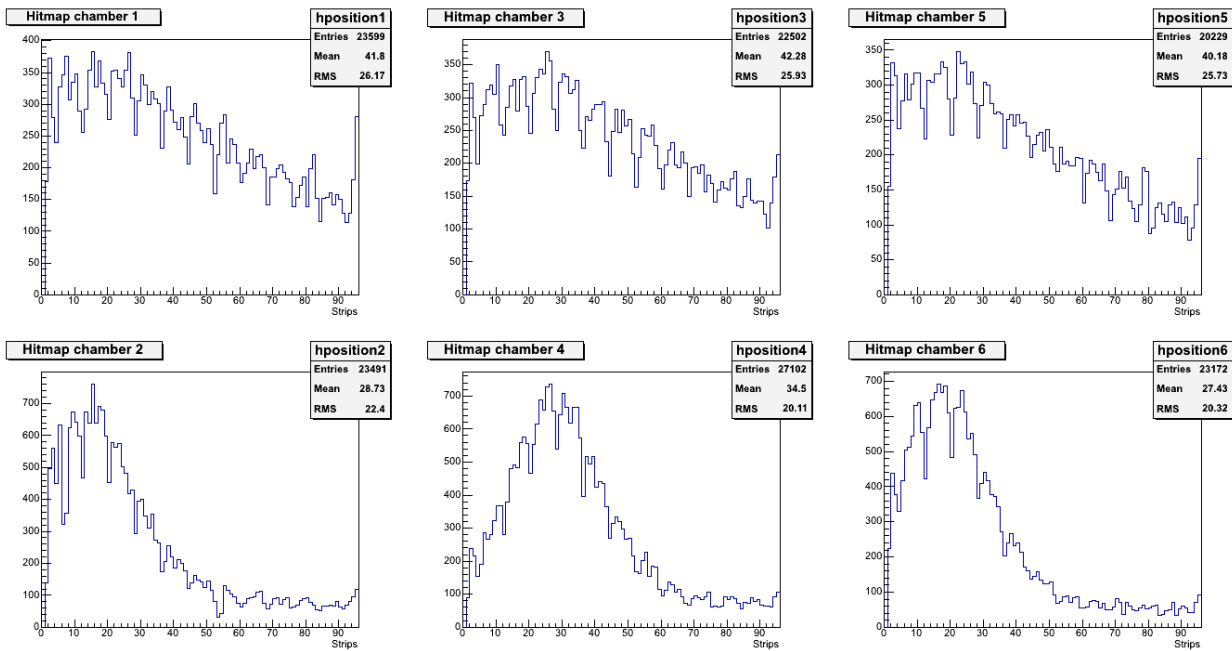
Figure 6.8: Hitmaps of 150 *GeV/c* pions for telescope chambers
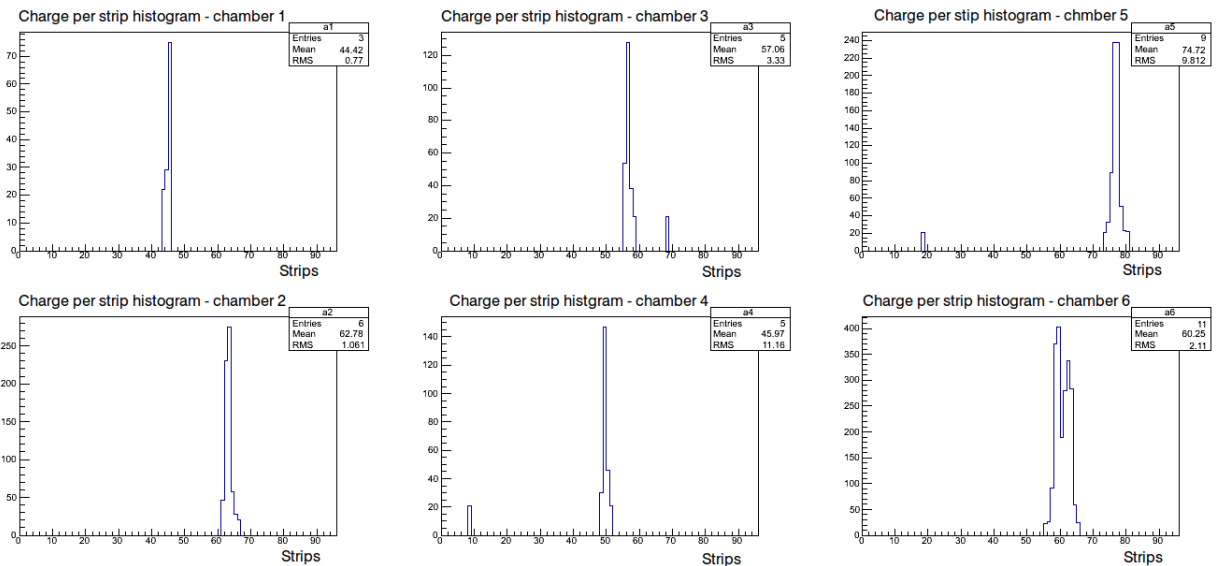
Figure 6.9: One event recorded at the early days of the test beam before the alignment of the telescope. At chamber six(right-bottom) the second peak may indicates a δ-ray

6.5 Clustering algorithm

When a particle passes through the detector, primary electrons are created due to the ionisation and the presence of the electric field makes them move to the the anode. In a micromegas detector primary electrons are created to the drift gap and drift to the amplification gap. With the correct field ratio between the drift and amplification gap, the detector becomes transparent and all the electrons enter the amplification gap, where the avalanche multiplication occurs and the charge is deposited to the strips.

In most of the cases, the size of the avalanche is larger than the size of the strips and as a result, the charge is distributed to more than one strips, creating compact teams of "fired" strips, known as clusters. Clusters, hold all the important information about the particle that crossed the detector. Consequently, an algorithm in order to find the clusters and calculate their properties is a high priority issue.

One of the most challenging parts of this thesis was the development of the clustering algorithm in order to provide with an efficient way the cluster properties. The algorithm that developed provides information about the number of cluster created in the detector, the exact position and size of each cluster in strips units[2] and the total charge of each cluster.

The method that is used in the clustering algorithm for a simple event is described below:

- Create charge per strip histogram of each event with a cut on the ADC value. With this way, we avoid to sort the strips in the correct order and we can take a first look at the event.

- Search for peaks in the histogram that indicate the maximum of each clusters.

- Go to the highest peak and then search left in order to find the start of the cluster and right for the end of the cluster. In order to find a start (or end) of a cluster, required two

---

[2]1 strip unit = 250 μm.

strips with zero content after the last strip of non-zero content[3].

- Knowing the cluster start and the cluster end from the previous step, calculate the strip size and loop over the fired strips i order to calculate the cluster position and the cluster energy. The cluster position x of a cluster of size N is calculated using the weighted mean of the strip positions x_i with respect to their charge Q_i:

$$x = \frac{\sum_{i=1}^{N} x_i \cdot Q_i}{\sum_{i=1}^{N} Q_i}$$

- Continue to the second higher top if exists and follow the same procedure. Continue to third etc.
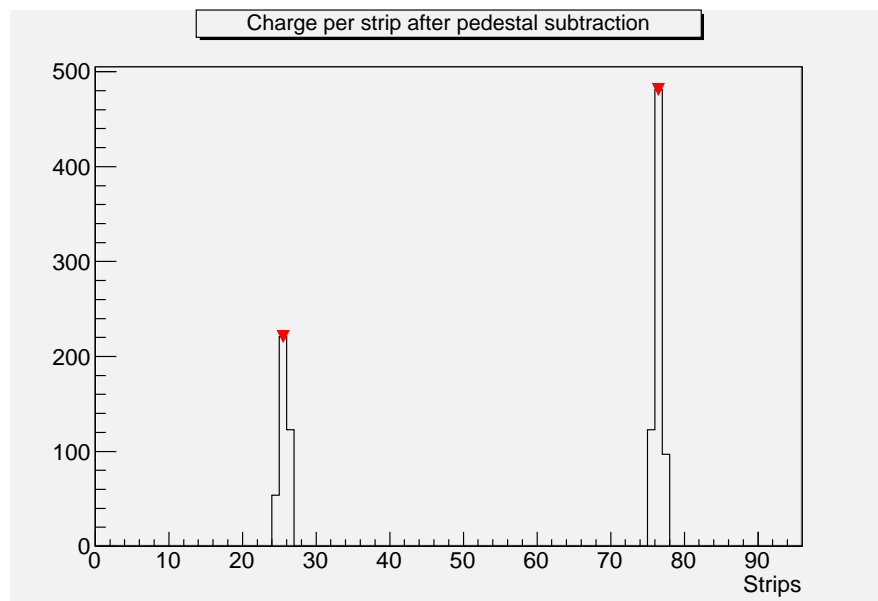
Figure 6.10: An event with two clusters. The algorithm start with the peak of the cluster at the right and calculate the properties. Then the second cluster follows

(a)   (b)

Figure 6.11: (a) Output of the algorithm for the cluster on the right of the previous figure. (b) Output of the algorithm for the cluster on the left of the previous figure.

Applying the algorithm for all the event of a run we can take the next figures that present the cluster properties for runs with muon and pion beams.

---

[3]For the cases we have cluster conflicts there are extra criteria in order to separate the cluster start and the cluster end.
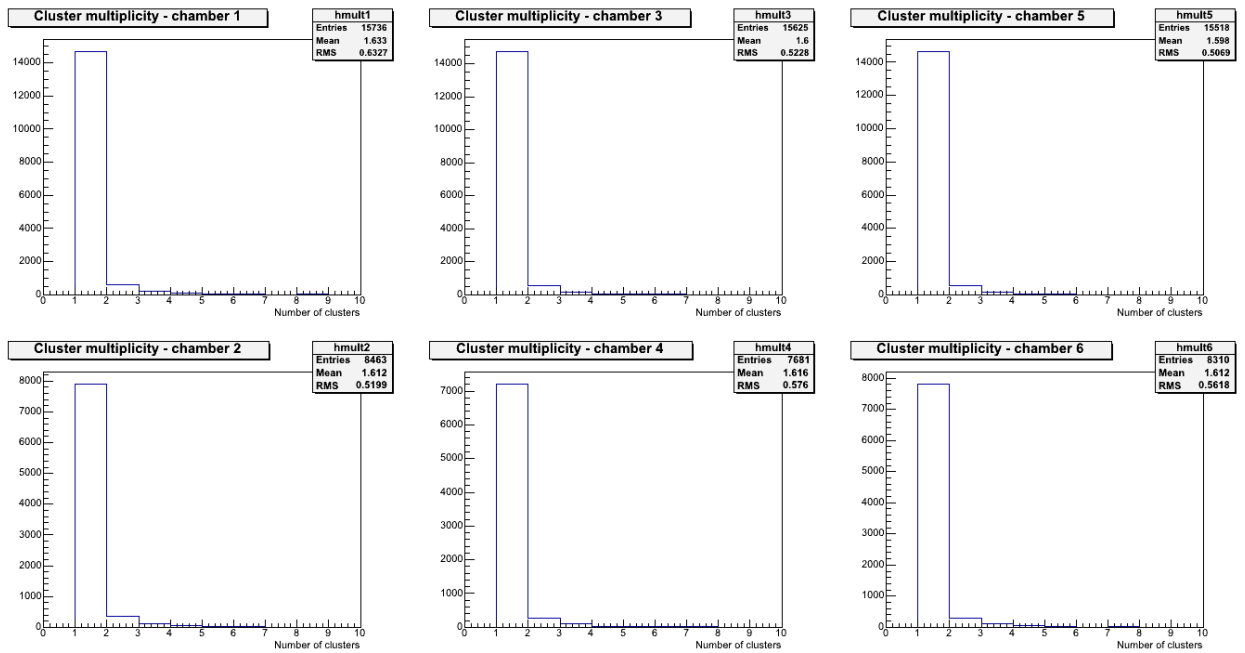
Figure 6.12: Cluster multiplicity of telescope chamber for a run with muon beam
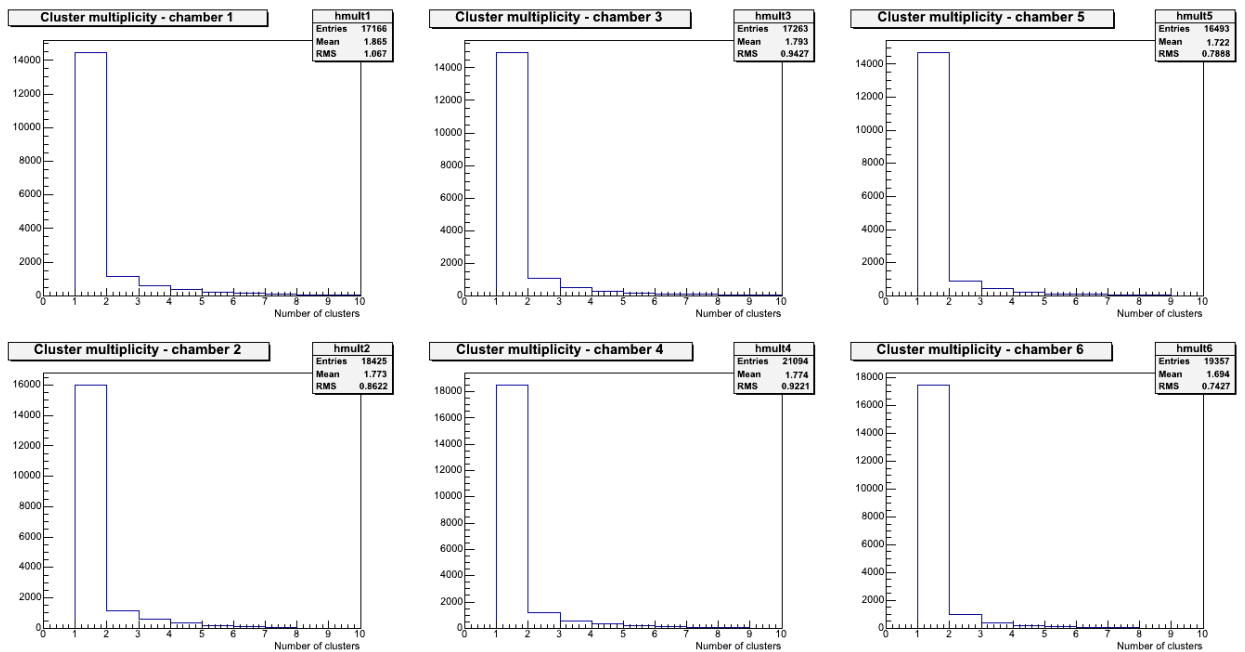
Figure 6.13: Cluster multiplicity of telescope chamber for a run with pion beam
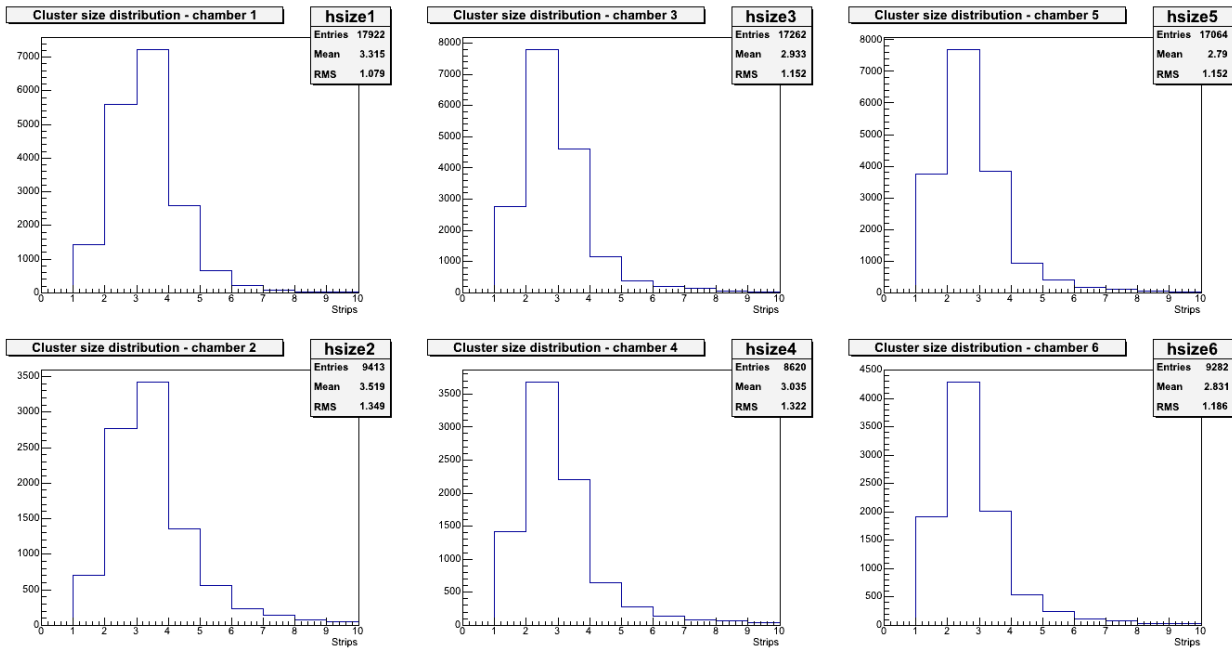
Figure 6.14: Cluster size distribution of telescope chambers for a run with a muon beam
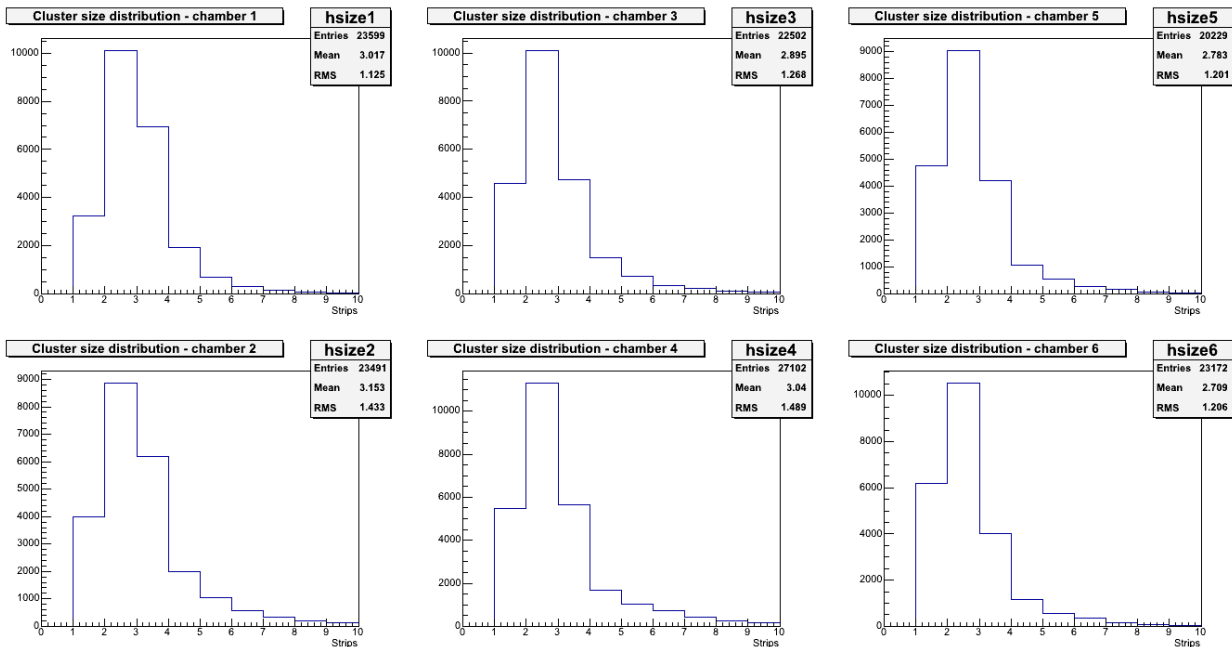
Figure 6.15: Cluster size distribution of telescope chambers for a run with a pion beam
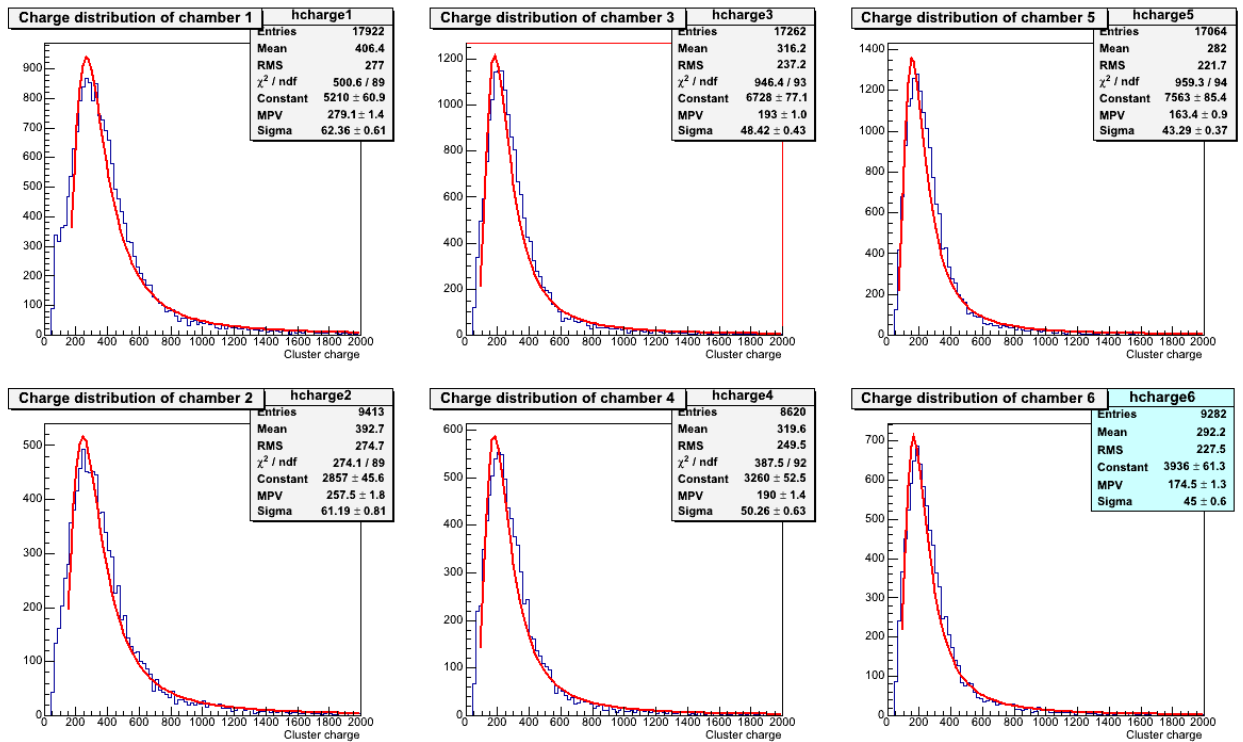
Figure 6.16: Cluster charge distribution of telescope chambers, fitted with a landau curve for a run with a muon beam
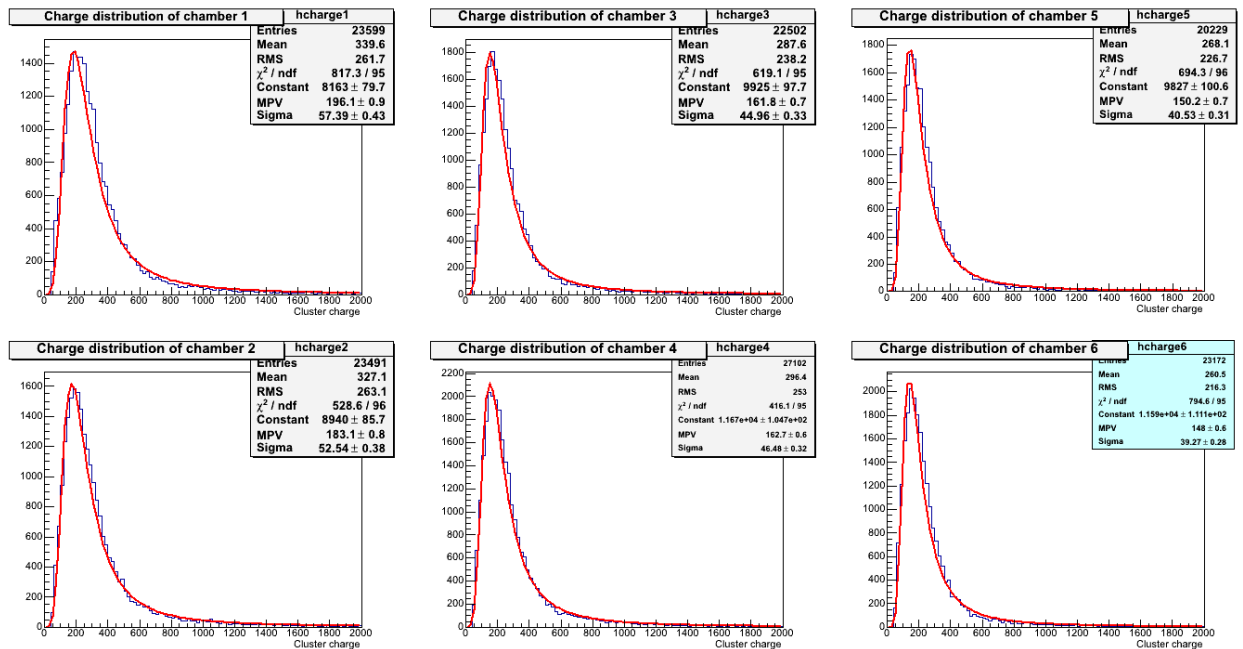
Figure 6.17: Cluster charge distribution of telescope chambers, fitted with a landau curve for a run with a pion beam

6.6   Telescope alignment

After the calculation of cluster properties, we are able to determine particle tracks with the telescope. The stations are supported in mechanical structure that keeps them parallel and movable. However, many reasons exist to explain the misalignment of the stations caused during the transportation and the installation of the setup to the testbeam area. Therefore, we have to correct out data in order to align the telescope station each other and perform the tracking.

We correct the misalignment following the next process:

- Keep station one as reference frame.
- Search for single cluster events for X and Y planes.
- Calculate cluster position difference between:
  - ▶ 2nd Station - 1st Station.
  - ▶ 3rd Station - 1st Station
- Fill a histogram with the differences and fit a Gaussian.
- The mean value given by Gaussian fit is the misalignment of the station.

This process revealed the misalignments shown in the next table:

Table 6.1: Misalignment of 2nd and 3rd station when 1st kept as refernce frame.

Station	Misalignment [strips]	Misalignment [mm]
2nd X-plane	-1.996	-0.499
2nd Y-plane	-12.34	-3.085
3rd X-plane	+2.857	+0.714
3rd Y-plane	-1.307	-0.326

In figure **??** can be found the distributions of cluster position differences before and after the the alignment.
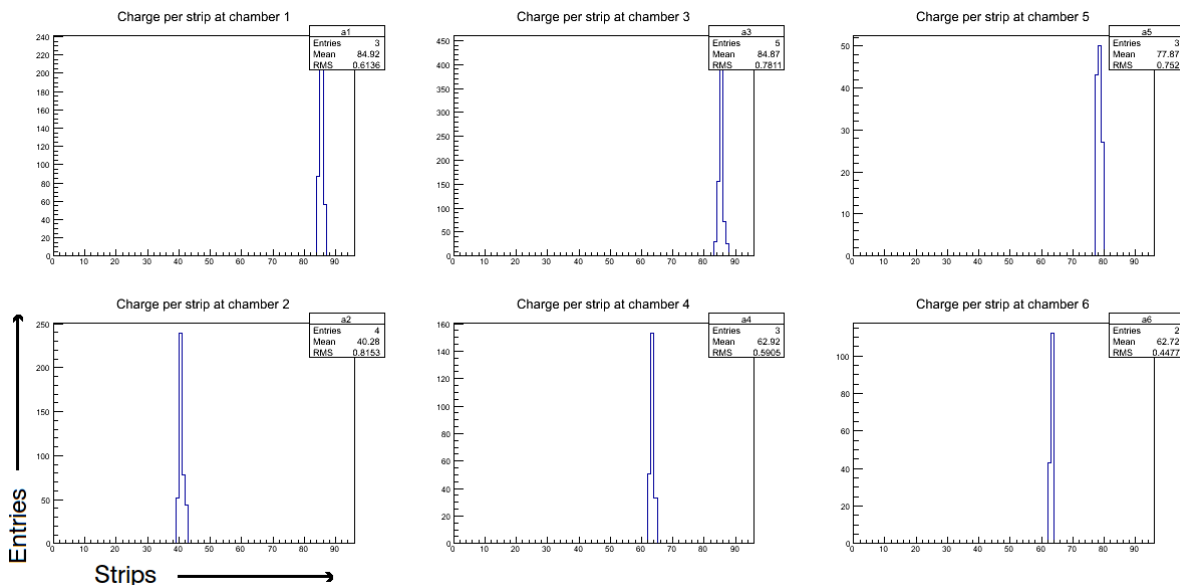
Figure 6.18: A single cluster event
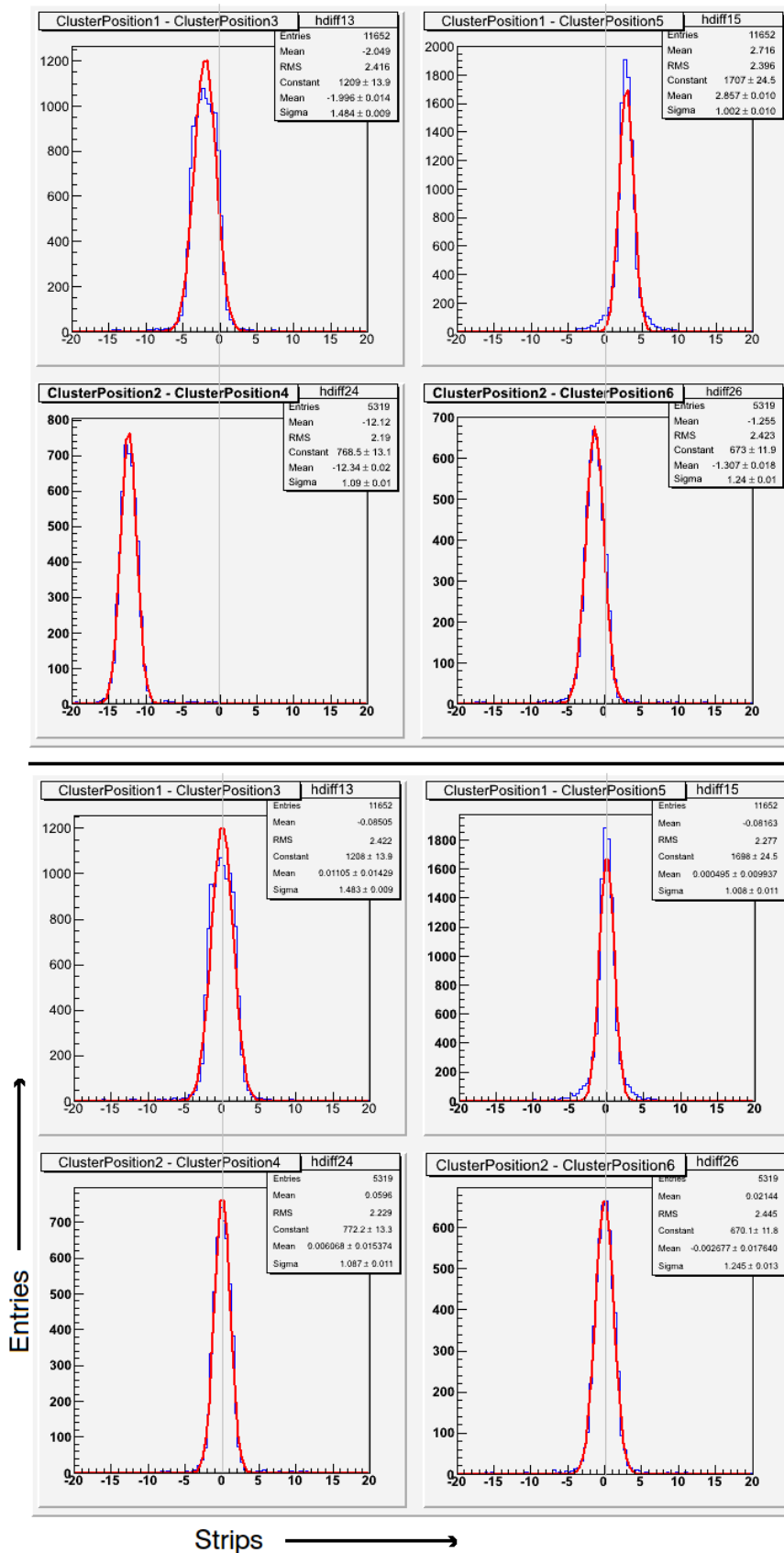
Figure 6.19: Distribution of the cluster position differences when the first station kept as reference frame before (top) and after (bottom) the alignment.

6.7   Track detection

For the tracking, used the RD51 tracking algorithm[4]. The algorithm is suitable both for micromegas and GEM telescopes and is based on Hough transform for line detection. The user has to provide as input a rootfile containing the number of clusters and their position. On the other hand, the output is a rootfile containing all the information needed for the projection of the tracks at X and Y plane.

6.7.1   Basic concept of tracking

For single cluster events (events with one cluster per detector) a total of three points in space (one per station) were taken, creating a unique track. To make the approach of tracking more trivial, each point from the 3D space (X-Y-Z) is projected to the 2D X-Z and Y-Z plane, see figure 6.20. After this, instead of facing a three dimensional tracking problem the problem transformed to a two dimensional, where more trivial approaches and faster algorithms exist. The study of the tracker and the tracking algorithms can then be separated in two phases. Phase one, tracking in X projection (X-Z plane) and phase two, tracking in Y projection (Y-Z plane), where the Z axis of the tracker will be treated as X axis for the algorithm at both projections. That is done because at that direction the tracker has fixed positions of the stations.

For example, take under study the X-Z projection plane of the real track; the Z of the real track corresponds to the position of the station and that information will be represented and treated as abscissa (on X axis) for the working X-Y space of the algorithm. The information extracted from the detectors (X position of the real track in X-Y-Z space) will be treated as ordinate (on Y axis) from the algorithm.
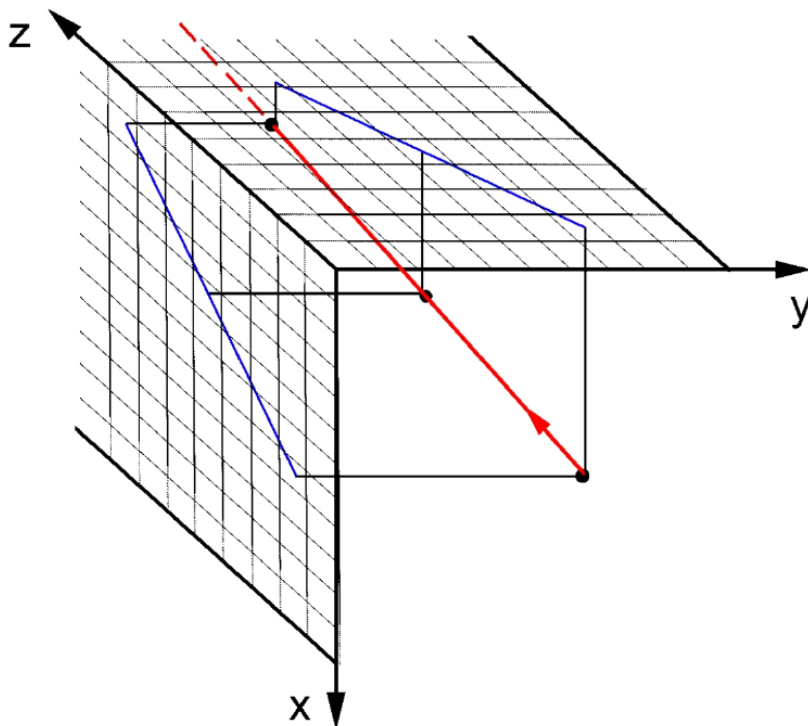
Figure 6.20: Projection of points and line for the space (3D) XYZ in two planes (2D), X-Z and Y-Z.

---

[4]Developed by K.Karakostas.
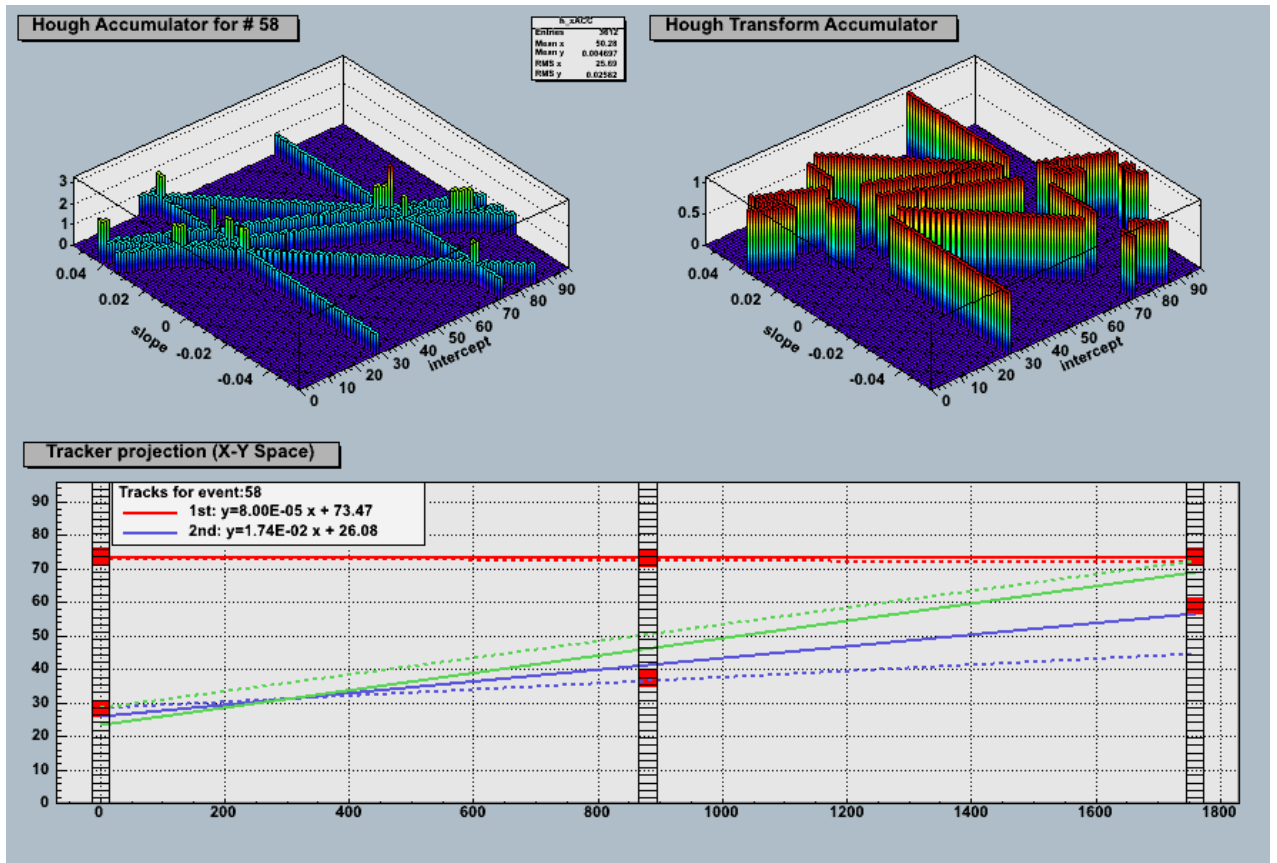
Figure 6.21: Off-line dispay of an event with two tracks
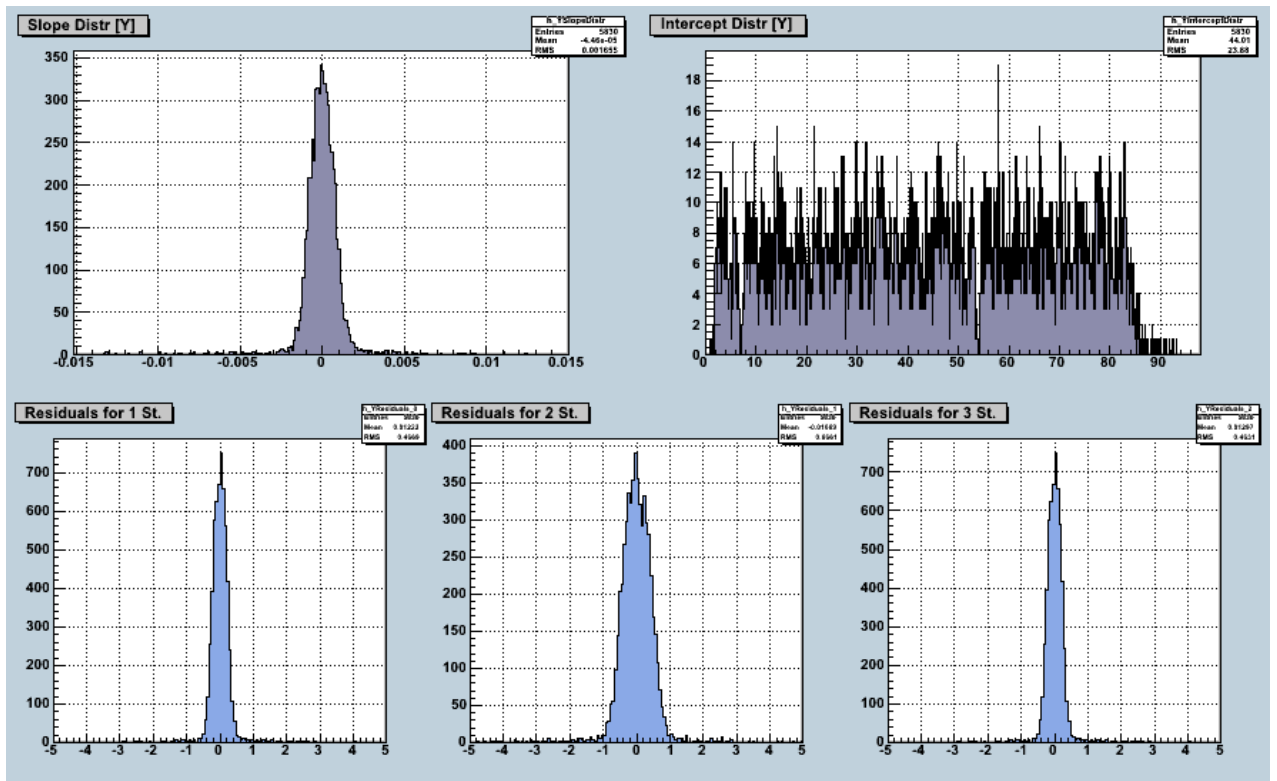
Figure 6.22: Track statistics after the

6.8　Spatial resolution of the telescope stations

As long as we know the track parameters, we can measure the spatial resolution of each station of the telescope. In order to measure the intrinsic resolution we have to calculate the residuals. The method that used was:

- Choose events with one track both in X and Y planes and one cluster per chamber

- Calculate the residuals one for all the stations, which is the difference of cluster position from the position given from the track (fig. 6.23(a)). This distribution gives the $\sigma_{included}$

- Calculate the residuals this time excluding the station under study. Suppose that we want to study chambers 1,3,5 (X-tracks), especially chamber 5. Then, exclude chamber 5 and fit a straight line using the cluster position of chambers 1,3. Calculate the residuals which is the difference of the cluster position from the position given from the straight line fit (fig. 6.23(b)). This distribution gives the $\sigma_{excluded}$

(a)　　　　　　　　　　　　　　　　　　　(b)
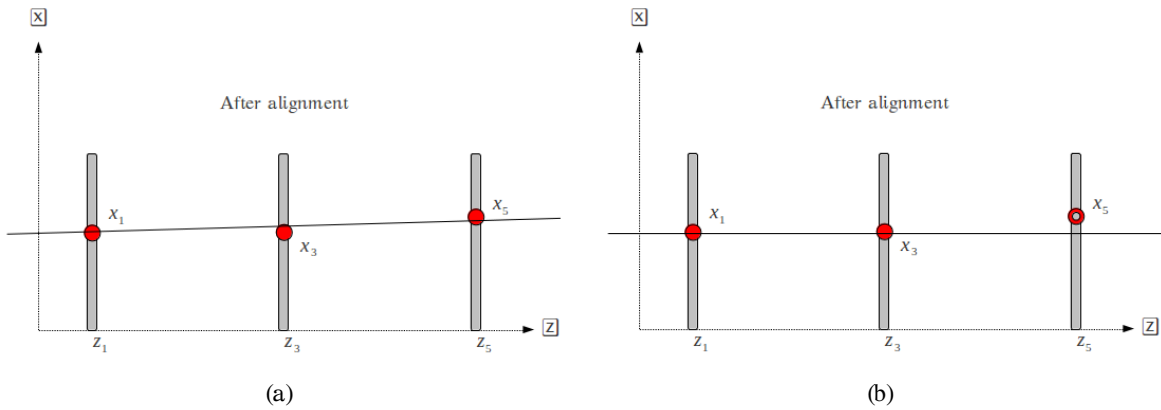
Figure 6.23: Illustration of the method that used in order to calculate the intrinsic resolution of each chamber. In (a) all the station included in the calculation, while in (b) the station under study is excluded.

The intrinsic resolution of each chamber is given by the geometrical mean of the internal and external σ calculated from the distribution of the residuals.

$$\sigma_{total} = \sqrt{\sigma_{included} \cdot \sigma_{excluded}} \tag{6.1}$$

The residuals distribution The intrinsic resolution for each telescope chamber that this study revealed ca be found in the next table

Table 6.2: Intrinsic spatial resolution of telescope chambers

chamber	$\sigma_{included}[strip]$	$\sigma_{excluded}[strip]$	$\sigma_{total}[strip]$	$\sigma_{total}[\mu m]$
1	0.116955	0.655224	0.278928	69.73
2	0.106858	0.59539	0.252234	63.06
3	0.225735	0.336798	0.275730	68.93
4	0.205426	0.588961	0.347833	86.95
5	0.116955	0.665224	0.278928	69.73
6	0.106858	0.59539	0.252234	63.06

Figure 6.24: Residual's distributions for telescope chambers calculated including and excluding the station under study.

6.9   The spatial resolution of the tracker

In order to calculate the spatial resolution of the telescope we use events with one cluster per station. An unbiased method to calculate the resolution, is to use the basics geometry and especially the theorem of similar triangles. If we apply the theorem for our telescope geometry (6.25) both in X and Y plane we have:

$$\frac{x_3 - x_1}{x_5 - x_3} = \frac{z_3 - z_1}{z_5 - z_3} = \frac{880}{880}(= c)$$

$$\Rightarrow c \cdot x_5 - c \cdot x_3 = x_3 - x_1$$

$$\Rightarrow \boxed{f_{tel} = (c + 1) \cdot x_3 - x_1 - c \cdot y_5} \tag{6.2}$$
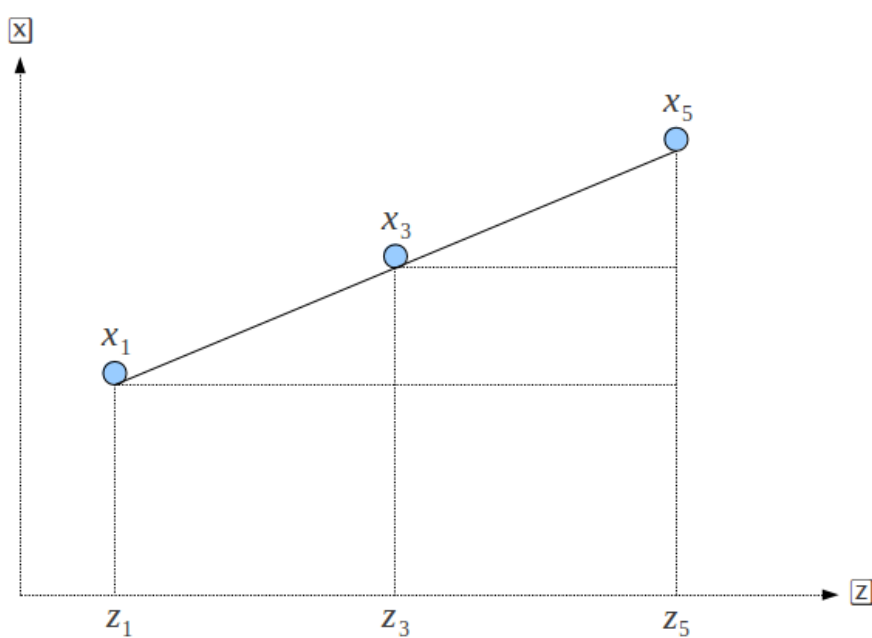
Figure 6.25: Schematic of the basic geometry used in the calculation of tracker resolution

Using the propagation of errors the calculation of the resolution of the tracker, based on the sigma of the function created before (f_{tel}), is:

$$\sigma_x = \frac{\sigma_{f_{tel}}}{\sqrt{(c + 1)^2 + c^2 + 1}}$$

The sigma of the distribution derives the resolution of the tracker:

$$\sigma_x = 67.89 \mu m$$

$$\sigma_y = 60.78 \mu m$$

The distributions of f_{tel} for the X and Y plane can be found at figure 6.26.
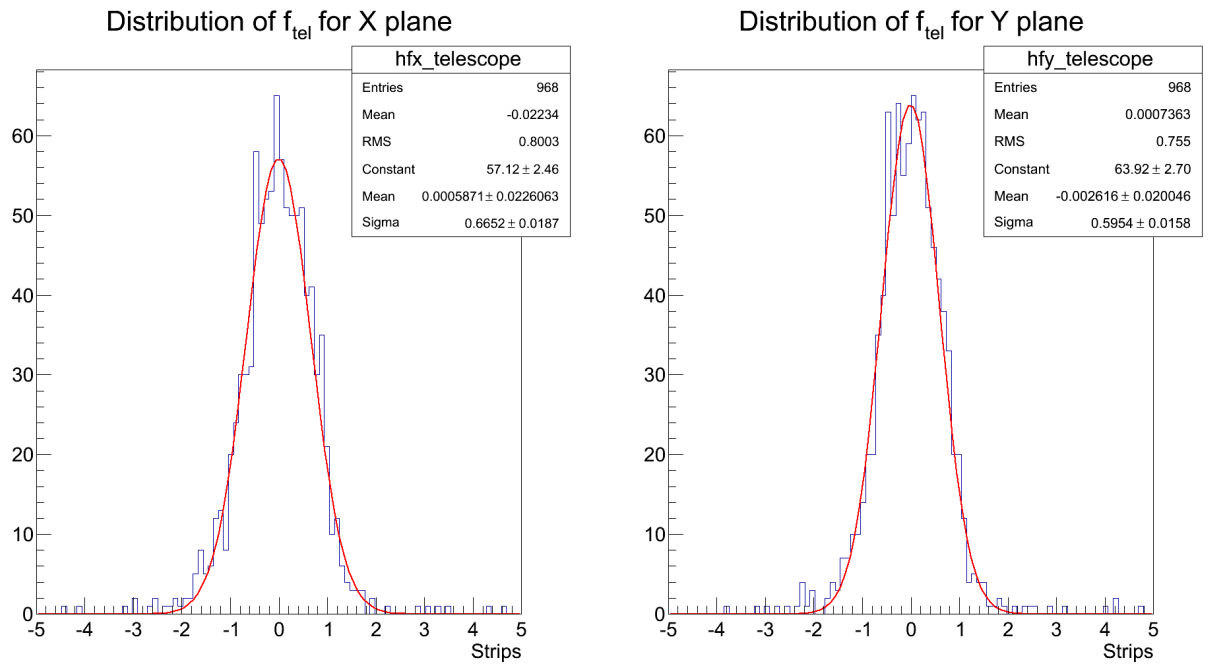
Figure 6.26: Distrifution of function f_{tel}, that used for the calculation of spatial resolution, for the single cluster events.

7

Square meter prototype performance

7.1 Introduction

This section is dedicated to efficiency and multiplicity studies for the square meter prototype. For these studies, we use events with one track in X or Y plane and then extrapolate its impact to the prototype and check if the prototype is efficient or not.

In order to support the analysis for the micromegas sDHCAL a new class added to the framework by the linear collider group of LAPP, the CaloEvent class. The main purpose of this is to describe the events of the calorimeter and suppress the noise hits. The basic variable is the number of hits at the calorimeter which are classified relatively with respect to the type of the particle, the track parameters, the track extrapolated position to the calorimeter, the timing information and the environmental conditions like pressure or temperature.

Therefore, the first task about the efficiency studies was to implement the track parameters to the framework and write some scripts in order to use the track parameters in the CaloEvent class. The implementation of the tracks in the CaloEvent class, make things better, because an event of the class contains all the information both for the telescope and the prototype.

7.2 Pedestal calibration of the prototype.

The aim of the calibration is to verify the overall functionality of the chips (shaper gain, noise) and determine optimal settings (thresholds and pedestal offsets) for maximum efficiency and negligible noise hit rate. This procedure was carried out for each MICROROC chip of the six ASUs. A LabView program developed at LAPP allowed the control of the injection of calibrated pulses into the chip entry stage and to control the chip configuration.

S-curves

The shaper gain of a given channel is determined by injecting voltage pulses to the test capacitor for decreasing threshold values. The obtained hits versus threshold trend is called an S-curve because of its specific shape showing a higher level plateau and a lower level one linked together by a continuous slope (recalling the shape of the letter 's'). Measuring the S-curve inflexion point (in DAC units) for different input charges (in fC) yields the gain of the shaper (in DAC/fC).

The pedestal of a channel is defined as the inflection point abscissa of its S-curves and the electronic noise of a channel is rendered by the width of its S-curve.

Calibration procedure

Given that 1 DAC corresponds roughly to 1 fC, figure 7.1(a) shows that the pedestals are quite spread and present irregular widths. The calibration process is aimed at allowing the lowest possible threshold with the lowest possible electronic noise contamination in order to achieve the highest efficiency. The tunable parameters are the gain of each channel and the global chip threshold. It has been noticed in that the pedestal value is linearly dependent on the channel gain and that the S-curve width on the contrary does not change much for different gains. Therefore it has been possible to align the S-curve at lower levels so that they all start at the same Digital to Analog Count (DAC) value; the result is plotted in figure 7.1(b). This technique allows the threshold for each readout channel to be minimized but is disadvantaged by the spread of channel gains.

(a)   (b)
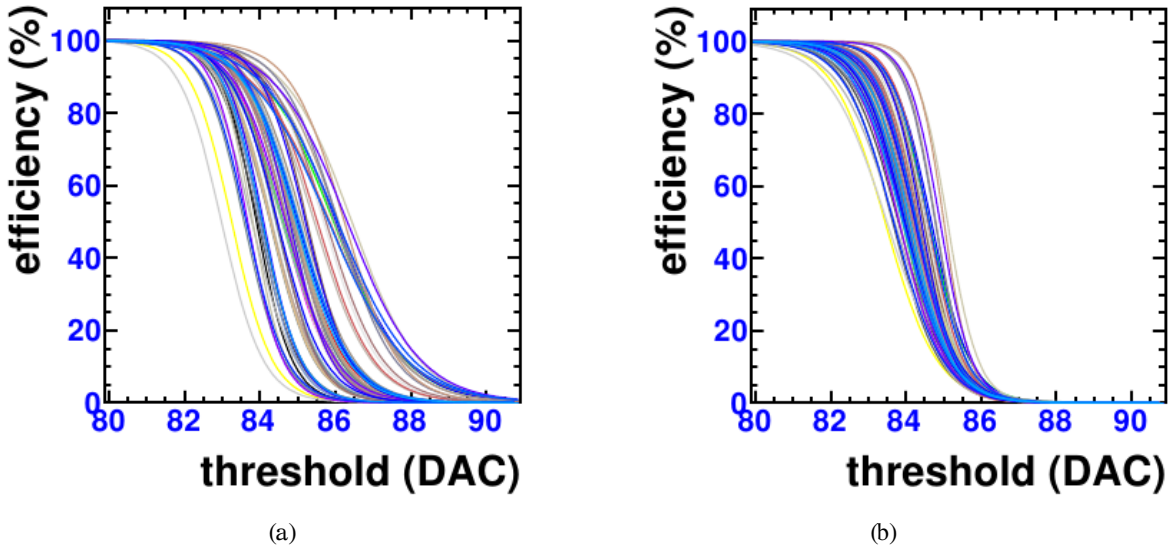
Figure 7.1: Pedestal S-curves for a chip before (a) and after (b) calibration

7.3   Event timing

The large size of the prototype in addition with the 9216 channels, indicates that we have to define an efficient method to synchronize our events. A good understanding of the event's timing, give us the opportunity to apply a time cut in order to separate the real hits, from the noisy hits.

The timing of each event calculated with the next values:

$$t_{hit} = t_{read} - t_2 + t_3$$

$$\Rightarrow dt = t_2 - t_3$$

and

$$t_{read} = t_0 + (t_1 - t_1(0))$$

where

- t_0 is the unix timestamp measured in (32 bits, with or without milliseconds)

- t_1 is absolute BCID (bcId-Abs, 48-bit).

- $t_1(0)$ is first t_1 reading.

- t_2 is the BCID of the DIF trigger time counter (24 bits).

- t_3 is the BCID of the recorded hit(HRs)

The DIF trigger time counter BCID synchronized with that of the hit, allow to find precisely the moment the particle is spent in data HR. In order to do this we calculate the time to readout distribution and the we apply the time cut based on this distribution. A typical time to readout distribution can be found in the next figure.
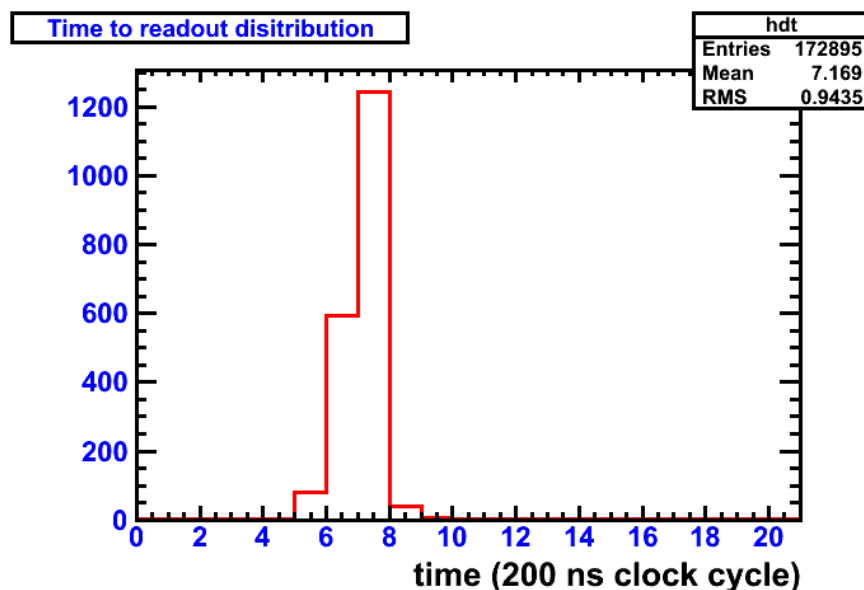
Figure 7.2: A time to readout distribution that used to apply the time cut

7.4 The efficiency measurement

The efficiency studies performed with muons (150 GeV/c), as they are a good approximation of MIP which liberate on average 30 primary electrons in the drift region. The most probable value is actually 14 electrons which are multiplied in the amplification gap by factors up to 10^4 depending on the mesh voltage.

In order to measure the efficiency of the square meter prototype, the tracks reconstructed from the tracker were used. A sample of "golden" events was selected by requesting three single cluster events (both in X and Y plane) in the three telescope stations in order to define a particle track. A time cut requiring $6 < dt \leq 8$ was applied for the prototype events, aiming to completely avoid taking noise hits into account. In figure 7.3 can be found the 2D muon beam profile at the prototype when a time-cut is applied (on the right) and without time-cut(on the left).In each processed event, the track impact extrapolated to the prototype and a hit has been searched in an area created by the pad in which the track is pointing ±3 pads.
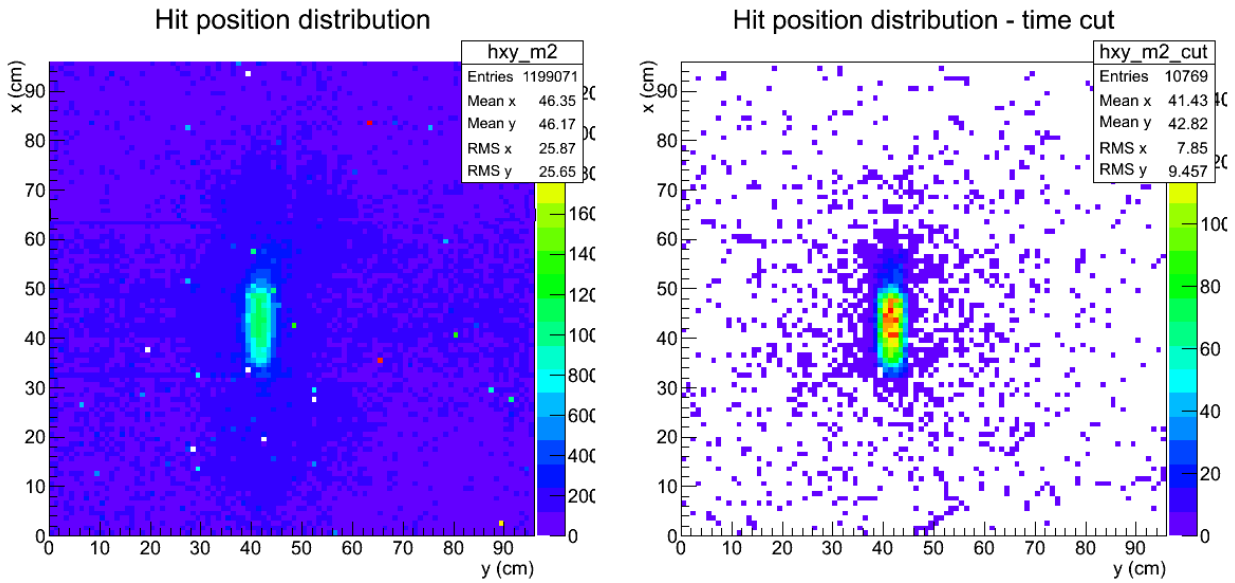
Figure 7.3: Beam profile of 150 *GeV/c* muons at the prototype

If a hit existed in this area of the telescope then the prototype is efficient for this event, while the prototype in not considered as efficient if a hit does not exist in the specified area. An illustration of an efficient and an inefficient event is shown in figures 7.4(a) and 7.4(b) respectively. The ratio of the number of events where the prototype is efficient to the events total number of the events of the sample is the efficiency of the chamber.
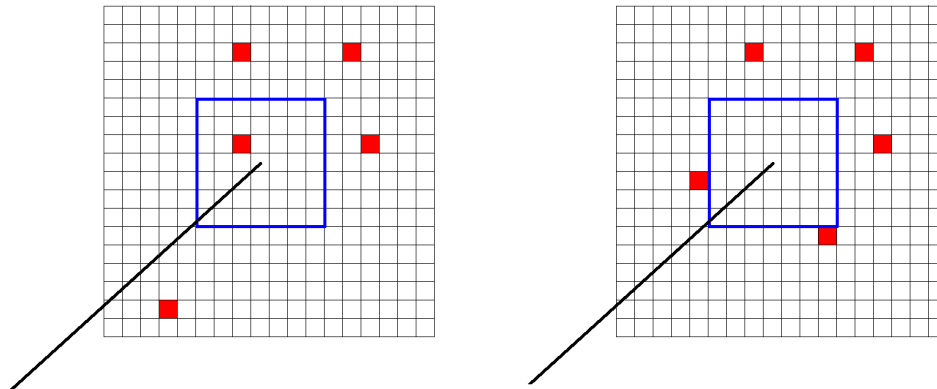
(a) An event which is considered as efficient   (b) An event which is considered as inefficient

Figure 7.4: Illustration of the criteria applied in order to define if an event was efficient (a) or inefficient (b).

The error $\delta\epsilon$ on the efficiency is calculated through the formula follows by the binomial distribution:

$$\delta\epsilon = \sqrt{\frac{\epsilon \cdot (1 - \epsilon)}{N_{total}}}$$

where ϵ is the efficiency and N_{total} is the number of total events of the golden event sample created for the efficiency measurement.

7.4.1 Voltage scans

As mentioned before the efficiency has a strong dependence on the applied voltage to mesh. Efficiency was measured at various mesh voltages and drift fields, for several shaping times with the beam spreading over roughly hundred pads. The analysis leads to the trends showed in the next figures where a high efficiency is reached at all shaping settings. At 390 V mesh voltage (gas gain around 3000), 1 fC hit threshold and 200 ns shaping, one records an efficiency of 99 % while these efficiencies are reached with a drift field higher than 100 V/cm.

(a) Efficiency versus mesh voltage for X plane

(b) Efficiency versus mesh voltage for Y plane
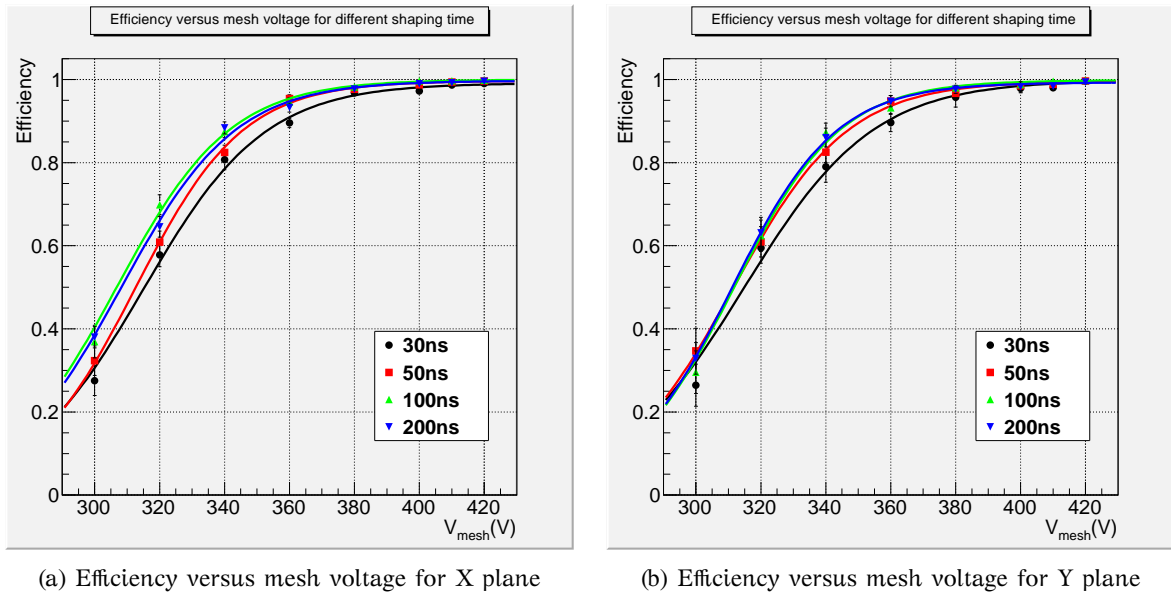
Figure 7.5: Mesh voltage scan for various shaping times.

(a) Efficiency versus drift field for X plane

(b) Efficiency versus drift field for Y plane
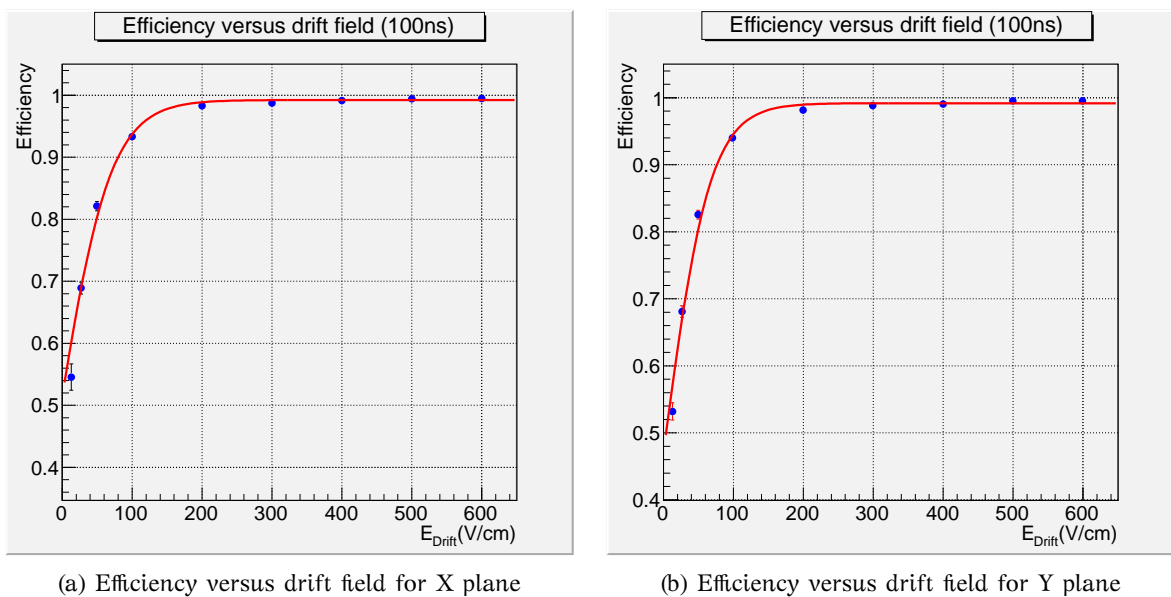
Figure 7.6: Drift field scan.

7.4.2 Threshold scan

In a digital hadronic calorimeter, the threshold is a fundamental parameter. Varying the threshold from 1 fC which is the lowest running threshold to 40 fC. An increase to 2 fC leads to a dramatic drop of the noise rate by 3 orders of magnitude while leaving the efficiency almost unchanged, while a further increase results to a steep drop of efficiency. A maximum efficiency above 98% is reached at a threshold as low as 4 fC. The efficiency is about 70% at a threshold of 20 fC and drops at 40% for threshold of 40 fC. The slight inflexion point at half of the range follows from the Landau distribution turnover.

(a) Efficiency versus threshold for X plane   (b) Efficiency versus threshold for Y plane
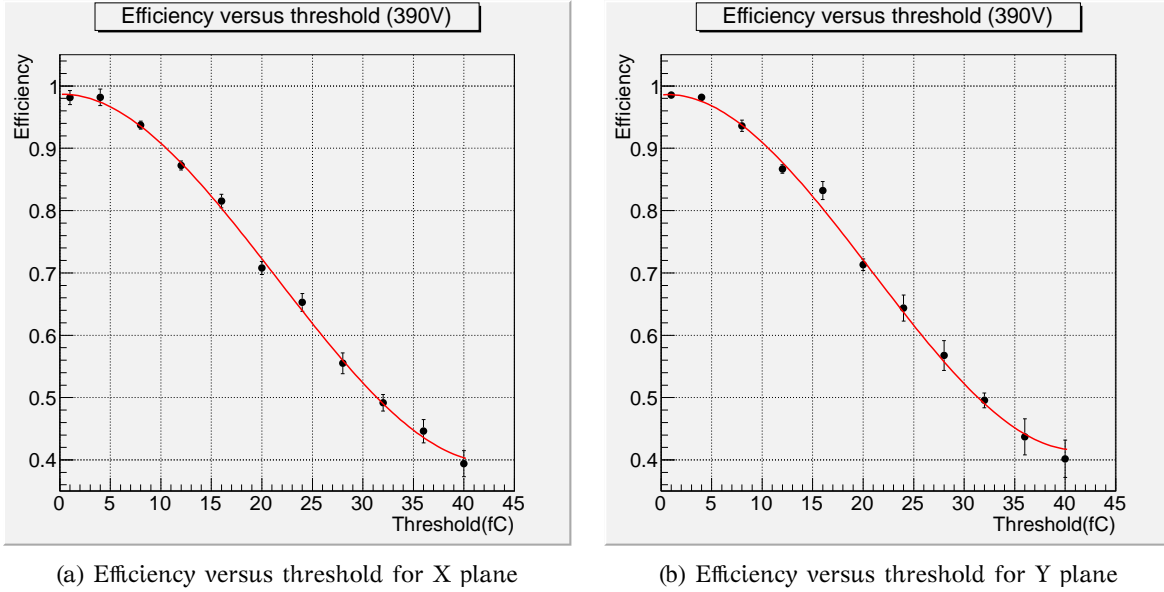
Figure 7.7: Threshold scan.

7.5 Multiplicity measurement

In order to perform the multiplicity study, the same sample of golden events has been used, as for efficiency measurement. For each event, the number of hits exist in the ±3 pad area around the pad expected to be hit by the particle track extrapolation has been counted. The average value of this number over all the processed events is the multiplicity of the chamber. It can be formulated through:

$$multiplicity = \frac{1}{N_{total}} \sum_{i=1}^{N_{max}} i \cdot N_i$$

where N_{tot} is the number of processed events, N_{max} is the maximum multiplicity in the search area, N_i is the number of events which showed a multiplicity of i.

7.5.1 Voltage scan

A benefit of Micromegas technology is the limited spatial extension of the avalanche signals. This is a result of the little diffusion experienced by the electrons in the gas. A cloud of primary electrons liberated at the cathode arrives at the mesh with a lower transverse spread compared to others. It is therefore likely that all electrons from a traversing particle are collected on one pad. The hit multiplicity lies below 1.2 up to a mesh voltage 380 - 390 V (i.e. gain of 3000). At higher gas gain, neighboring pads become sensitive to single electrons, increasing the multiplicity. There is however no reason to work in that regime as high efficiency is reached at lower gains. The multiplicity measurement performed for the same voltage, drift field and shaping time settings, as the efficiency measurement. The results shown in figures 7.8(a), 7.8(b) and 7.9(a),7.9(b)

(a) Hit multiplicity versus mesh voltage for X plane

(b) Hit multiplicity versus mesh voltage for Y plane
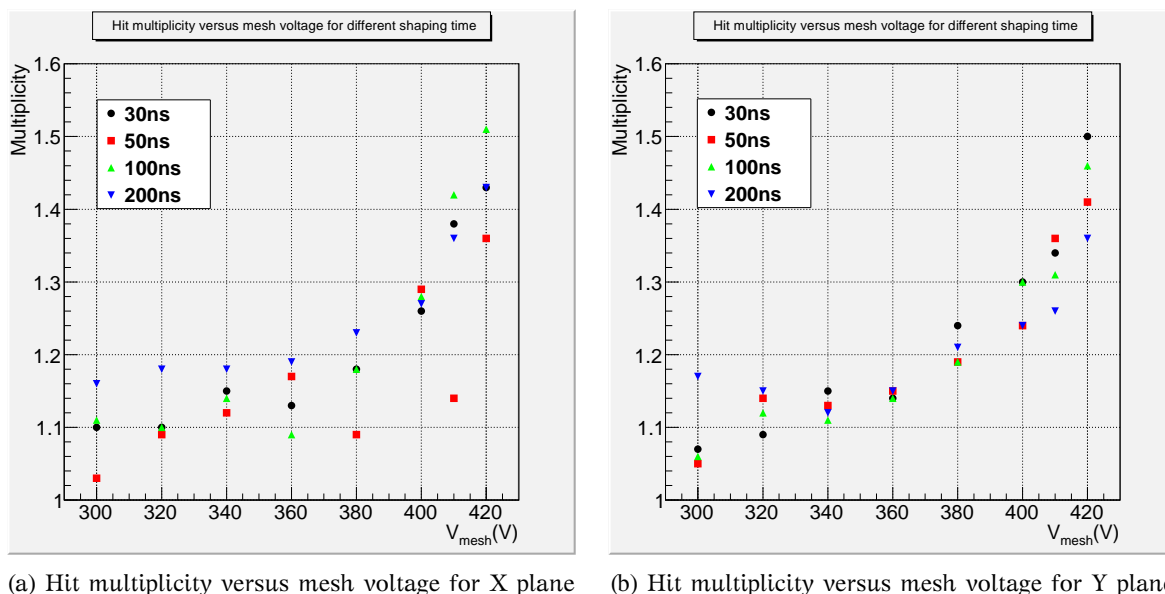
Figure 7.8: Mesh voltage scan for various shaping times.

7.5.2 Threshold scan

The behavior of multiplicity versus threshold was also studied and is illustrated in figures 7.10(a) and 7.10(b). After a quick fall, the multiplicity rises slowly and then decreases at high threshold. At very low threshold, almost all pads receiving charge are seen and the maximum multiplicity is measured. With increasing threshold, secondary hits due to small charge overflows are quickly vanishing, leading the multiplicity to decrease dramatically down to 1.04 at 40 fC. Above this value, low energy single hit events are ignored, therefore, only events with a large energy deposit are normally considered.These events likely contain δ-rays leading to some ionization far from the track and hence to a higher multiplicity.

7.5.3 Angular scan

Pad multiplicity is directly impacted by the angle of incidence of traversing muons. Its dependence to the angle was studied by rotating the prototype with respect to the beam direction. As is seen in figures 7.11(a) and 7.11(b), the hit multiplicity reaches 1.5 at angles as large as 60° .
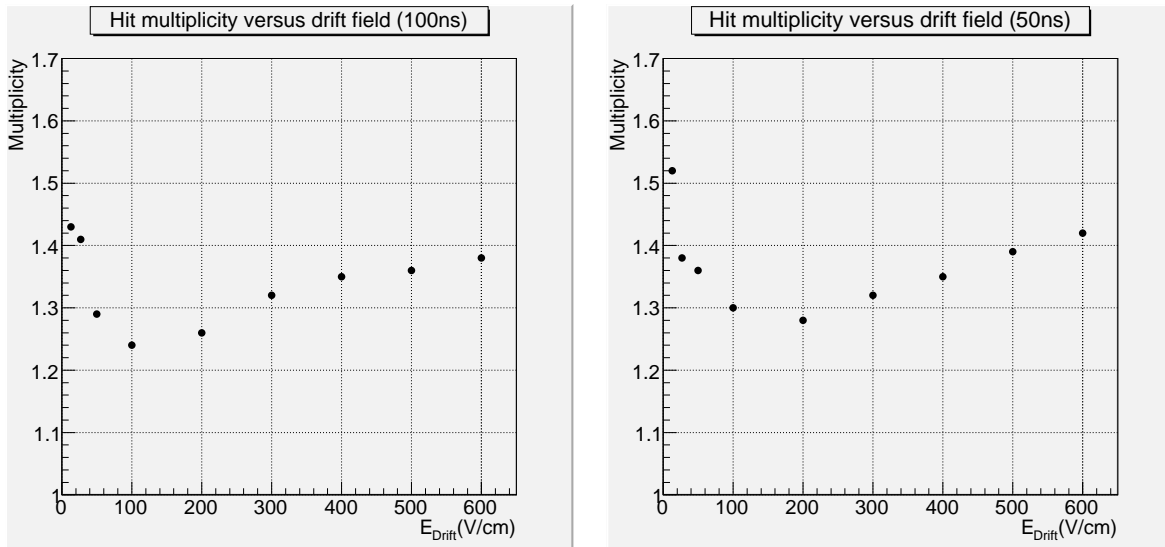
(a) Hit multiplicity versus drift field for X plane

(b) Hit multiplicity versus drift field for X plane

Figure 7.9: Drift field scan.
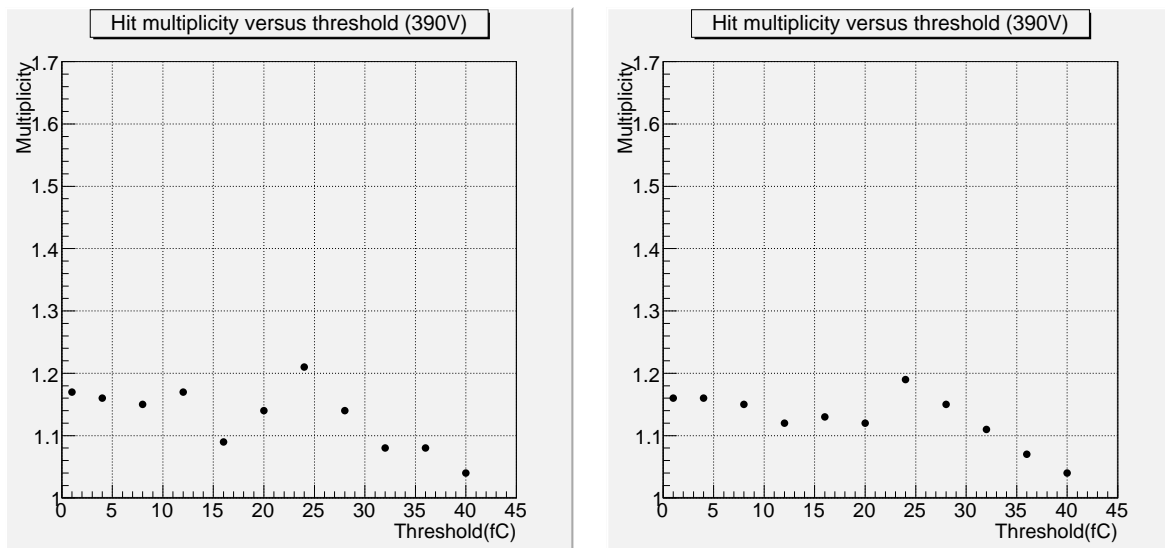
(a) Hit multiplicity versus drift field for X plane

(b) Hit multiplicity versus drift field for X plane

Figure 7.10: Threshold scan.

(a) Hit multiplicity versus angle for X plane

(b) Hit multiplicity versus angle for Y plane
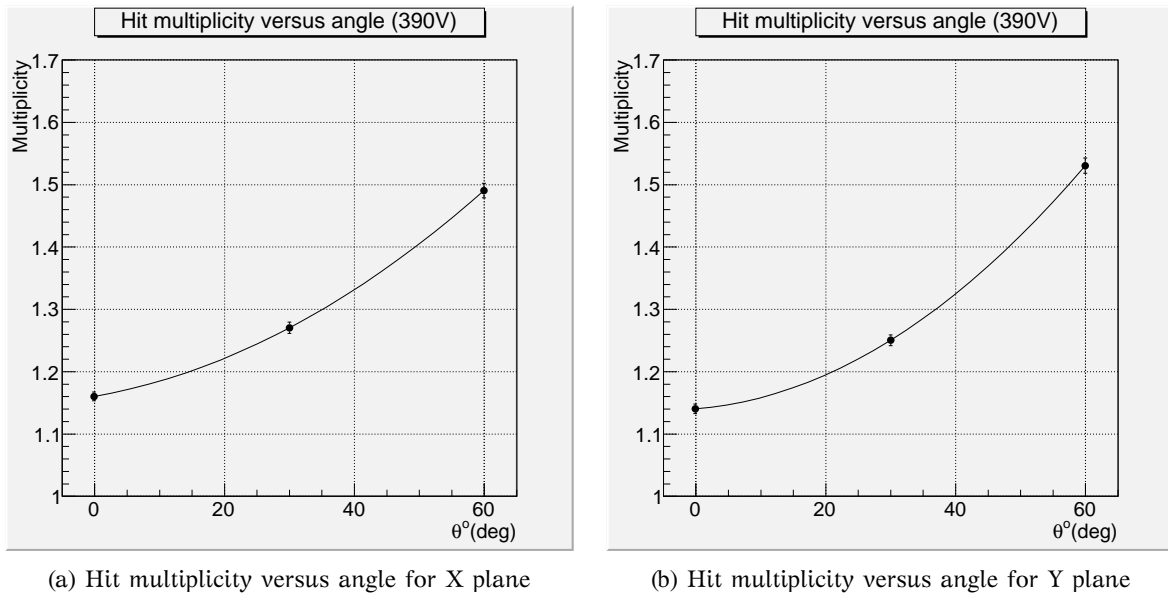
Figure 7.11: Angular scan.

7.6 The effect of the dead areas

One of the tasks of this thesis was to determine the efficiency drop due to the spacers placed between two ASUs which add a dead area of 5 *mm*. In order to do this we have to create efficiency maps for X and Y plane.The efficiency map is a 1D histogram and it follows from the next method:

- Divide divide the X,Y space of the strips into a certain number of wide bins, suitable to the precision of the track extrapolation.

- When finding a track traversing a given bin, fill a 1D histogram.

- Check if the prototype was efficient or not in a ±3 pad area (time AND position cut) and fill a second histogram.

- The ratio of the previous histograms provides a new 1D histogram for each plane which is the efficiency map.

7.6.1 Track extrapolation resolution

The extrapolation resolution of the telescope tracks to the square meter prototype, faces a problem. As it was mentioned, the spatial resolution of the telescope chambers is excellent due to the strips and as a result the resolution is a few *μm*. So can extrapolate the impact of the track with a high resolution. But, the prototype has as anode, 1 *cm*^{2} pads. The particle position can only be considered being at the center of the pad. Hence, this leads to worse precision if we use the method described at section 5.8 for the intrinsic resolution of telescope chambers.

We can avoid this method if we use again the basic geometry of our detector stack (7.12) including this time the square meter prototype. Applying the method of similar triangles two times, first using stations 1,3 and 5 and then stations 3,5 the *m*^{2} prototype, we can calculate the resolution at the *m*^{2} prototype reference plane. For X and Y plane the calculation gives:

First

$$\frac{x_3 - x_1}{x_5 - x_3} = \frac{z_3 - z_1}{z_5 - z_3} = 1$$

$$\Rightarrow x_3 - x_1 = x_5 - x_3 \tag{7.1}$$

Then

$$\frac{x_5 - x_3}{x_{m^2} - x_5} = \frac{z_5 - z_3}{z_{m^2} - z_5} = c$$

$$\overset{7.1}{\Rightarrow} x_3 - x_1 = c \cdot (x_{m^2} - x_5)$$

$$\Rightarrow f_{m^2} = x_2 - x_1 - c \cdot (x_{m^2} - x_5)$$
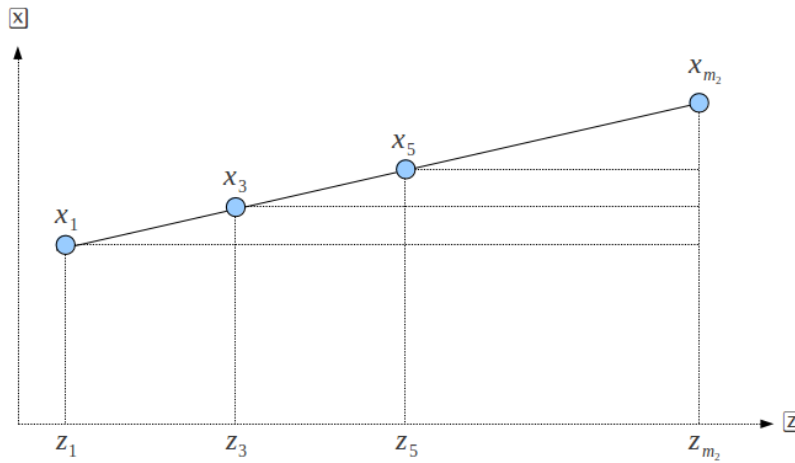
Figure 7.12: Schematic of the basic geometry used in the calculation of extrapolation resolution.

From the previous equation by error propagation, we have:

$$\sigma_x = \frac{\sigma_{f_{m^2}}}{\sqrt{(c)^2 + 1^2 + 1^2}} \tag{7.2}$$

So, from the f_{m^2} distribution we can calculate the spatial resolution on the m^2 reference plane. The distributions of f_{m^2} for the X and Y plane can be found at figure 7.13. The total resolution at the m^2 prototype reference plane depends on the extrapolated resolution of the tracker and on the extrapolation precision of the track according to the next equation:

$$R^2 = \sigma^2_{tracker} + \sigma^2_{extrapolation}$$

$$\boxed{\Rightarrow \sigma_{extrapolation} = \sqrt{R^2 - \sigma^2_{tracker}}}$$

where R^2 given from equation 7.2.

In order to calculate the extrapolated precision of the tracker we use the formula which follows from the correlation matrix of the track parameters:

$$\sigma_{tracker} = \frac{\sigma_2^2\sigma_3^2(z_0 - z_1)^2 + \sigma_1^2(\sigma_3^2(z_0 - z_2)^2 + \sigma_2^2(z_0 - z_3)^2)}{\sigma_3^2(z_1 - z_2)^2 + \sigma_2^2(z_1 - z_3)^2 + \sigma_1^2(z_2 - z_3)^2}$$

After simple math we have, for X and Y plane respectively:

$$\sigma_{extrapolation,x} = 1.2mm$$

$$\sigma_{extrapolation,y} = 1.1mm$$

Now, with an extrapolation resolution of 1.2mm we are able to choose the correct number of bins for the efficiency map histograms.
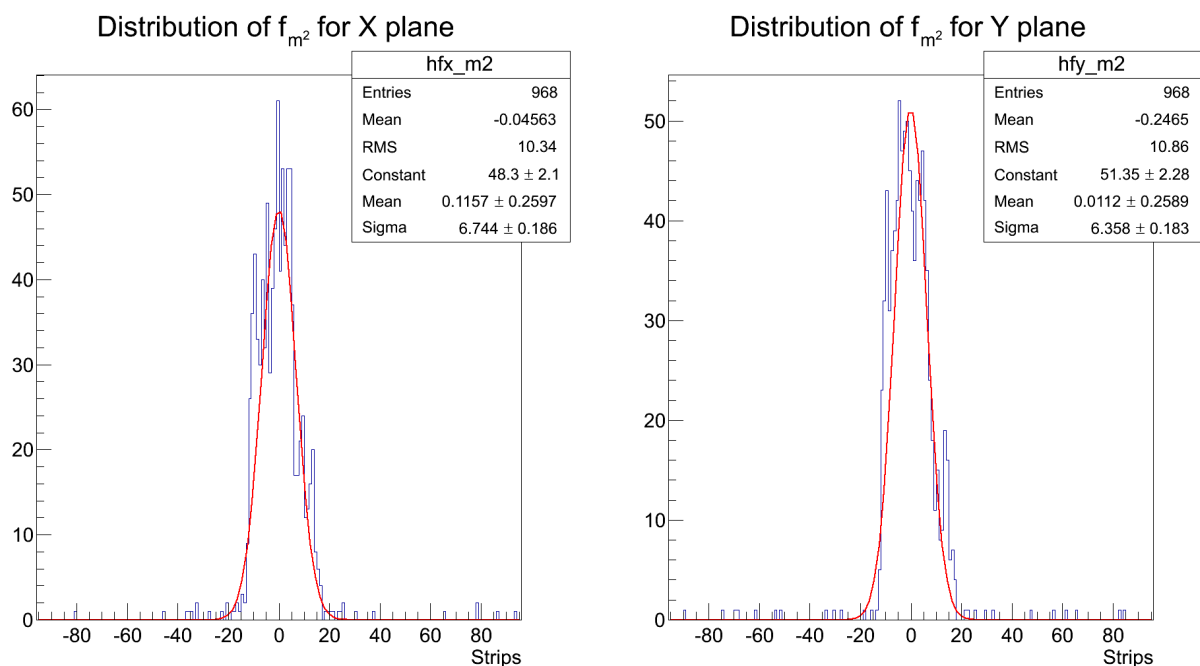
Figure 7.13: Distrifution of function f_{m^2} used for the calculation of extrapolation resolution.

7.6.2 Efficiency maps

The extrapolation resolution of 1.2 mm in addition with the 2.4 × 2.4 cm^2 of the telescope active area, indicates that we have to divide our X,Y strip space in 20 wide bins in order to create the efficiency maps. If we use a run where the beam was targeted to the ASU junction, then we expect to see a drop at 32 cm for the X plane or at 48 cm for the Y plane. This study resulted in figures 7.14 and 7.15. The upper x-axis shows the extrapolated position to the prototype.

In figure 7.14 the efficiency map for a run where the beam was targeted to the ASU junction is shown. As we can see at the efficiency map for the Y plane there is a drop to the efficiency between 47 cm - 48 cm. Knowing that the spacer adds a "dead zone" of 5mm between the ASUs, we are able to see an efficiency drop about 80% for the Y plane with a width of 5mm
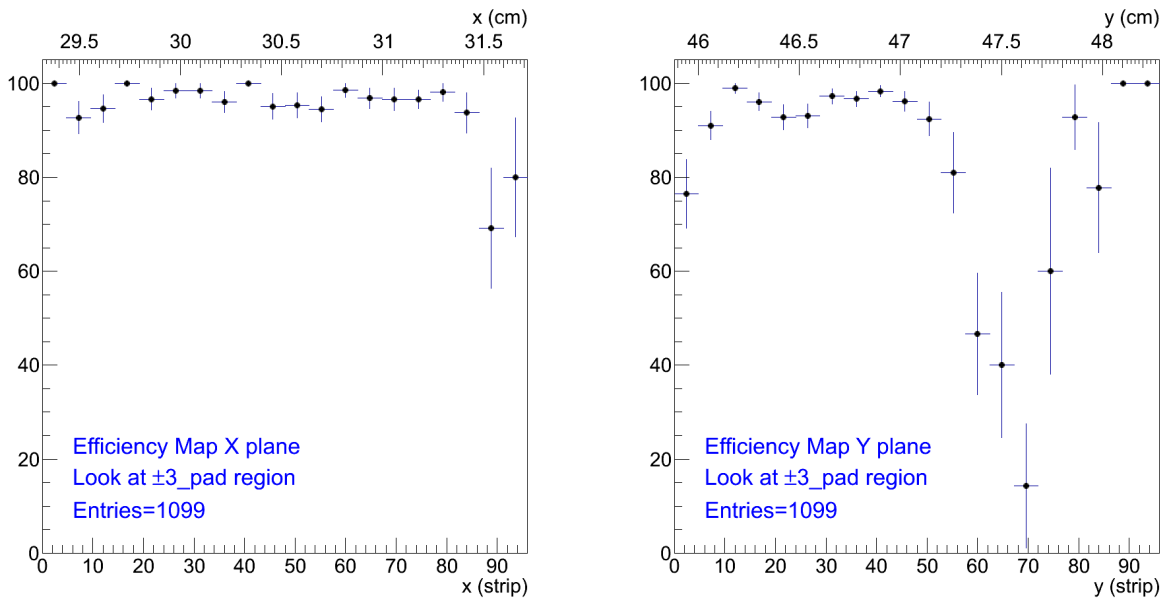
Figure 7.14: Efficiency map of a run where the beam was targeted to the ASU junction.
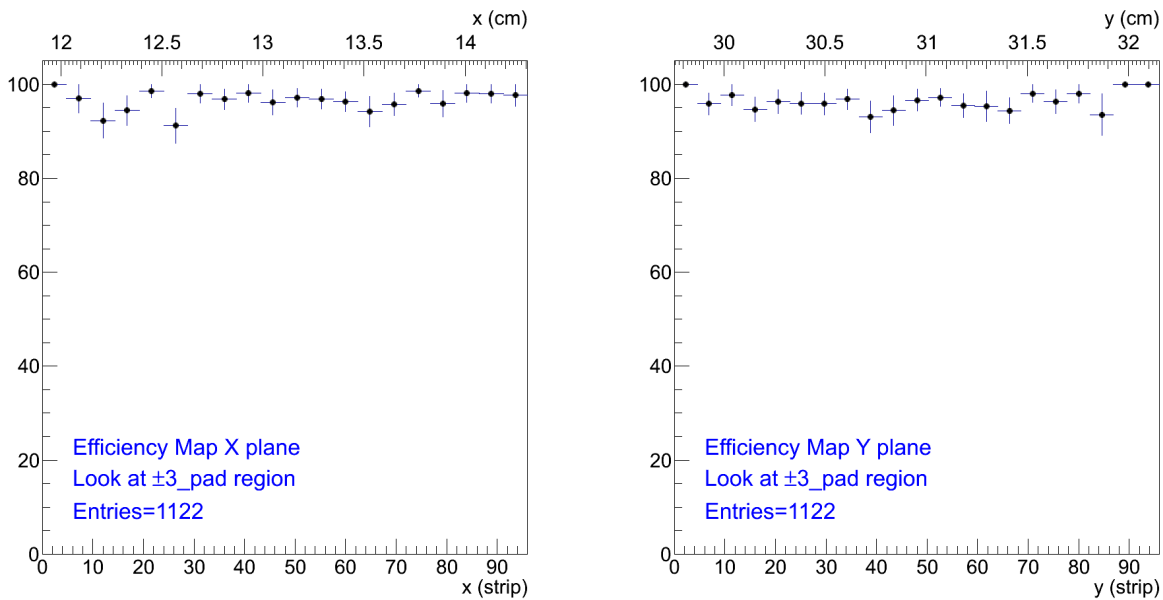
Figure 7.15: Efficiency map of a run where the beam was not targeted to the ASU junction.

approximately, as expected. For the X-plane, we can see the start of the drop at 32 *cm* but not the whole drop, because the active area off the telescope does not cover the ASU junction. On the other hand, in figure 7.15 the efficiency maps for a run where the beam was targeted to the middle of an ASU can be found. As expected there is no drop to the efficiency maps which are uniform.

7.7 Performance to pions

During the testbeam the 150 *GeV/c* pion beam was used to produce hadron showers which would propagate to the prototype. A 20 *cm* thick block of iron placed half a meter in front of the prototype. This set-up allows to get a first idea of the response of the prototype in high multiplicity showers. In addition, the possibility to distinguish by use of the three thresholds multi-particles and single particle within 1 cm^2 cells can be examined.

(a) Pion beam profile without the iron block

(b) Pion beam profile with the iron block
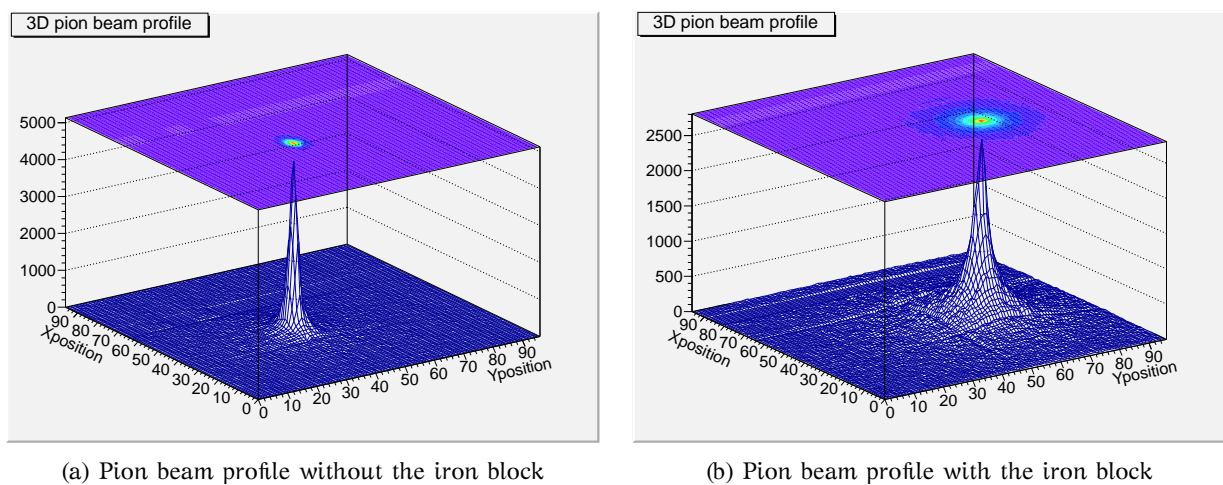
Figure 7.16: Three dimensional profile of the pion beam.

Thanks to the possibly large spatial extend of some showers, a uniformity measurement can be carried out quickly. The pattern exhibits rings that correspond to non-showering pions in the center surrounded by electromagnetic and hadronic shower components. Thanks to a uniform response, a clear azimuthal symmetry is observed. The effect of dead zones at the ASU junctions is better seen when projecting the pattern along vertical and horizontal axis. Pads at the ASU edges show a lower efficiency, as expected from the 2 *mm* wide Bulk cover lay line running along them.

Runs with pion beams were performed at various mesh voltages. The primary goal was to measure the hit multiplicity. Distributions obtained at 325, 350 and 375 *V* exhibit a sharp peak and a long tail from traversing and showering pions respectively (Figure 7 left). The tail extends to larger values at higher voltages while the population of the zero hit bin drops. At 375 *V* (MIP efficiency of 97 %), the maximum number of hits is quite large: up to ∼ 300.

(a) Pion beam profile for the Xplane

(b) Pion beam profile for the Y plane
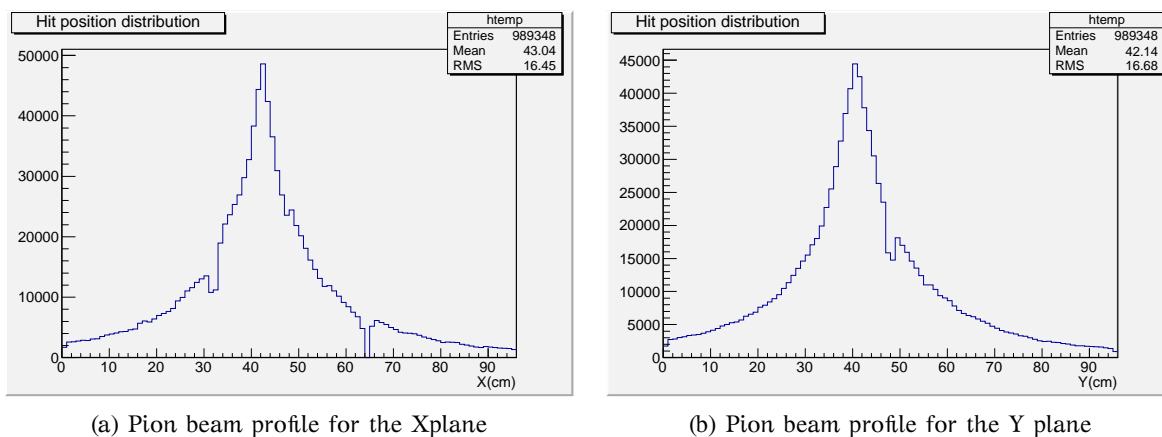
Figure 7.17: One dimensional profile of the pion beam. Both for X in (a) and for Y plane in (b) someone can see the effect of the dead areas.
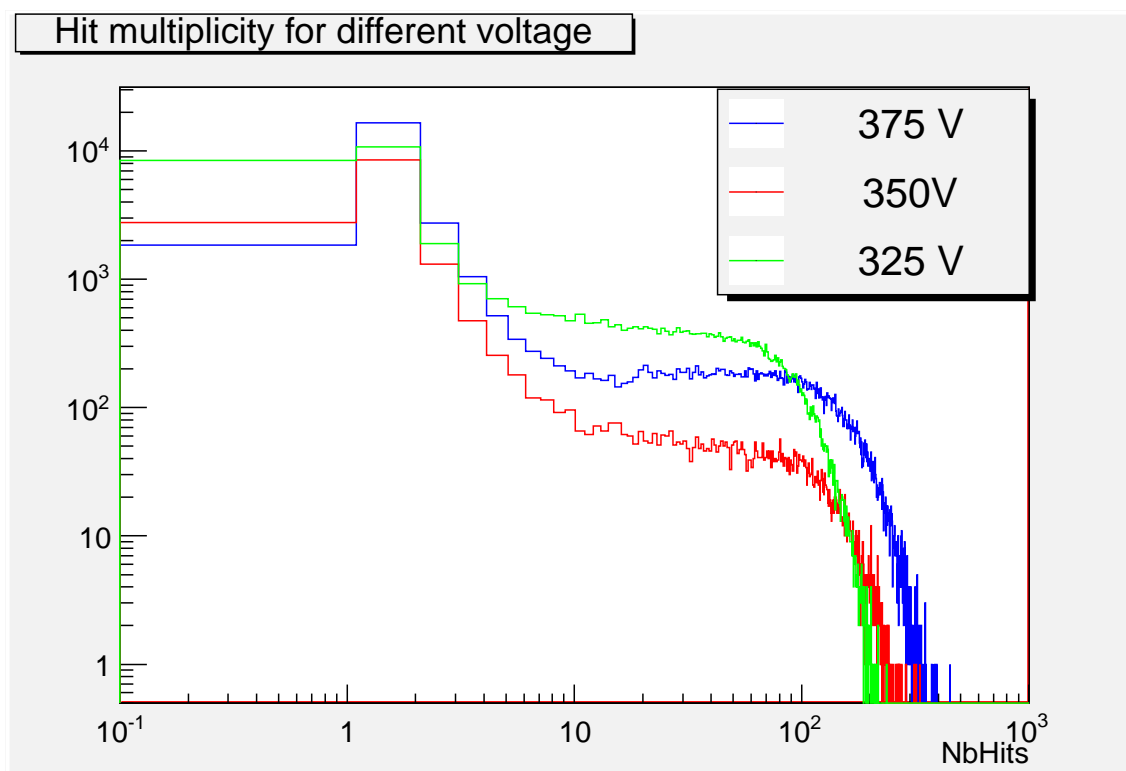
Figure 7.18: Hit multiplicity of the showers created with the iron block, for various mesh voltages.

(a) 325V

(b) 350V

(c) 375V
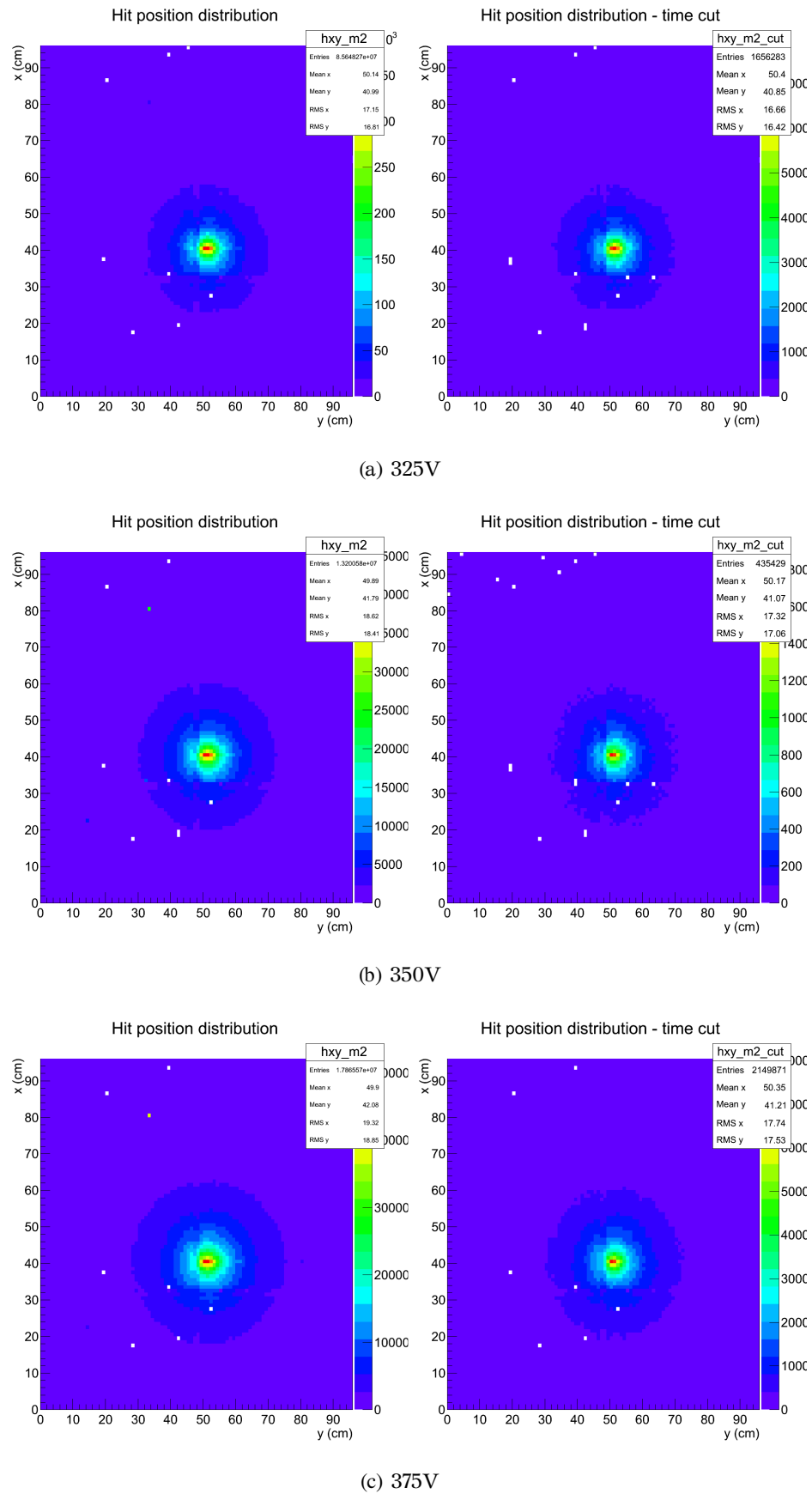
Figure 7.19: Two dimensional profile of the pion beam. As we can see for higher voltages the spread of the shower increases as expected.

Coclusion

The goal of this thesis was to study the performance of the square meter prototype to muon (mainly) and pion beams. As it was the first time that the prototype exposed to particle beams, it was of great importance to determine the working point of the detector and measure the efficiency and multiplicity.

The first important step, was the development of the clustering algorithm for the telescope chambers. The fact that the telescope chambers do not have resistive coating for spark protection, makes important the separation of normal and noisy hits. An efficient clustering algorithm has been developed, able to specify the number of clusters per event and their properties like their size the total charge.

The RD51 tracking algorithm used in order to reconstruct the particle tracks, where we use as input, the output of the tracking algorithm. However, the track data were not produced into the Micromegas Framework. As a result, the software in order to implement the track data into the framework was necessary. The new software is able to update each event of the telescope, with its associated tracks.

In order to support the analysis of the square prototype data, the CaloEvent class added to the framework. The role of the class is to keep the important information of each event and to suppress the noisy hits. The modification of some components of the class and the development of some new scripts, gave the ability to contain all the important information both for the telescope and the prototype in one single data file.

The efficiency and multiplicity measurements performed using the muon beam, for various detector settings. The prototype records an efficiency of 98-99% for various voltage and drift field settings. The hit multiplicity lies below 1.2 up to a mesh voltage 380 - 390 V (i.e. gain of 3000). At higher gas gain, neighboring pads become sensitive to single electrons, increasing the multiplicity. There is however no reason to work in that regime as high efficiency is reached at lower gains.

Varying the threshold from 1 fC which is the lowest running threshold to 40 fC, results to a steep drop of efficiency. At very low threshold, almost all pads receiving charge are seen and the maximum multiplicity is measured. With increasing threshold, secondary hits due to small charge overflows are quickly vanishing, leading the multiplicity to decrease dramatically down to 1.04 at 40 fC. Above this value, low energy single hit events are ignored, therefore, only events with a large energy deposit are normally considered.

One task of great importance was to determine the effect of dead areas of the detector. In order to understand this effect we have to create the efficiency maps for the square meter prototype. This analysis resulted to a drop in the efficiency larger than 80% due to the dead areas.

Finally, a quick study of the performance to pion beams carried out. An iron block was used to produce hadron showers. The square meter prototype possess good response and uniformity to high multiplicity showers.

Bibliography

[1] C. Adloff et al, *Recent results of Micromegas sDHCAL with a new readout chip*, arXiv.org, arXiv:1202.0624, February 2012.

[2] R. Gaglione et al, *A micromegas chamber with embedded dirac asic for hadronic calorimeter*, In 1st International Conference On Micro Pattern Gaseous Detectors, JINST,4,11011.

[3] C. Adloff et al, *Large area Micromegas chambers with embedded front-end electronics for hadron calorimetry*, Physics Procedia, 37 (2012) 221 – 228.

[4] C. Adloff et al, *Micromegas chambers for hadronic calorimetry at a future linear collider*, JINST, November 2009.

[5] C. Adloff, et al, *Effects of high-energy particle showers on the embedded front-end electronics of an electromagnetic calorimeter for a future lepton collider*, NIM A 654 (2011).

[6] G. Charpak et al, *Micromegas, a multipurpose gaseous detector*. Nuclear Instruments and Methods in Physics Research Section A: Accelerators, Spectrometers, Detectors and Associated Equipment, 2002.

[7] I. Giomataris et al, *Micromegas in a bulk*, Nuclear Instruments and Methods in Physics Research Section A: Accelerators, Spectrometers, Detectors and Associated Equipment, 2006.

[8] M. A. Thomson, *Particle Flow Calorimetry and the PandoraPFA Algorithm*, Nuclear Instruments and Methods in Physics Research A, 611, july 2009.

[9] T. Alexopoulos et al, *Development of large size micromegas detector for the upgrade of the atlas muon system*, Nuclear Instruments and Methods in Physics Research Section A: Accelerators, Spectrom- eters, Detectors and Associated Equipment, 617(1-3):161 – 165, 2010. 11th Pisa Meeting on Advanced Detectors - Proceedings of the 11th Pisa Meeting on Advanced Detectors.

[10] F. Sauli, *Principle of operation of multiwire proportional and drift chambers*,"yellow report". CERN, 1977.

[11] K. Nakamura and Particle Data Group, *Review of Particle Physics*, Journal of Physics G: Nuclear and Particle Physics, 2010.

[12] W. Blum, W. Riegler and L. Rolandi, *Particle detection with drift chambers*, Springer-Verlag, Berlin, 2008.

[13] R. C. Fernow. Introduction to experimental particle physics. Cambridge Univ. Press, Cambridge, 1986.

[14] B. R. Martin and G. Shaw , *Particle Physics*, Third edition, John Wiley & Sons, 2008.

[15] G.F. Knoll, *Radiation Detection and Measurement*, John Wiley & Sons, 2010.

[16] J. E Turner , *Atoms, Radiation and Radiation Protection*, Third edition, WILEY-VCH Verlag GmbH & Co. KGaA, Weinheim , 2007.

[17] C. Grupen and B. A. Shwartz, *Particle Detectors*, Second Edition, Cambridge University Pressm 2008.

[18] W. R. Leo, *Techniques for nuclear and particle physics experiments: a how-to approach*, Springer-Verlag, Berlin, 1994.

[19] M. Chefdeville, *Development of a Micromegas-like gaseous detector using a pixel readout chip as collecting anode*, PhD thesis, University of Amsterdam/Universit´ Paris Sud XI, 2009.

[20] K. Karakostas, *A micromegas tracker for the RD51 test beam*, M.Sc. Thesis, National Technical University of Athens, 2010.

[21] K. Ntekas, *Μελέτη ανιχνευτή micromegas σε δοκιμαστική δέσμη πιονίων ορμής 120 GeV/c στο H6/SPS/CERN*, M.Sc. Thesis, National Technical University of Athens, 2012.

[22] ILC home page,
http://www.linearcollider.org/ILC

[23] CLIC home page,
http://clic-study.org/

[24] CALICE Official web page,
https://twiki.cern.ch/twiki/bin/view/CALICE

[25] RD51 home page,
http://rd51-public.web.cern.ch/rd51-public/

[26] SiD. Letter of Intent, March 2009,
http://arxiv.org/pdf/0911.0006v1.pdf

List of Figures

List of Tables